Adsorption and degradation of chemical warfare agents on oxides

Kristi Mo and Stig Rune Sellevåg

Norwegian Defence Research Establishment (FFI)

10 November 2011

FFI-rapport 2010/01775

111601

P: ISBN 978-82-464-2014-1
E: ISBN 978-82-464-2015-8

Keywords

Kjemiske stridsmidler

Adsorpsjon

Nedbryting

Faste stoffer

Approved by

Hans Christian Gran	Project Manager
Jan Ivar Botnan	Director

English summary

The adsorption and degradation of chemical warfare agents and their simulants on oxides have been reviewed. As part of the work, the physics of adsorption and desorption phenomena have also been reviewed, together with some important experimental and computational methods. The major degradation pathways for sulfur mustard are elimination of HCl at basic oxide sites and intermolecular addition-elimination reactions at acid sites. Less information is available for other blister agents. Nerve agents adsorb molecularly to oxides through bonding between the P=O group and surface acid sites. The mechanism for the degradation of the adsorbed nerve agents is generally the same for the different oxides with Fe_2O_3 and SiO_2 as exceptions. On SiO_2 little if any degradation of the nerve agent occurs.

Sammendrag

Denne rapporten er en litteraturstudie av adsorpsjonen og nedbrytningen av kjemiske stridsmidler og deres simulanter på oksider. Som en del av studien, har fysikken bak adsorpsjons- og desorpsjonsprosesser blitt gjennomgått sammen med noen viktige eksperimentelle og teoretiske metoder. Nedbrytning av sennepsgass på oksider skjer hovedsakelig ved eliminasjon av HCl på basiske seter på oksidet, og ved intermolekylære addisjons-eliminasjonsreaksjoner på sure seter. Nervestridsmidler adsorberer molekylært til oksider ved binding mellom P=O-gruppen og sure seter på overflaten til oksidet. Mekanismen for nedbrytningen av nervestridsmiddelet er generelt lik for ulike oksider, med unntak for Fe_2O_3 og SiO_2. På SiO_2 skjer det liten eller ingen nedbrytning av nervestridsmiddelet.

Contents

1 Introduction

Chemical weapons are considered as weapons of mass destruction (WMD). Under the Chemical Weapons Convention, chemical weapons are defined as munitions and devices specifically designed to cause death or other harm through the release of toxic chemicals or precursors for toxic chemicals as a result of the employment of such weapons [1]. A toxic chemical is defined as any chemical which through its chemical action on life processes can cause death, temporary incapacitation or permanent harm to humans or animals. A precursor for a toxic chemical is defined as any chemical reactant which takes part at any stage in the production of a toxic chemical. This includes any key component of a binary or multicomponent chemical system [1]. Such toxic chemicals are often called chemical warfare agents (CWA).

Chemical warfare agents are often categorized in accordance with their physiological mode of operation: nerve, blister, choking, blood, and incapacitating agents. The effect of the chemical agents may be immediate as is the case for the nerve agents, or delayed as is the case for the blister agent sulfur mustard. In addition, the agents may be persistent, sulfur mustard and the nerve agent VX being typical examples, or non-persistent as is the case for the nerve agent sarin [2].

The first use of chemical warfare agents as weapons of mass destruction dates back to World War I. On April 22, 1915, large amounts of chlorine (Cl_2) were released by German Forces in the attack at Ypres, Belgium [3]. After World War I, chemical warfare agents have been used at several occations like the Halabdja Massacre in 1988 where Iraqi Forces attacked the Kurds, or the Aum Shinrikyo terrorist attacks in Matsumoto (1994) and Tokyo (1995) [3].

Chemical warfare agents are now being regulated under the Chemical Weapons Convention (CWC) which came into force on April 29, 1997. As of May 21, 2009, 188 states have signed and ratified the Convention. This does not imply, however, that the threat posed by chemical warfare agents has vanished. Large amounts of chemical weapons are still being stockpiled in several countries. The Russian Federation, for example, has declared a stockpile of 40,000 tons of chemical weapons of category 1 under the CWC to the Organisation for the Prohibition of Chemical Weapons (OPCW). Angola, the Democratic People's Republic of Korea (North Korea), Egypt, Somalia, and the Syrian Arab Republic (Syria) have neither signed nor accepted to the Chemical Weapons Convention [4]. North Korea, Egypt, and Syria allegedly posess chemical weapons capabilities [5-7].

The actions by the Japanese cult Aum Shinrikyo have demonstrated that non-state actors may obtain chemical warfare agents. In 2002 the Norwegian Defence Research Establishment (FFI) reported a survey of terrorist and rebel groups' interests in and efforts at acquiring chemical, biological, radiological, and nuclear (CBRN) substances [8]. It was found that serious cases of CBRN acquisition and/or use by terrorist and rebel groups have occurred in as many as eleven countries; chemical warfare agents accounted for more than half of the incidents. Religious groups followed by ethnic-separatist groups were greatly over-represented among the perpetrating

groups. The FFI report recommended increased policy attention to improve national response capacity and preparedness to counter and handle low-scale CBRN terrorist incidents.

This requires, among other things, technologies for protection and decontamination of personell and equipment. This is a challenging task because many materials are porous; typical examples being polymers, paints and building materials. Thus the uptake of chemical warfare agents by such materials may be significant and the materials may be difficult to decontaminate. Further, many of the existing decontamination technologies are aggressive towards materials and harmful to the environment and human beings [9]. There is therefore a need for materials that are easier to decontaminate and new decontamination technologies that neutralize the chemical warfare agents while still being environmentally acceptable.

To achieve this goal, fundamental understanding of the interaction between chemical warfare agents, materials, and decontaminants is needed. This includes understanding of the sorption processes occurring. According to the IUPAC[1] Gold Book [10], *sorption* is the process by which a substance (sorbate) is sorbed (adsorbed or absorbed) on or in another substance (sorbent) [10]. *Adsorption* is an increase in the concentration of a dissolved substance at the interface of a condensed phase (e.g. a solid) and a liquid or gaseous phase due to the operation of surface forces [10]. *Absorption* is the process of one material (absorbate) being retained by another (absorbent); this may be the physical solution of a gas, liquid, or solid in a liquid, or attachment of molecules of a gas, vapor, liquid, or dissolved substances to a solid by physical forces [10]. *Desorption* is the converse of adsorption. As part of the sorption process, *diffusion* of species will usually also take place. The different sorption processes are illustrated in Figure 1.1.

FFI has initiated a project that will investigate the sorption processes occurring in the interaction between chemical warfare agents, materials, and decontaminants. This report has two parts. First, the physics of adsorption and desorption phenomena are reviewed, and an overview of some important experimental and computational methods is given. The purpose of this part is to provide unacquainted readers some theoretical background for understanding adsorption phenomena. The second part reviews the current knowledge available in the open literature concerning the adsorption of chemical warfare agents to oxides. Unpainted metal surfaces are often covered with an oxide layer and, as will be shown later, many oxides may adsorb and decompose chemical warfare agents.

This report is organized as follows: Chapter 2 gives an overview of important physicochemical properties of selected chemical warfare agents. The agents selected are different blister and nerve agents. These agents are the most harmful compounds and represent the greatest challenge when it comes to protection and decontamination. Chapter 3 gives a short description of the crystalline structure of solids. Chapter 4 gives a thermodynamic description of surfaces and interfaces. Chapter 5 and 6 review the underlying physics of adsorption and desorption processes, respectively. Chapter 7 gives a short description of some relevant experimental and computational methods for

[1] The International Union of Pure and Applied Chemistry.

Chapter 7 gives a short description of some relevant experimental and computational methods for studying the adsorption of chemical warfare agents to solid surfaces. Finally, chapter 8 reviews the adsorption of chemical warfare agents to oxides and a summary is given.

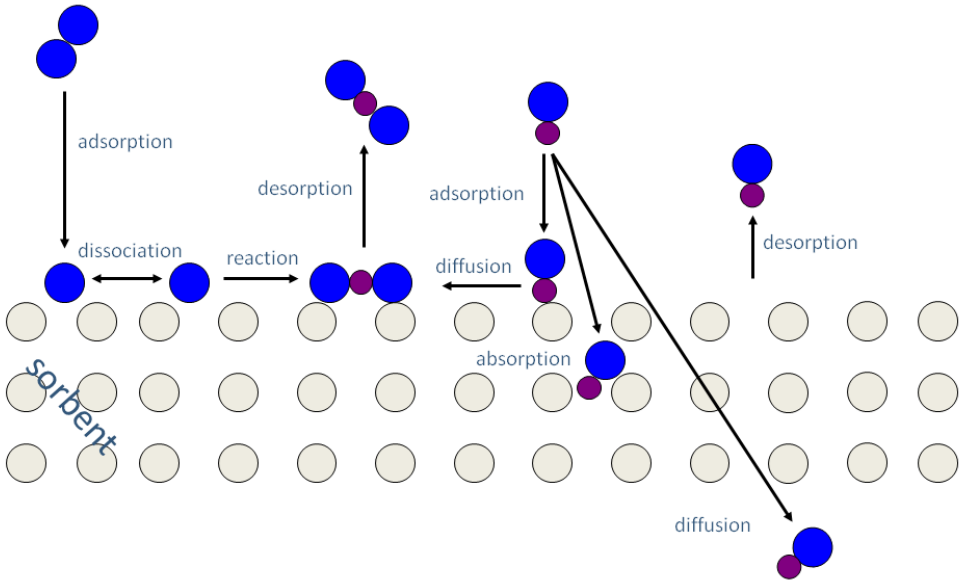

Figure 1.1 Illustration of different sorption processes (reproduced after [11]).

2 Physicochemical properties of chemical warfare agents

2.1 Blister agents (vesicants)

Blister agents are divided into three groups: mustards, arsenicals, and urticants [2]. The most common mustards are sulfur mustard (HD) and the nitrogen mustards HN-1, HN-2, and HN-3. Because of their physical properties, they are very persistent, especially sulfur mustard. The mustards are also so-called delayed-action casualty agents. It can take several hours up to days before the effect of exposure is observed [2]. The molecular structure of sulfur mustard is illustrated in Figure 2.1 and some of its physicochemical properties are listed in Table 2.1. Commonly used simulants for sulfur mustard include 2-chloroethyl methyl sulfide (2-CEES) and methyl salicylate (MS).

Arsenicals are organic dichloroarsines of which lewisite (L) is the principal compound of military interest [2]. The structural formula of lewisite is given in Figure 2.1. Contrary to the mustards, the effect of exposure to lewisite is immediate. Lewisite hydrolyzes rapidly, even with the moisture in the air [12]. Pure lewisite is therefore not a particularly effective chemical warfare agent, but it is often added to sulfur mustard to lower the freezing point of the sulfur mustard. The mustard-lewisite mixture is denoted HL and consist of 37% sulfur mustard and 63% lewisite by weight [2]. Pure HL has a freezing point of –25.4 °C and munitions grade[2] HL has a freezing point of –42 °C. The freezing point of pure HD is +14.5 °C; see Table 2.1.

[2] The quality used in chemical weapons.

Urticants are not true vesicants because they do not produce fluid-filled blisters. The primary urticant of military interest is phosgene oxime ($Cl_2C=NOH$) also denoted CX. For a list of the physicochemical properties of CX we refer to ref. [2].

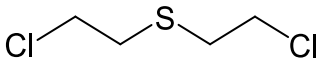

sulfur mustard (HD)

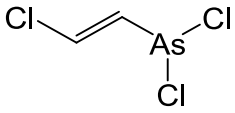

lewisite (L)

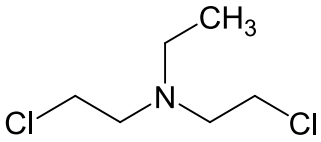

nitrogen mustard (HN-1)

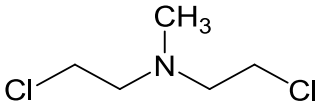

nitrogen mustard (HN-2)

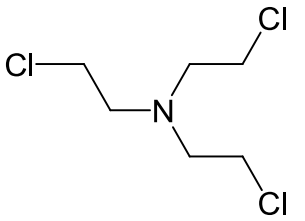

nitrogen mustard (HN-3)

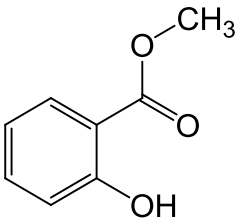

methyl salicylate (MS)

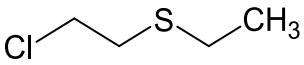

2-chloroethyl ethyl sulfide
(2-CEES/half mustard)

Figure 2.1 Structural formulas of the blister agents sulfur mustard, nitrogen mustard, and lewisite, and two potential sulfur mustard simulants methyl salicylate and 2-chloroethyl ethyl sulfide.

Table 2.1 Physicochemical properties of chemical warfare agents and potential simulants (data from ref. [2]).[a]

compound	abbrev.	CAS no.	molecular formula	mass / g mol^{-1}	m.p. / °C	b.p. / °C	ρ(25 °C) / g cm^{-3}	P_{vap}(25 °C) / kPa	K_H(25 °C)[b]	$\Delta_{vap}H°$ / kJ mol^{-1}	η(25 °C) / mPa s	γ(25 °C) / mN m^{-1}
blister agents												
sulfur mustard	HD	505-60-2	$C_4H_8Cl_2S$	159.07	14.45	218[b]	1.2685	1.41×10^{-2}	9.8×10^{-4}	62.8	3.951	42.5
nitrogen mustard	HN-1	538-07-8	$C_6H_{13}Cl_2N$	170.08	–34.2	192[b]	1.086	3.25×10^{-2}	n.d.	54.4	n.d.	n.d.
nitrogen mustard	HN-2	51-75-2	$C_5H_{11}Cl_2N$	156.05	–70	177[b]	1.118	5.55×10^{-2}	n.d.	54.0	n.d.	n.d.
nitrogen mustard	HN-3	555-77-1	$C_6H_{12}Cl_3N$	204.53	–3.74	257[b]	1.2352	1.47×10^{-3}	n.d.	66.1	0.073	40.9
lewisite	L	541-25-3	$C_2H_2AsCl_3$	207.32	–1.2[c]	196[b]	1.8793	4.61	n.d.	64.9	2.053	41.1
2-chloroethyl ethyl sulfide[c]	2-CEES/ HM	693-07-2	C_4H_9ClS	124.63	–48.6	156.5	1.0663[c]	4.53×10^{-1}	1.5×10^{-2}	37.7[c]	n.d.	n.d.
methyl salicylate[c]	MS	119-36-8	$C_8H_8O_3$	152.15	–8	223	1.1798[c]	5.33×10^{-3}	4×10^{-3}	47.7[c]	n.d.	n.d.
G-agents												
tabun	GA	77-81-6	$C_5H_{11}N_2O_2P$	162.13	–50	248	1.0756	7.60×10^{-3}	6.5×10^{-7}	64.9	2.277	32.5
sarin	GB	107-44-8	$C_4H_{10}FO_2P$	140.09	–56	150	1.0887	3.31×10^{-1}	3.8×10^{-4}	48.5	1.397	25.9
soman	GD	96-64-0	$C_7H_{16}FO_2P$	182.17	–42	198	1.0222	5.35×10^{-2}	1.9×10^{-4}	55.2	3.167	24.5
cyclosarin	GF	329-99-7	$C_7H_{14}FO_2P$	180.16	–12	228	1.1276	1.24×10^{-2}	n.d.	59.8	5.41	32.3
diisopropyl methyl-phosphonate	DIMP	1445-75-6	$C_7H_{17}O_3P$	180.19	< 25	121	0.976[c]	3.69×10^{-2}	1.8×10^{-3}	43.2[c]	n.d.	n.d.
dimethyl methyl-phosphonate	DMMP	756-79-6	$C_3H_9O_3P$	124.08	–48	181	1.16[c]	1.28×10^{-1}	5.3×10^{-5}	40.0[c]	n.d.	n.d.
V-agents												
O-ethyl methyl phosphonothiolate	VX	50782-69-9	$C_{11}H_{26}NO_2PS$	267.37	< –51	292	1.0083	1.17×10^{-4}	1.4×10^{-7}	80.3	10.041	31.3
O,*S*-diethyl phenyl-phosphonothioate	DEPPT	57557-80-9	$C_{10}H_{15}O_2PS$	230.26	n.d.	98-100	1.1395[d]	1.20×10^{-4}	n.d.	53.3[d]	n.d.	n.d.

[a] Abbreviations: m.p. – melting point; b.p. – boiling point; ρ – density; P_{vap} – vapor pressure; K_H – Henry's law constant; $\Delta_{vap}H°$ – enthalpy of vaporization; η – viscosity (1 mPa s = 1 cP); γ – surface tension (1 mN m^{-1} = 1 dynes cm^{-1}); n.d. – no data.

[b] Extrapolated boiling point; sulfur mustard (HD) will decompose.

[c] Data from Bartelt-Hunt et al. [13].

[d] Data from SciFinder Scolar [14].

In kinetic studies, 2-chloroethyl ethyl sulfide, 2-CEES is often used as a simulant for sulphur mustard. In this simulant one of the chlorine atoms in HD is exchanged with a CH_3 group. Several studies on degradation of 2-CEES over metal oxides have been done in the literature. The detected species from studies on degradation of 2-CEES at different oxides are consistent with those found for degradation of HD on the same type of oxides. However the fraction between the dissociated products might differ.

2.2 Nerve agents

Nerve agents are organophosphate esters of the form illustrated in Figure 2.2, and are usually classified as G agents, V agents, and novichok agents. The G and V agents differ in the substituents *X*, *R*, and *R′*, where *X* is the leaving group in the reaction with acetylcholinesterase; see Table 2.2. The G agents were first synthesized by German scientists in the 1930s and 1940s and include tabun (GA), sarin (GB), soman (GD), and cyclosarin (GF) [3]. In the early and mid 1950s, at least three laboratories investigated a class of highly toxic organophosphate esters of various 2-aminoethanethiols resulting in the development of the V agents by British and US Laboratories [3]. Of the V agents, VX was chosen as the most "promising" warfare agent. Chemical variants of VX were produced in the Soviet Union/Russia (Russian VX; abbreviated VR) and China (Chinese VX; abbreviated CVX).

Physicochemical properties of the G agents and VX are summarized in Table 2.1. VX is a viscous compound with a very low vapor pressure. The G-agent sarin, on the other hand, is much more volatile and has lower viscosity. The other G agents are in the range between sarin and VX. The physicochemical properties of VR and CVX (not listed in Table 2.1) are comparable to the properties of VX. Commonly used G-agent simulants include diisopropyl methylphosphonate (DIMP) and dimethyl methylphosphonate (DMMP), where the latter is a simulant for sarin. *O,S*-diethyl phenylphosphonothioate (DEPPT) is a potential simulant for VX. Structural formulas of DIMP, DMMP, and DEPPT are given in Figure 2.3.

The novichok agents are a series of organophosphates developed by the former Soviet Union in the mid-1970s up to its dissolution in 1991 (novichok is Russian for "newcomer"). To our knowledge, the only information published is the information revealed by Dr. Vil S. Mirzayanov, a former Russian scientist at the State Scientific Research Institute of Organic Chemistry and Technology in Moscow [15].

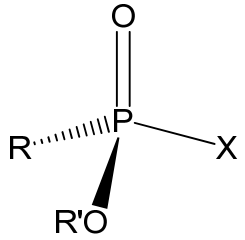

Figure 2.2 General structural formula of nerve agents.

Table 2.2 *Molecular formulas of different nerve agents. Nerve agents are organophosphate esters with the general structure O=P(OR′)RX as illustrated in Figure 2.2.*

nerve agent	*X*	*R*	*R′*
		G agents	
tabun (GA)	–CN	$-N(CH_3)_2$	$-C_2H_5$
sarin (GB)	–F	$-CH_3$	$-CH(CH_3)_2$
soman (GD)	–F	$-CH_3$	$-CH(CH_3)C(CH_3)_3$
cyclosarin (GF)	–F	$-CH_3$	$-C_6H_{11}$
		V agents	
VX	$-SCH_2CH_2N(CH(CH_3)_2)_2$	$-CH_3$	$-C_2H_5$
Russian VX (VR)	$-SCH_2CH_2N(C_2H_5)_2$	$-CH_3$	$-CH_2CH(CH_3)_2$
Chinese VX (CVX)	$-SCH_2CH_2N(C_2H_5)_2$	$-CH_3$	$-C_4H_9$

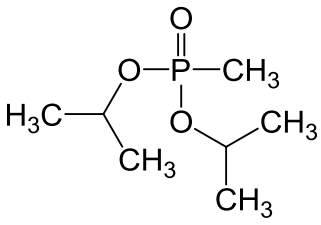

diisopropyl methylphosphonate (DIMP)

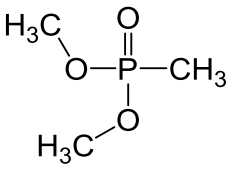

dimethyl methylphosphonate (DMMP)

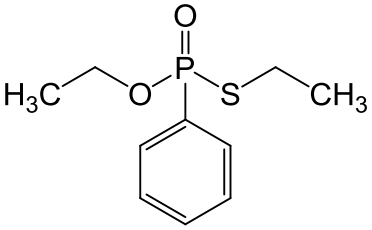

O,S-diethyl phenylphosphonothioate (DEPPT)

Figure 2.3 *Structural formulas of the G-agent simulants diisopropyl methylphosphonate and dimethyl methylphosphonate, and the V-agent simulant O,S-diethyl phenylphospho-nothioate.*

3 Solids

3.1 Structure and unit cells

The solid phase structure is rigid; it is hardly compressible and has high density. The components in a solid must hence be close together and exert large attractive forces on each other. Solids can be divided into two groups, crystalline and amorphous. Polymers and glass are typical amorphous materials.

Crystallines are built up of atoms or molecules in regular arrangement whereas the structure in amorphous solids is partly or totally disordered. The positions of the components in a crystalline solid are normally represented by a lattice, with a three-dimensional repetitious pattern of the components. The unit cell is generated from the atomic positions which are defined from the vectors x_1, x_2, and x_3 from a chosen origo [16]. Figure 3.1 shows a unit cell where the positions of atom a and b is defined relative atom c in origo. The unit cell is then formed by the three-dimensional parallell displacement of the atomic positions (a, b, and c) to neighbour atoms [10]. Each corner in Figure 3.1 hence indicates an atom.

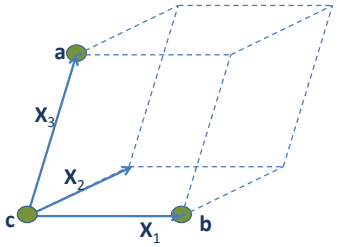

Figure 3.1 Unit cell generated from three basic vectors [16].

Types of crystalline solids are ionic solids (e.g. NaCl), molecular solids (e.g. sucrose), atomic solids (e.g. graphite), and metallic solids (e.g. Al) [17]. Further, metals are because of their different conduction abilities, divided into metals, half-metals and isolators, see e.g. ref. [16].

3.2 Bulk phase

How the atoms in a metal are packed will influence the sorption properties of the metal. Below a short introduction to the most common packing of metals are given. A metal can be illustrated as spherical atoms packed together and bonded to each other equally in all directions. The spheres are packed in layers that most efficiently use the available space so that each sphere in the third layer lies directly over a sphere in the first layer, *aba structure*, or they can occupy positions with no atoms in the two layers below, the *abc-structure,* as shown in Figure 3.2. The closest packed cubic cell of this structure is ccp-fcc configuration shown furthest to the left in Figure 3.3. The three-dimensional unit cell of the aba-structure is the hexagonal closest packed structure (hcp) [17;18].These two structures in addition to the bcc structure are the most common; see Figure 3.3 [19].

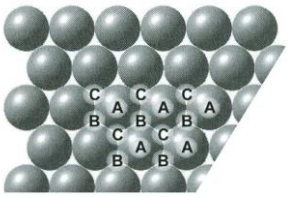

Figure 3.2 The closest packing arrangement of uniform spheres. The sites of the A atoms defines the bottom layer. The spheres B in the second layer occupy dimples in the first layer. The spheres in the third layer, C, occupy dimples in the second layer [19].

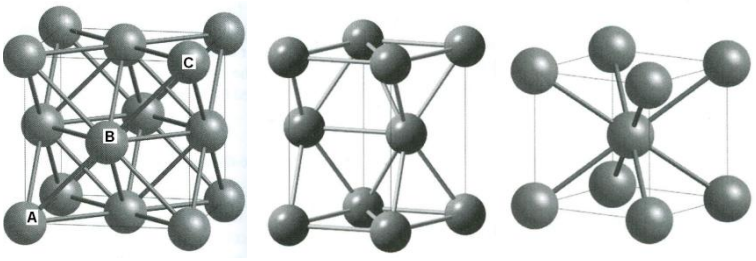

Figure 3.3 Three different unit cell structures. The left figure shows the cubic close packing, the fcc-packing (from abcabc structure) The letters denote layers shown in Figure 3.2. The mid figure shows the hexagonal, hcp-packing (from the ababab-structure). The right shows the bcc-packing [19].

Materials with the same chemical formula can have different phases, hence different packings and hence different properties. An example of such a material is the metal oxide Al_2O_3, with possible structures γ, α, κ etc. The phase of the material is written in front of the chemical formula, e.g γ-Al_2O_3.

3.3 Miller indexes

To define how a surface is cut from the bulk phase, Miller indexes are used. The plane spent out of the Miller indexes defines the structure of the surface and hence the adsorption properties. The Miller indexes are three integers, *h, l, and k*, defined as the inverse of the basis vectors in the unit cell, i.e.

$$h:k:l=\frac{1}{x_1}:\frac{1}{x_2}:\frac{1}{x_3} \tag{3.1}$$

where x_n is the axis in the direction n. Some examples of a cubic system are shown in Figure 3.4. The packing of the atoms combinded with the Miller indexes of the cutting plane will hence define the surface and the layers below. The cutting plane of a metal, alloy or metal oxide is in literature and for other purposes indicated after the chemical formula of the metal, for example Al(111) and Fe_2O_3(100).

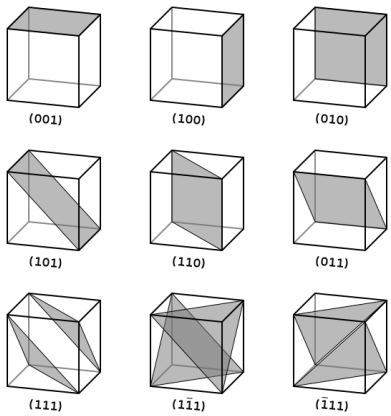

Figure 3.4 Four lattice planes and their Miller indexes [20].

4 Surfaces and interfaces

4.1 Flat interfaces

In this section we consider the thermodynamics of flat interfaces. For a description of the thermodynamics of curved interfaces, we refer to Ibach [21] or similar textbooks in surface physics.

Consider the two phases denoted by I and II illustrated in Figure 4.1a. Inside the bulk, the phases shall be in equilibrium. Following Ibach [21], we assume that phase I and II and the interfaces between them form an infinite periodic sequence along the z-axis with periodic boundary conditions. We further assume that the system is homogeneous in the (x, y) plane. The formed supercell has length L and area A, and the length of the supercell is so large compared to the extension of the interfaces so that the bulk of phase I and II are homogeneous. The supercell has a fixed and finite volume $V = AL$. Because of the periodic boundary conditions, the number of particles in the supercell is constant. We further assume that the external pressure is zero.

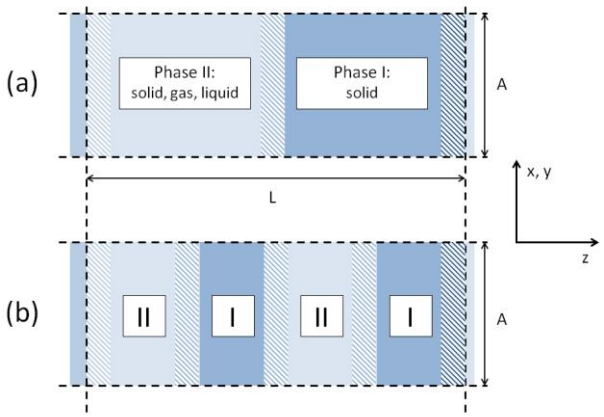

Figure 4.1 Illustration of flat interfaces. Phases are marked with solid color and interfaces with hatched pattern (after Ibach [21]).

The thermodynamic function appropriate for this system is the Helmholtz energy[3]. Again following Ibach [21], we define a Helmholtz energy for one supercell with two interfaces, denoted as $F^{(2)}(L)$. In order to define the Helmholtz energy associated with the formation of an interface, the periodicity length is reduced by a factor of two such that we have four interfaces instead of two within the supercell, Figure 4.1b. The Helmholtz energy associated with this system is denoted as $F^{(4)}(L)$ [21].

The Helmholtz energy associated with the introduction of the two additional interfaces is $F^{(4)}(L) - F^{(2)}(L)$. An interface Helmholtz energy ($F^{(s)}$) and area specific Helmholtz energy ($f^{(s)}$) can therefore be defined [21]:

$$f^{(s)} = F^{(s)}/A = \left[F^{(4)}(L) - F^{(2)}(L)\right]/2A \tag{4.1}$$

As discussed by Ibach [21], the advantage of this definition is that there is no need to specify where one bulk phase ends and the next one begins as is done in Gibbs thermodynamics with the Gibbs surface[4].

We will now go on to define the infinitesimal strain tensor, the stress tensor, and the particle number (or more appropriately, the surface excess number) for the interface. The state of strain in a solid is described by the dependence of the gradients of a displacement vector **u**, and the components of the second-rank infinitesimal strain tensor is given by [21]

$$\varepsilon_{ij} = \frac{1}{2}\left(\frac{\partial u_i}{\partial x_i} + \frac{\partial u_j}{\partial x_j}\right). \tag{4.2}$$

By definition, the tensor is symmetric where the diagonal elements are associated with change in volume, and the non-diagonal elements describe the shear distortion. Stresses and strains are related by Hooke's law

$$\tau_{kl} = \sum_{ij} c_{klij}\varepsilon_{ij}\,, \tag{4.3}$$

where τ_{kl} are components of the stress tensor and c_{klij} are the components of the stiffness tensor. Because of homogeneity and zero external pressure, the bulk components of the stress tensor vanish. Near the interface, however, the stress tensor may have non-vanishing components. The interface stress is defined as [21]

$$\tau_{kl}^{(s)} = \int_{\text{interface}} \tau_{kl}(z)\mathrm{d}z\,, \tag{4.4}$$

[3] Formerly called Helmholtz free energy.

[4] Gibbs surface is a geometrical surface chosen parallel to the interface and used to define the volumes of the bulk phases in the calculation of the extent of adsorption, and of other surface excess properties. The Gibbs surface is also referred to as Gibbs dividing surface or Gibbs dividing plane [10].

where the indices k,l = 1,2 denote the in-plane components of the stress tensor. The insertion of additional interfaces into the supercell may cause bulk species to flow towards or away from the interface, thus changing the particle density at the interface. For the interface, the particle number is replaced by the surface excess number $n_i^{(s)}$, defined as the integral over the z-dependent densities ($\rho_i(z)$) minus the bulk densities [21]:

$$n_i^{(s)} = A\int_{\text{interface}}\left[\rho_i(z) - \rho_{\text{I,II}}\right]\mathrm{d}z \tag{4.5}$$

The Helmholtz energy for the interface ($F^{(s)}(T, \varepsilon_{kl}, n_i^{(s)})$) can now be written as [21]

$$F^{(s)}(T,\varepsilon_{kl},n_i^{(s)}) = U^{(s)} - S^{(s)}T + A\sum_{kl}\tau_{kl}^{(s)}\varepsilon_{kl} + \sum_i \mu_i n_i^{(s)}\,, \tag{4.6}$$

where $U^{(s)}$ is the internal energy of the interface, $S^{(s)}$ is the entropy of the interface, μ_i is the chemical potential of particles of type i in the system, and T is the temperature. The total differential of the Helmholtz energy of the interface is given by

$$\mathrm{d}F^{(s)} = -S^{(s)}\mathrm{d}T + A\sum_{kl}\tau_{kl}^{(s)}\mathrm{d}\varepsilon_{kl} + \sum_i \mu_i \mathrm{d}n_i^{(s)}\,. \tag{4.7}$$

The indices k,l denote the x and y components of the surface stress and strain tensors. There is no contribution to the mechanical work from the z-component since the external pressure is zero [21]. The last term describes the chemical work associated with bringing $\mathrm{d}n_i$ particles with a chemical potential μ_i into the system.

4.2 Solid-solid and solid-liquid interfaces

As an example of the thermodynamics of flat interfaces, let us consider solid-solid and solid-liquid interfaces. That is, phases which have a line of contact in common. This situation can be illustrated as depicted in Figure 4.2a. Following Ibach [21], we assume for a moment that the interface tensions are independent of the orientations of the interfaces. The interfaces are in equilibrium if the total interface energy is stationary against a variation of the contact angles. Let us introduce a "virtual" displacement of the line of contact in any arbitrarily chosen direction, as illustrated by the vector **s** in Figure 4.2a. Note that the virtual displacement compares different sets of contact angles; it should not be interpreted as an elastic deformation. The condition that the total interface energy of the three phases is stationary with respect to the virtual displacement **s**, requires that

$$\sum_i \gamma_i \cos\alpha_i = 0\,, \tag{4.8}$$

where γ_i is the surface tension and α_i is the angle between the interface i and the direction of **s** [21]. If we consider crystalline solids, the surface tension depends on the orientation, thus contributing a second term to each variation in the interface tensions [21]:

$$\Delta\gamma_i = \frac{\partial\gamma_i}{\partial\theta_i}\Delta\theta_i \tag{4.9}$$

Here, $\Delta\theta_i$ is the rotation of the orientation of interface *i* because of the virtual displacement **s** (see Figure 4.2a). For this situation, the condition that the interface energy is stationary is then [22]

$$\sum_i \left(\gamma_i \cos\alpha_i + \frac{\partial\gamma_i}{\partial\theta_i}\sin\alpha_i \right) = 0 \tag{4.10}$$

As an example, consider the deposit of a solid or a liquid on a flat surface as illustrated in Figure 4.2b. For this situation, eq. (4.8) turns into the Young-Dupré equation [21]:

$$\gamma_i + \gamma_{\text{dep}} \cos\alpha = \gamma_s\,, \tag{4.11}$$

where γ_s, γ_{dep}, and γ_i are the surface tension of the solid substrate, the surface tension of the deposit, and the interface tension between the substrate and the deposit, respectively. For simplicity, we have assumed that the surface of the deposit is "rough" near the line of contact so that $\partial\gamma_{\text{dep}}/\partial\theta \ll \gamma_{\text{dep}}$. If $\gamma_i + \gamma_{\text{dep}} < \gamma_s$, the Young-Dupré equation (eq. (4.11)) is not satisfied for any contact angle, and the substrate will be completely wetted by the deposit and growth will be in a layer-by-layer manner (so-called Frank-van-der-Merwe growth). On the other hand, if $\gamma_i + \gamma_{\text{dep}} > \gamma_s$, growth will be in the form of 3D-clusters (so-called Vollmer-Weber growth) [21].

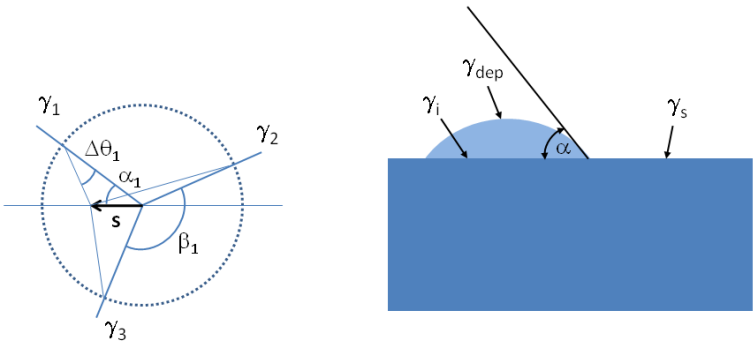

Figure 4.2 (a) Illustration of three phases that share a common line perpendicular to the plane of drawing. (b) Contact angle of a solid cluster or a liquid on the flat surface of a substrate. See text for details (after Ibach [21]).

4.3 Solid-gas interfaces: Lattice gas models

We now go on to describe how the thermodynamics of the adsorption of a gas on an adsorbent can be described in terms of so-called lattice gas models. For simplicity, let us consider *N* atoms chemically adsorbed (chemisorbed) to a crystalline surface. The atoms are chemisorbed at defined surface sites for the crystalline surface. These sites have a periodic structure; see Figure 4.3. Such

a model dealing with the occupation of a periodic arrangement of M equivalent adsorption sites is called a *lattice gas model* [21].

In the simplest lattice gas model, it is assumed that there is only one type of sites and that the adsorption energy for a site is independent of the occupation of neighboring sites, that is, a mean field interaction is assumed. Thus, the partition function of an adsorbed species (q_{ads}) is independent of the configuration of the other adsorbates. This model is called *non-interacting lattice gas*. In the non-interacting lattice gas model the allowed occupation numbers for each site i are $n_i = 0$ and $n_i = 1$. It can be shown that the mean occupation number ($\langle n \rangle$) per site is given by [21]

$$\langle n \rangle = \theta_{\text{ads}} = \left[1 + \exp\left(E_{\text{ads}} - \mu_{\text{ads}}\right)/k_{\text{B}}T\right]^{-1}, \tag{4.12}$$

where E_{ads} and μ_{ads} are the energy of the adsorbate and its chemical potential, respectively, k_{B} is the Boltzmann constant, and T is the temperature. The mean occupation number is the same as the coverage of adsorbates (θ_{ads}). Rearrangement of eq. (4.12) gives the following expression for the chemical potential of the adsorbate:

$$\mu_{\text{ads}} = E_{\text{ads}} + k_{\text{B}}T \ln\left(\frac{\theta_{\text{ads}}}{1-\theta_{\text{ads}}}\right). \tag{4.13}$$

As discussed by Ibach [21], adsorbed species may have low-lying vibrational frequencies so that the vibrational partition function for the adsorbate ($q_{\text{ads,vib}}$) differs from unity. The chemical potential of the adsorbate for this situation is

$$\mu_{\text{ads}} = E_{\text{ads}} + k_{\text{B}}T \ln\left(\frac{\theta_{\text{ads}}}{1-\theta_{\text{ads}}}\right) - k_{\text{B}}T \ln q_{\text{ads,vib}}\,. \tag{4.14}$$

According to Ibach [21], the non-interacting lattice gas model is a good approximation to adsorption isotherms (see e.g chapter 5.2), but fails to describe the evolution of different phases as a function of the adsorbate coverage and transitions between various phases.

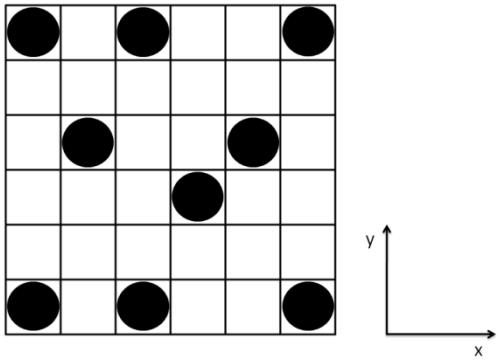

Figure 4.3 Illustration of a non-interactive lattice gas model. Open squares represent available and equivalent adsorption sites and black circles represent adsorbed species. Coverage = 0.25.

The lattice gas model described above can be extended to include adsorbate interactions. The Hamiltonian (H) for this system can be described by [23;24]

$$H = \sum_{i=1}^{N} H_i + \sum_{l} w_l \sum_{j,k} n_{lj} n_{lk} \,, \tag{4.15}$$

where H_i is the Hamiltonian of an isolated adsorbate i (equivalent for all adsorbates) , $w_l = w_1$, w_2, w_3, etc. are the interaction energies due to the occupation of the nearest neighbor, next-nearest neighbor, third-nearest neighbor sites, and so on, and n_{lj}, n_{lk} are 1 if the sites j, k of type l are occupied, 0 if not [24]. The Hamiltonian given by eq. (4.15) does not include diffusion, adsorption, or desorption of species. In the non-interacting lattice gas model $w_l = 0$ for all l and the total partition function for the N adsorbates is given by [24]

$$Q(N,M,T) = \frac{M!\, q_{\text{ads}}(T)^N}{N!(M-N)!}. \tag{4.16}$$

When adsorbate interactions are included, the partition function is given formally by

$$Q(N,M,T) = q_{\text{ads}}(T)^N \sum_{c} g_c(N,M) \exp(-E_c / k_{\text{B}} T) \,, \tag{4.17}$$

where $g_c(N,M)$ is the temperature-independent number of ways N adsorbates can be distributed among M adsorption sites for any configuration of adsorbates c, and E_c is the energy of the configuration. Because of the very large number of configurations possible for any moderately large N and M, an exact evaluation of eq. (4.17) cannot be obtained. One therefore has to rely on either numerical techniques or approximations like the *Bragg-Williams approximation* where a coverage-dependent energy term ($W(\theta_{\text{ads}})$) is added to the expression for the chemical potential of the adsorbated [21]:

$$\mu_{ads} = E_{ads} + k_B T \ln\left(\frac{\theta_{ads}}{1-\theta_{ads}}\right) - k_B T \ln q_{ads,vib} + W(\theta_{ads}) \tag{4.18}$$

A positive $W(\theta_{ads})$ corresponds to repulsive interactions between the adsorbed species, while a negative $W(\theta_{ads})$ corresponds to attractive interactions.

5 Adsorption

5.1 Physical and chemical adsorption

The strength of adsorption can be found from the adsorption or bonding energy, E_{ads}. The size of the bonding energy divides the phenomena into physisorption and chemisorption, where the first has much lower bonding energy than the second [25]. This energy is given as the sum of each single component minus the energy of the whole system. The larger E_{ads}, the stronger bonding between the adsorbate and adsorbent.

$$E_{ads} = E_{tot,substrat} + E_{tot,atom} - E_{tot,adatom/substrat} \tag{5.1}$$

5.1.1 Physisorption

Physisorption is the weakest form of adsorption; no chemical bonds are created. Physical adsorption is a result of attractive van der Waals interaction and a repulsive[5] potential close to the surface.

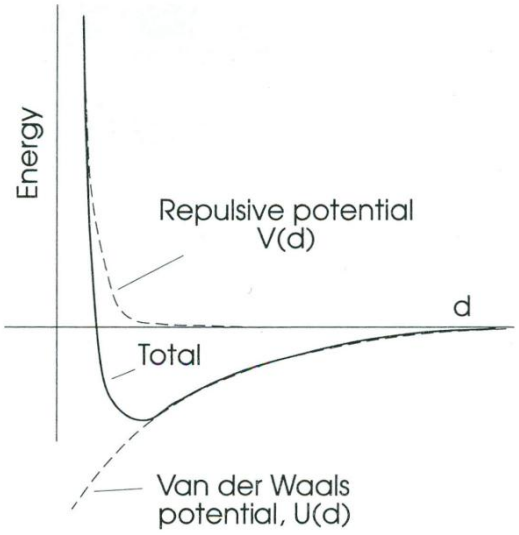

Figure 5.1 Illustration of the physisorption potential [26].

[5] Repulsive due to the Pauli principle: no fermions (here electrons) can be in the same quantum state.

Van der Waals interaction is given by

$$V_{\mathrm{vdW}} = -\frac{C}{|z - z_0|^3} \tag{5.2}$$

where C is the Van der Waals constant and z is the distance from the surface z_0 [27].

The repulsive potential can be written as [28]

$$V_{\mathrm{R}}(z) = V_0 e^{-\alpha z} \tag{5.3}$$

V_0 is the strength, and α is the repulsive potential.

The total physical potential is then

$$V_{\mathrm{phys}}(z) = V_{\mathrm{vdW}}(z) + V_{\mathrm{R}}(z) \tag{5.4}$$

Figure 5.1 show the potentials above the surface. As can be seen the total potential has no positive values. There is no barrier towards adsorption [27].

5.1.2 Chemical adsorption

In chemical adsorption the bonding energy is much larger than for physical adsorption and true chemical bonds exist. Energy must be added to achieve the reaction, but the total reaction is exothermic.

Different models can be used to describe chemical adsorption. This section will give a short introduction to some of them. To show the use of the models single atoms and simple molecules adsorbing on pure metals are chosen for illustration. The examples can be extended to larger molecules.

The molecule can either be bonded as a whole molecule or it can dissociate and bond as fragments or reacted with other species. Whether the molecule bonds unseparated or not can be discussed in terms of the Lennard-Jones potential model, see Figure 5.2.

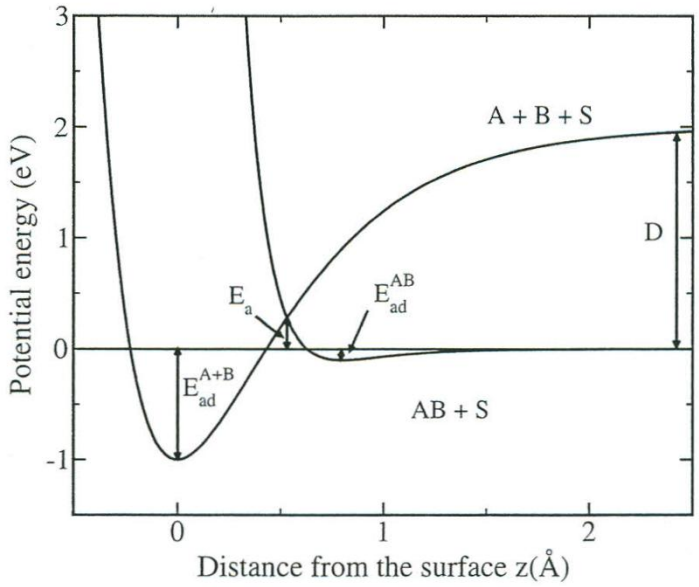

Figure 5.2 Potential energy curves for molecular and dissociative adsorption according to Lennart-Jones [29].

Curve "AB+S" describes the potential energy for a molecule "AB" which moves towards the surface "S". The curve has a shallow minimum before it rises steeply. "A+B+S" describe the potential energy for the separate atoms A and B moving towards the same surface. Far from the surface the molecule as its whole is energetically favourable. Close to the surface the dissociated molecule is favourable. The crossing of the two lines is the activation energy needed to separate the molecule [29].

5.1.2.1 The Blyholder model

In 1964 Blyholder proposed a model which characterized chemical adsorption by identifying the lowest unoccupied molecule orbital (LUMO) and the highest molecule occupied orbital (HOMO). HOMO and LUMO are most active orbitals in the bonding mechanism. The reaction between an adsorbate and an adsorbent can hence be predicted from these two orbitals.

The bondig orbitals of two molecules O_2 and CO are shown in Figure 5.3. Empty, lined and crossed spheres denote empty, half filled and filled orbitals respectively. O_2 has filled 5σ and 1π molecular orbitals. The anti-bonding 2π orbital is half filled and makes O_2 paramagnetic and unstable. In O_2 2π is the HOMO orbital, wheras 6σ is the LUMO orbital.

The orbital structure for CO is completely different. Different atomic energy levels make C and O only bond in the 4σ and the 1π orbital. The 5σ orbital is higher in energy than the highest filled level in atomic O. The two electrons in 5σ, localized at the carbon end of the molecule, are therefore non-bonding. In the CO molecule the HOMO and LUMO orbital is the 5σ and the symmetric 2π orbital respectively [27].

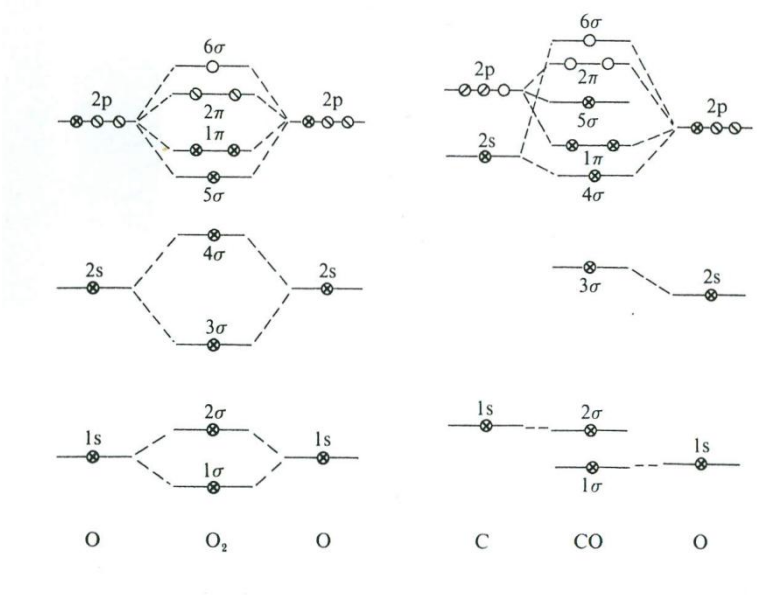

Figure 5.3 Schematic molecular orbital diagrams for O_2 and CO. Empty, lined and crossed spheres denote empty, half filled and filled orbitals, respectively [30].

Due to the closed electron structure in CO the bonding energy is high (11.23 eV) and CO will remain as a whole molecule when it gets closer to the surface. However, by adsorption the carbon part of the molecule will face towards the surface so that 5σ "donates" its electrons to the substrate. By adsorbing of CO the 5σ orbital donates its electrons to the metals d-orbital. To retain the charge balance some of the electrons from the d-orbital are donated to the 2π-orbital. This weakens the CO bond and strengthens the metal–carbon bond. The lower-lying 4σ and 1π remain filled [27]. The orbital energy is lowered and energy is hence gained. Oxygen has half filled orbitals and a bonding energy of 5.2 eV only. Therefore, energy lost by breaking the intermolecular bond usually can be more than compensated for by local bonding of two separate O atoms. [30]

5.1.2.2 The News-Anderson model

This model divides between chemical adsorption on metals induced from electrons in so-called sp-bands and electrons in d-bands. When an atom or a molecule adsorb on a surface with sp-bands only, the interaction results in a broadening and a down-shift of the energy of the orbitals. Figure 5.4 shows how the local density changes after interaction with a sp-metal. The main peak has moved further down on the energy axis and is broadened. If the substrate is a transition metal with electrons in the d-orbital, the orbitals will be divided into two resonances, one bonding and one antibonding state. If the topmost peak is below the d bands energy limit, the filling of the anti-bonding state will depend on how full the d band is. Adsorbate-substrate bonds with one single resonance and double peaks are often called "weak chemical and strong adsorption" respectively.

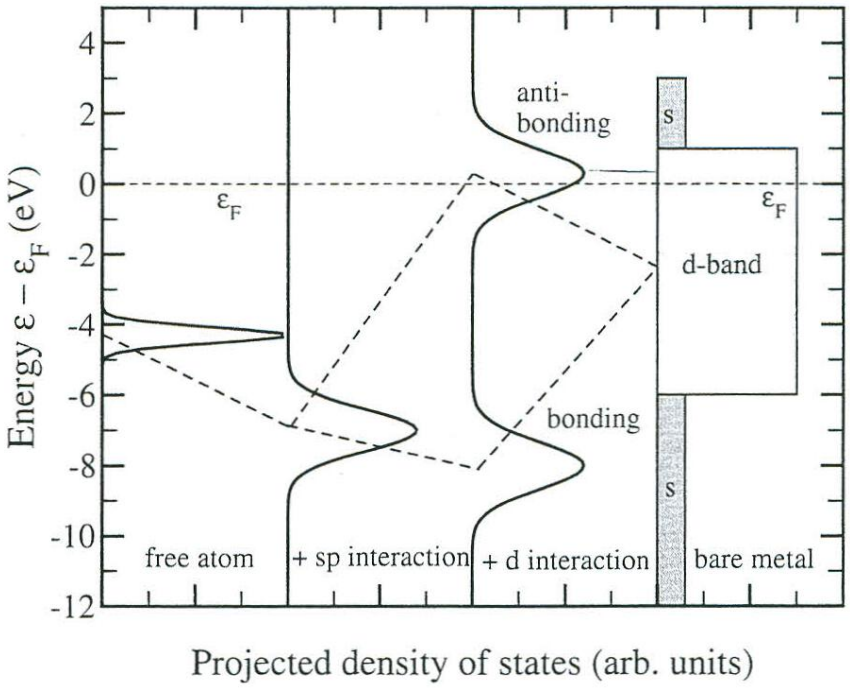

Figure 5.4 Sketch of the interaction of an atomic level with a d-metal (transition metal) [27].

5.1.2.3 Nørskov-Hammer model

This model is valid for d-metals only and explains how the adsorbate bonds to the metals d-band. The bonding strength is determined by the numbers of anti-bonding adsorbate-metal d-states and the strength of the bond between the metal and adsorbate. The interaction between a d-metal and an adsorbate normally decreases moving to the right and/or downwards in the periodic table.

By moving to the left in the periodic table, more anti-bonding states are empty and the d-band moves up in energy. By moving to the right in the periodic table, the d-band is lowered in energy and more anti-bonding states will be filled. More anti-bonding atomic level states will hence be filled by adsorption at e.g. Cu/Ag/Au than at Ni/Pd/Pt giving a weaker bonding.

After adsorption molecular orbitales will, due to the Pauli principle, arrange themselves orthogonal to the metals d-states. This leads to an increase (the square of the coupling between the adsorbate and the metal d-band) in kinetic energy, which again increase the repulsion due to the Pauli principle. For a fixed adsorbate the energy increase only depends on the broadening of the band. The further down in the periodic table, the broader the bond (5d is broader than 4d which is broader than 3d), the bigger the increase in energy, the less favorable for an adsorbate to adsorb on the surface [27].

5.2 Adsorption isotherms

An important concept in adsorption is the adsorption isotherm. The adsorption isotherm is the equilibrium between the quantity of the adsorbed material and the pressure (if gas) or concentration (if fluid) in the bulk fluid phase at constant temperature [31].

From the benefit of understanding the mechanism of the adsorption phenomenon the need of a mathematical model of adsorption isotherms arises. A pure theoretical isotherm equation is desired to be able to explain and predict exactly what happens between a solid surface and the gas phase. Different equations have been made trying to cover the experimental adsorption data. Such equations are called adsorption isotherms. However, no equation today can describe the microscopic adsorption system precisely, but many of the properties of the adsorption system can be calculated and regarded as reliable based on isotherms [27;32].

This section offers an overview over some of the most important adsorption isotherms and describes the basic theory behind them.

5.2.1 Freunlich and Küster

One of the first mathematical descriptions of an adsorption isotherm is the Freunlich and Küster equation

$$\frac{x}{m} = \kappa P^{\frac{1}{n}} \tag{5.5}$$

Here, x is amount adsorbed, m is the weight of the adsorbent (x/m is hence the concentration of the adsorbed species), P is the equilibrium adsorption pressure of the gas. If the adsorbate is a liquid, P represents the equilibrium adsorption concentration. κ and n are constants varying with each adsorbate-absorbent system [33].

5.2.2 Henry's law

One of the simplest adsorption isotherms is Henry's law from 1803 [34]. In this isotherm the amount adsorbed is assumed to vary with the equilibrium pressure (or concentration) of the adsorbate only. Both the gas and the adsorbed phase are dilute enough to be considered as perfect. The adsorption term can hence be written as

$$c = p\frac{ad}{RT}\frac{w_2}{w_1}e^{E/RT} = p \cdot \text{constant}(T) \tag{5.6}$$

Here, c is the amount adsorbed (mol/m^2), p the equilibrium pressure, a the fraction of the solid surface available for adsorption, d the thickness of the adsorbed layer, w_1 and w_2 are the weights for the internal energies of the molecules in the gas and adsorbed phase, respectively, and E is the adsorption potential energy assumed to be constant (R and T are the gas constant and the temperature, respectively). Several more complicated theoretical isotherms simplify to the linear Henry's law at low pressures [35].

5.2.3 Langmuir – molecular adsorption

The Langmuir equation describes monolayer adsorption on an energetically homogeneous surface. Langmuir assumed that the forces acting by adsorption are equal to those causing chemical bondings [36]. The adsorptive forces are concentrated on points or elementary spaces at the sur-

face; the adsorption sites are energetically equivalent. The adsorbates are fixed at these areas for a certain time and each of these points can hold only one adsorbed species. The adsorbed layer can hence only be a monolayer [37]. No pores are present. Further the adsorbed gas is described as an ideal gas and lateral interactions among the adsorbates are neglected. Even though this is an extreme simplification, the Langmuir equation describes relatively well adsorption (both physical and chemical) adsorption on solid surfaces with one type of adsorption active centre and low pressure [31;35;37].

There are several ways to derive the Langmuir isotherm. Below follows a short overview of one possibility, other ways of deduction can e.g. be found in Ibach [21].

In the early stages of the adsorption process, only one part, θ_{ads}, of the surface is covered with adsorbed molecules [31;35-37]:

$$\theta_{ads} = \frac{\text{number of occupied states}}{\text{total number of possible states } (n)} \tag{5.7}$$

The rate of adsorption, r_{ads}, is then proportional to $(1 - \theta_{ads})$. The rate is also proportional to the flux of molecules or atoms, F, striking the surface. From kinetic theory this flux is given as

$$F = \frac{p}{\sqrt{2\pi m k_B T}} \tag{5.8}$$

where p, m, k_B and T is pressure of the gas, the atomic/molecule mass, the Boltzman constant and the temperature respectively. The fraction α of molecules actually bonding to the surface must also be included and the rate of adsorption can then written as

$$r_{ads} = \frac{\mathrm{d}\theta_{ads}}{\mathrm{d}t} = \alpha F(1-\theta_{ads}) \tag{5.9}$$

The rate of desorption is $r_{des} = \xi\theta_{ads}$, where ξ is the rate of evaporation from a fully covered surface. At equilibrium the adsorption rate is equal to the desorption rate

$$\begin{aligned} r_{ads} &= r_{des} \\ \alpha F(1-\theta_{ads}) &= \xi\theta_{ads} \\ \theta_{ads} &= \frac{\alpha F}{\xi + \alpha F} \end{aligned} \tag{5.10}$$

For low temperatures the evaporation rate will be low and the amount adsorbed will be high. This is consistent with adsorption being an exothermic process. By lowering the temperature, more adsorbates will be adsorbed so that energy is gained to counteract the temperature depression.

By combining eq. (5.8) and eq. (5.10) and defining

$$\frac{\alpha}{\xi\sqrt{2\pi k_{\mathrm{B}}T}} = K \tag{5.11}$$

the equilibrium between condensation and evaporation can be written as

$$Kp = \frac{\theta_{\mathrm{ads}}}{1-\theta_{\mathrm{ads}}} \tag{5.12}$$

Eq. (5.12) can then be rewritten as

$$\theta_{\mathrm{ads}} = \frac{Kp}{1+Kp} \tag{5.13}$$

which is the familiar Langmuir isotherm. For a solid-liquid system p is replaced by the molar concentration of the solution [35].

Since the number of adsorbate atoms/molecules at high pressures will be much larger than the number of adsorption sites, the Langmuir isotherm is thermodynamically inconsistent [32]. Even at high pressures θ_{ads} cannot exceed one:

$$\lim_{p\to\infty} \theta_{\mathrm{ads}} = 1 \tag{5.14}$$

At low pressures

$$\lim_{p\to 0} \theta_{\mathrm{ads}} = Kp \tag{5.15}$$

which is of the same form as Henry's law (see section 5.2.2) [35].

The value θ_{ads} can be difficult to measure experimentally, hence it favourable to introduce the quantities v and v_{max} that are the volumes adsorbed at pressure p and infinite pressure, respectively. It is then possible to write:

$$\theta_{\mathrm{ads}} = \frac{v}{v_{\mathrm{max}}} \tag{5.16}$$

Eq. (5.16) can be written as

$$v = \frac{v_{\mathrm{max}} Kp}{1+Kp} \tag{5.17}$$

Rearranged, this is the same as

$$\frac{p}{v} = \frac{p}{v_{\max}} + \frac{1}{Kv_{\max}} \tag{5.18}$$

Eq. (5.18) can now be used to find $v_{\max}$ and K for each induviduale adsorbate/adsorbent system. By plotting p/v vs. p, a straight line should occur with slope $1/v_{\max}$ and intercept $1/Kv_{\max}$. The number of adsorption sites at surface is through the ideal gas law related to $v_{\max}$. This Langmuir method has successfully been applied to different adsorbates on e.g. charcoal or silica gel. The equation has been less suitable for non-porous systems [35]. In the next subsections follow some additions involving lateral interactions to the Langmuir equation.

5.2.3.1 Fowler-Guggenheim – lateral interactions

One of the most common extensions of Langmuir is the Fowler-Guggenheim equation which extends the Langmuir equation to involve the molecular interactions between the adsorbed molecules

$$Kp = \frac{\theta_{\text{ads}}}{1-\theta_{\text{ads}}} e^{-\bar{z}u\theta_{\text{ads}}/k_{\text{B}}T} \tag{5.19}$$

where u is the interaction energy between the adsorbed molecules and $\bar{z}$ is the average number of nearest neighbours in the gas lattice. The Fowler-Guggenheim equation is valid for homogenous surfaces and is based on the Bragg-Williams approximation. In this approximation the configuration degeneracy and the average nearest neighbour interaction energy are both handled on the basis of a totally random distribution of the molecules among lattice sites (see ref. [32] and references therein).

The Fowler-Guggenheim isotherm assumes independent homogeneous patches at the surface. That is, the substrate is divided into several homogenous domains. The interactions between molecules adsorbed on different patches are excluded [32].

In eq. (5.19) it is assumed totally random distribution. However, the interaction energy will make the adsorbates aggregate. A less primitive approximation shown in ref. [35], is to only assume quasi-chemical equilibrium between three types of nearest neighbour sites: filled-filled, filled-vacant, and vacant-vacant. The adsorption isotherm is then

$$Kp = \frac{\theta_{\text{ads}}}{1-\theta_{\text{ads}}} \left(\frac{2-2\theta_{\text{ads}}}{\chi + 1 - 2\theta_{\text{ads}}} \right)^{z} \tag{5.20}$$

where

$$\chi = \left[1 - 4\theta_{\text{ads}}(1-\theta_{\text{ads}})(1-e^{u/kT}) \right]^{1/2} \tag{5.21}$$

Setting u to zero reduces both eq. (5.19) and (5.20) to the original Langmuir isotherm.

5.2.3.2 William and Henry's isotherm - dissociation

William and Henry modified the Langmuir equation by assuming that each adsorbed molecule occupies *q* adjacent sites. The adsorption rate is hence

$$r_{\text{ads}} = \frac{\mathrm{d}\theta_{\text{ads}}}{\mathrm{d}t} = \alpha\mu(1-\theta_{\text{ads}})^q \tag{5.22}$$

The isotherm follows as

$$\theta_{\text{ads}} = \frac{Kp^{1/q}}{1+Kp^{1/q}} \tag{5.23}$$

If the adsorbate molecule for example dissociates into two atoms and each atom occupies one site, $q = 2$ [35].

5.2.4 The BET equation – multilayer adsorption

Molecules and atoms often adsorb in multilayers. The Langmuir monolayer equation is then no longer valid. The BET equation, a multilayer development of the Langmuir isotherm, was proposed by Brunauer, Emmett, and Teller in 1938 [38]. The first adsorption layer is assumed to be formed on an array of surface sites with equal energy. This assumption is the same as used in the Langmuir equation. Each adsorbed molecule in the first layer act as an adsorption site in the second layer and so on. The BET equation (in conformity with the Langmuir equation) ignores mutual interaction between adsorbed species. The areas s_0, s_1, s_2, s_3,…, s_i,… are covered with 0, 1, 2, 3,…, i,… adsorbate layers, respectively. From the second layer and upwards the heat of condensation is assumed to be the same for all layers. The following derivation of the BET isotherm follows reference [35].

At equilibrium the rate of condensation to s_0 is equal to the evaporation rate from s_1:

$$a_1 p s_0 = b_1 s_1 e^{-E_1/RT} \tag{5.24}$$

Here, a_1 and b_1 are constants, p is the pressure, and E_1 is the adsorption heat in the first layer.

The general statement between two layers on top of each other, $(i-1)$ and i, can be written as

$$a_i p s_{i-1} = b_i s_i e^{-E_i/RT} \tag{5.25}$$

E_i here denotes the heat of liquification/condensation; this value is the same for all layers above the first

$$E_2 = E_3 = \ldots = E_i = E_L \tag{5.26}$$

where L denotes the top layer. Additionally, the BET equation assumes that

$$\frac{b_2}{a_2} = \frac{b_3}{a_3} .... = \frac{b_i}{a_i} \tag{5.27}$$

The total surface area, A, covered with adsorbates is

$$A = \sum_{i=0}^{i=\infty} s_i \tag{5.28}$$

and the total volume of adsorbed gas is then

$$v = v_0 \sum_{i=0}^{i=\infty} i s_i \tag{5.29}$$

where v_0 is the volume adsorbed per unit surface when the unimolecular layer is totally filled. Eq. (5.29) divided by eq. (5.28) gives

$$\frac{v}{A v_0} = \frac{v}{v_{\max}} = \frac{\sum_{i=0}^{i=\infty} i s_i}{\sum_{i=0}^{i=\infty} s_i} \tag{5.30}$$

where $v_{\max}$ is the volume of the monolayer as in section 5.2.3.

By defining two variables y and x as

$$\begin{aligned} y &= \frac{a_1}{b_1} p e^{E_1/RT} \\ x &= \frac{a_2}{b_2} p e^{E_L/RT} \end{aligned} \tag{5.31}$$

eq. (5.24) can be written

$$s_1 = y s_0 \tag{5.32}$$

Correspondingly, for $i > 2$, eq. (5.25) can be simplified to

$$s_i = x(s_{i-1}) = x(x s_{i-2}) = x^{i-1} s_1 = x^{i-1} y s_0 = c x^i s_0 \tag{5.33}$$

where

$$c = \frac{y}{x} = \frac{a_1 b_1}{a_2 b_2} e^{(E_1 - E_L)/RT} \tag{5.34}$$

By inserting eq. (5.33) into eq. (5.30), the relation

$$\frac{v}{v_{\max}} = \frac{cs_0 \sum_{i=1}^{i=\infty} ix^i}{s_0 \left[1 + c\sum_{i=1}^{i=\infty} x^i\right]} \tag{5.35}$$

occurs, which after use of summation rules for rows results in

$$\frac{v}{v_{\max}} = \frac{cx}{(1-x)(1-x+cx)} \tag{5.36}$$

At saturation, $p = p_0$. Thus, the number of layers adsorbed and hence v is infinite. From eq. (5.36) it is obvious that v is infinite when x→1.

$$x = \frac{a_2}{b_2} pe^{E_L/RT} = 1 \tag{5.37}$$

which is the same as

$$x = p / p_0 \tag{5.38}$$

Substituting eq. (5.38) into eq. (5.36) gives

$$v = \frac{v_{\max} cp}{(p_0 - p)\,1 + (c-1)p / p_0} \tag{5.39}$$

This can be rewritten as

$$\frac{p}{v_{\max}(p - p_0)} = \frac{1}{v_{\max}} + \frac{(c-1)}{v_{\max} c} \frac{p}{p_0} \tag{5.40}$$

Eq. (5.40) can be used for drawing a plot of $p/[v_{\max}(p - p_0)]$ vs. p/p_0. The slope is then $(c - 1)/(v_{\max}c)$, and the intercept is $1/(v_{\max}c)$. The values of both c and $v_{\max}$ can then be found. The value of c is from eq. (5.34) related exponentially to the difference between the heat of liquification, E_L, and the heat of adsorption, E_1, in the first layer, that is; the "net heat" of adsorption.

$$c = e^{(E_1 - E_L)/RT} \tag{5.41}$$

The BET equation should be used for $c < 200$. However, the c value should not be used for finding the value of the adsorption enthalpy, rather the magnitude of the adsorbate-adsorbent interaction [39]. The isotherm is a good description for adsorption in the relative pressure areas of 0.05–0.35. At lower and higher pressures it predicts too small and too high adsorption values respectively [31].

The total surface area, A_s, of the adsorbent is found from

$$A_s = v_{max} N_A a_{max} \tag{5.42}$$

where N_A is the Avogadro number. In addition the average area a_{max} covered of each adsorbate in the complete monolayer must be known and is assumed to be independent of temperature. The BET equation is hence often used for measuring surface area [40].

5.2.4.1 Porous materials

Adsorption isotherms involving filling of micropores are complex. A short introduction to the BDDT equation will follow to introduce the common five different classifications of adsorption isotherms.

An extension to the BET equation was in 1940 proposed by Brunauer et al. [41]. Their isotherm was called BDDT and included the additional contribution from forces of capillary condensation (pore spaces become filled with condensed adsorbate gas). The isotherm can be applied to a wide range of relative pressures. The equation is rather complex with four adjustable parameters that must be determined depending on each other [31;35]. From these it is possible to divide adsorption isotherms into five different classifications, the BDDT classification, see Figure 5.5. This is recommended as the basis for a more complete classification of adsorption isotherms introduced by IUPAC [31;39].

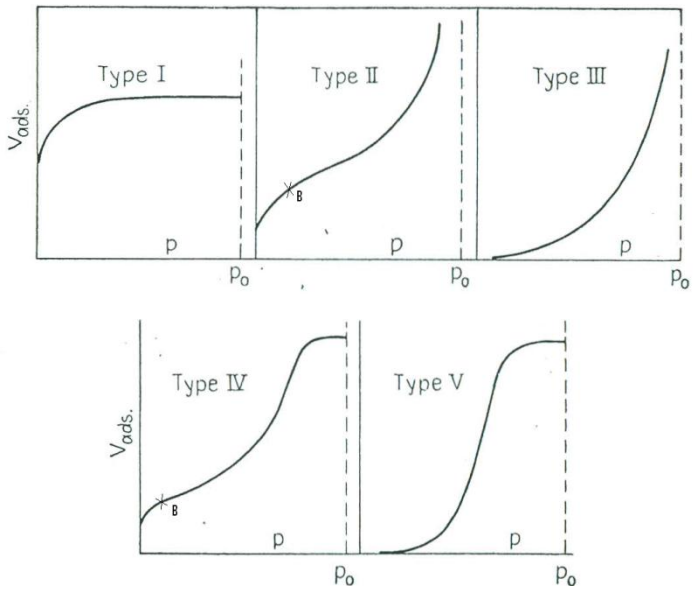

Figure 5.5 The five different types of adsorption from the BDDT equation: type 1 adsorption of oxygen on carbon at –183 °C, type II nitrogen on iron catalysts at –195 °C, type III bromine at silica gel, type IV benzene on ferric oxide gel at 50 °C, and type V water vapour on carbon at 100 °C. B denotes the point where monolayer adsorption is completed [37].

The five different types of isotherms is briefly described in ref. [39]. When describing different type of adsorbents, porous materials are divided into three main types. Macropores, mesopores and micropores have pore widths > 50 nm, 2–50 nm, and < 2 nm, respectively.

- The type I isotherms is concave to p/p_0 and approaches a limiting value for $p \to \infty$. Adsorbates in this group are microporous (pores < 2 mm) materials with relatively small external surface (i.e. activated carbon, certain porous oxides and molecular zieves like zeolites). This isotherm is often referred to the Langmuir isotherm. This can be somewhat misleading; many experiments show that the limiting uptake is determined by the accessible micropore volume and not the internal surface area, excluding the Langmuir theory.
- The isotherm shown in curve II is valid for non-porous and macroporous adsorbents. The curve shows an infinite mono-multilayer adsorption. Point B is used to indicate the stage at which the monolayer capacity is complete.
- Isotherm III is convex to the *p*-axis and there is no point B. This isotherm uncommon, but is valid for i.e. nitrogen on polyethylene. Adsorbate-adsorbate interactions are assumed to be strong in this type of adsorption.
- Type IV isotherms are valid for many mesoporous industrial adsorbents. The characteristic of this isotherm is the hysteris loop arriving from condensation in the mesophores. At high p there is a limiting value of amount adsorbed. The initial part is the same as in isotherm II, with point B indicating filled monolayer.
- Isotherm V is uncommon, but can be found from some porous materials. The isotherm follows from the assumption of weak adsorbate-adsorbent interactions, and stronger interactions between the adsorbates.

6 Desorption

6.1 Kinetics

In this section we will focus on the kinetics of the desorption process. We start by considering the adsorption and desorption of a molecule M (adsorbate) onto and from a solid surface with area *A* (adsorbent), enclosed in a container of volume *V*. Let us then denote the surface and gas-phase concentrations of species M by $[\mathrm{M}]_{\mathrm{surf}}$ and $[\mathrm{M}]_{\mathrm{gas}}$, respectively. The rate of desorption (r_{des}) is then given by

$$r_{\mathrm{des}} = \frac{\mathrm{d}[\mathrm{M}]_{\mathrm{surf}}}{\mathrm{d}t} = -k_{\mathrm{des}}[\mathrm{M}]_{\mathrm{surf}} \,, \tag{6.1}$$

where k_{des} is the desorption rate coefficient for the process $\mathrm{M}_{\mathrm{surf}} \to \mathrm{M}_{\mathrm{gas}}$.

It is, however, important to realize that k_{des} is not necessarily independent of $[\mathrm{M}]_{\mathrm{surf}}$ as is the case for the unimolecular rate coefficient for gas-phase reactions. The reason for this is that other adsorbed molecules may, in general, exercise both entropic and enthalpic influences on the desorption of any given species M [42].

Likewise, an adsorption rate coefficient (k_{ads}) can be defined by

$$r_{ads} = \frac{\mathrm{d}[\mathrm{M}]_{surf}}{\mathrm{d}t} = k_{ads}[\mathrm{M}]_{gas}\,, \tag{6.2}$$

where r_{ads} is the reaction rate of adsorption. Pitts and co-workers have incorporated the dependence of the adsorption rate on coverage and site density into k_{ads} as these factors cannot be separated from the adsorption rate coefficient without making assumptions about the properties of the system [42].

In the work of Pitt and co-workers [42], adsorption is considered to correspond to equilibration with the surface. In this context, the sticking (S_c) coefficient (or the sticking probability) is given as the ratio between the rate of adsorption onto the surface and the rate of collisions (r_{coll}) with the surface. By using results from kinetic gas theory,

$$r_{coll} = \sqrt{\frac{k_B T}{2\pi m}}[\mathrm{M}]_{gas} A, \tag{6.3}$$

where k_B is the Boltzmann constant, T is the temperature, and m is the mass of the molecule M. Thus, we can therefore write the sticking coefficient as

$$S_c = k_{ads} \big/ \langle |v| \rangle\,, \tag{6.4}$$

where

$$\langle |v| \rangle = \sqrt{k_B T / 2\pi m} \tag{6.5}$$

is the average velocity of M in the gas phase in a direction normal to the surface [42].

We can derive an expression for the desorption rate coefficient by viewing the adsorption-desorption process from a thermodynamic perspective. Let us go back to our adsorbent surface with surface area A_s. The number of molecules hitting the surface per unit time equals the number of molecules contained in a cylinder with base area A and height determined by $\langle |v| \rangle$. If we assume that the ideal gas law is valid where P is the pressure and V is the volume of the gas, the number of molecules (N) in the cylinder is

$$\frac{N}{V}\langle |v| \rangle A = PA \big/ \sqrt{2\pi m k_B T}\,. \tag{6.6}$$

Thus, the flux (F) of molecules impinging on the surface per unit area and time is

$$F = P \big/ \sqrt{2\pi m k_B T}\,. \tag{6.7}$$

We can then rewrite the adsorption rate as

$$r_{\text{ads}} = S_{\text{c}}(\theta_{\text{ads}},T)F/n_{\text{ads}} = S_{\text{c}}(\theta_{\text{ads}},T)\frac{P}{n_{\text{ads}}\sqrt{2\pi m k_{\text{B}}T}}\,, \tag{6.8}$$

where we have said that the sticking coefficient is a function of the surface coverage (θ_{ads}) and the temperature (T), and n_{ads} is the number of adsorbate sites per unit area.

At equilibrium, the rate of adsorption and the rate of desorption must be equal and the pressure is given by the equilibrium pressure (P_{eq}). We can therefore write

$$r_{\text{ads,eq}} = r_{\text{des,eq}} \quad \Rightarrow \quad S_{\text{c}}(\theta_{\text{ads}},T)\frac{P_{\text{eq}}}{n_{\text{ads}}\sqrt{2\pi m k_{\text{B}}T}} = k_{\text{des}}(\theta_{\text{ads}},T)\theta_{\text{ads}}\,. \tag{6.9}$$

We know from statistical thermodynamics that the chemical potential of a gas (μ_{g}), taken as an ensemble of indistinguishable and independent particles, is given by [43]

$$\mu_{\text{g}} = \left(\frac{\partial G}{\partial N}\right)_{V,T} = E_{\text{g}} + k_{\text{B}}T\ln\left\{\frac{P}{k_{\text{B}}T}\left(\frac{h^2}{2\pi m k_{\text{B}}T}\right)^{3/2}\frac{1}{q_{\text{rot}}q_{\text{vib}}}\right\}, \tag{6.10}$$

where G is Gibbs energy, E_{g} is the ground-state energy of the gas, h is the Planck constant, and q_{rot} and q_{vib} are the rotational and vibrational partition functions for the gas-phase molecules, respectively. We can express the equilibrium pressure in terms of the chemical potential of the gas phase by rearrangement of eq. (6.10). Further, the chemical potential of the gas phase is equal to the chemical potential of the adsorbed phase ($\mu_{\text{ads}}(\theta_{\text{ads}}, T)$) at equilibrium. We can then express the desorption rate coefficient as follows by insertion of eq. (6.10) into eq. (6.9):

$$k_{\text{des}}(\theta_{\text{ads}},T) = S_{\text{c}}(\theta_{\text{ads}},T)\frac{1}{n_{\text{ads}}}\frac{k_{\text{B}}T}{h}\frac{2\pi m k_{\text{B}}T}{h^2}q_{\text{rot}}q_{\text{vib}}\exp\left(\frac{\mu_{\text{ads}}-E_{\text{g}}}{k_{\text{B}}T}\right) \tag{6.11}$$

In the limit of zero coverage and no interaction between the adsorbates, the adsorbate chemical potential approaches the Langmuir lattice gas limit, and eq. (6.11) becomes [43]

$$k_{\text{des}}(\theta_{\text{ads}},T) = S_{\text{c}}(\theta_{\text{ads}},T)\frac{1}{(1-\theta_{\text{ads}})n_{\text{ads}}}\frac{k_{\text{B}}T}{h}\frac{2\pi m k_{\text{B}}T}{h^2}q_{\text{rot}}q_{\text{vib}}\exp\left(-\frac{(E_{\text{g}}-E_{\text{ads}})}{k_{\text{B}}T}\right), \tag{6.12}$$

where E_{ads} is the energy for each adsorption site. Equation (6.12) is often conveniently rewritten as

$$k_{\text{des}}(\theta_{\text{ads}},T) = S_{\text{c}}(\theta_{\text{ads}},T)\frac{k_{\text{B}}T}{h}\frac{Q_{\text{2D-gas}}}{Q_{\text{ads}}}\exp(-E_0/k_{\text{B}}T)\,, \tag{6.13}$$

where $Q_{\text{2D-gas}}$ is the partition function for a gas translating in only two dimensions, Q_{ads} is the coverage- and temperature-dependent partition function for the adsorbed state, and $E_0 = E_{\text{g}} - E_{\text{ads}}$.

6.2 Transition-state theory

We now go on to describe how the desorption rate coefficient and the sticking coefficient can be obtained from transition-state theory (TST) [44-46]. Transition-state theory relies on two fundamental assumptions: rapid energy randomization in the reactant configuration ("ergodicity") and the existence of a critical (dividing) hypersurface in phase space where every trajectory passing through this surface started in the reactant valley of the potential energy hypersurface[6] (PES), and these trajectories do not recross the dividing hypersurface [48]. The latter assumption is known as the transition-state assumption. Assumption of ergodicity means that the system has no memory of how it was prepared and all parts of phase space are accessible on the timescale of the reaction, subjected only to the constraints of conservation of energy and total angular momentum.

Before we apply transition-state theory to desorption phenomena, let us discuss TST in relation to a gas-phase reaction to get an understanding of the underlying physics of the theory. We start out by assuming that our chemical reaction occurring in the gas phase can be described by classical mechanics and that the reacting systems are independent of each other. We further assume that the chemical reaction takes place on its ground-state electronic PES, i.e., no electronic transitions are allowed [48].

Consider then an ensemble of systems each containing n classical particles interacting with a known potential. The state of each system can be represented by a point in a $6n$-dimensional phase space ($\mathbf{p}$, $\mathbf{q}$), where $\mathbf{q}$ is a set of generalized coordinates and $\mathbf{p}$ its conjugated linear momentum. Let $\rho(\mathbf{p}, \mathbf{q})$ be the density of such points. Since the number of points is conserved, ρ satisfies the continuity equation

$$\frac{\partial \rho}{\partial t} + \nabla \cdot \rho \mathbf{v} = 0 \,, \tag{6.14}$$

where $\mathbf{v}$ is the generalized velocity of a point in phase space and ∇ is the generalized divergence operator. The flow through phase space is governed by the Hamilton equation

$$\dot{q}_j = \partial H / \partial p_j \,, \quad \dot{p}_j = -\partial H / \partial q_j \,, \tag{6.15}$$

where $H(\mathbf{p}, \mathbf{q})$ is the Hamiltonian of the system, and $\dot{q}_j$ and $\dot{p}_j$ are the components of $\mathbf{v}$. Thus, a chemical reaction can be described as the convection of representative points from one region of phase space to another.

We now consider a volume $\Omega(i)$ in phase space corresponding to a particular chemical state i. Integration of eq. (6.14) gives [48]

[6] Hypersurface is a generalization of the concept of an ordinary surface in the three-dimensional space to the case of an n-dimensional space. The dimension of a hypersurface is one less than that of its ambient space [47].

$$\frac{\partial N(i)}{\partial t} = -\int_{\Omega(i)} (\nabla \cdot \rho \mathbf{v}) \mathrm{d}^{6n}\tau = -\int_{\Omega(i)} (\nabla \cdot \rho \mathbf{v}) \prod_{j=1}^{3n} \mathrm{d}p_j \mathrm{d}q_j \,, \tag{6.16}$$

Where

$$N(i) = \int_{\Omega(i)} \rho \prod_{j=1}^{3n} \mathrm{d}p_j \mathrm{d}q_j \,. \tag{6.17}$$

Invoking the Divergence Theorem gives

$$\frac{\partial N(i)}{\partial t} = -\int_{S(i)} \rho(\mathbf{v} \cdot \mathbf{n}) \mathrm{d}\sigma \,, \tag{6.18}$$

where **n** is the unit outward normal to $\mathrm{d}\sigma$ and $S(i)$ is the surface bounding the volume $\Omega(i)$. We can write the population and depopulation of state *i* by reactions leading to and from various final states *f* as [48]

$$\frac{\partial N(i)}{\partial t} = \sum_f R(i, f) - R(f, i) \,, \tag{6.19}$$

where

$$R(f, i) = \int_{S(f,i)} \rho(\mathbf{v} \cdot \mathbf{n}) \mathrm{d}\sigma \,, \tag{6.20}$$

and $S(f, i)$ is the partial surface corresponding to reactions leading from *i* to *f* (this is the diving hypersurface mentioned above), bounded by the constraints

$$S(\mathbf{p}, \mathbf{q}) = 0, \quad (\mathbf{v} \cdot \mathbf{n}) > 0 \,. \tag{6.21}$$

Let $\mathbf{n} = (\nabla S / |\nabla S|)_{S=0}$, which gives

$$R(f, i) = \int_{S(f,i)} \rho(\mathbf{v} \cdot \nabla S) \frac{\mathrm{d}\sigma}{|\nabla S|} \,. \tag{6.22}$$

Expansion of $(\mathbf{v} \cdot \nabla S)$ and setting $S(\mathbf{p}, \mathbf{q}) = S(\mathbf{q})$, gives

$$R(f, i) = \int_{S(f,i)} \rho \left(\sum_{j=1}^{3n} \frac{J_j}{|J_1|} \right) \mathrm{d}H \prod_{j=2}^{3n} \mathrm{d}p_j \mathrm{d}q_j \,, \tag{6.23}$$

where J_j is the Jacobian of the transformation from (H, S) to (p_j, q_j).

If the chemical reaction is the result of the interaction of $\nu \leq n$ particles, it can be shown that the rate coefficient is given by [48]

$$k(f,i) = R(f,i)V^{\nu-1}/N(i)\,, \tag{6.24}$$

where V is the normalization volume. We now assume that the internal degrees of freedom of the reactants are in local equilibrium and described by the Boltzmann distribution:

$$\rho = \rho_0 \exp(-H/k_{\mathrm{B}}T)\,. \tag{6.25}$$

Combining eqs. (6.25), (6.24), (6.23), and (6.17), and integrating over the center-of-mass coordinates, we obtain the following expression for the rate coefficient:

$$k(f,i) = \frac{1}{Q(i)} \int_{S(f,i)} \exp(-E/k_{\mathrm{B}}T) \left(\sum_{j=1}^{3n-3} \frac{J_j}{|J_1|} \right) \mathrm{d}E \prod_{j=2}^{3n-3} \mathrm{d}p_j \mathrm{d}q_j\,, \tag{6.26}$$

where

$$Q(i) = V^{1-\nu} \int_{\Omega(i)} \exp(-E/k_{\mathrm{B}}T) \prod_{j=1}^{3n-3} \mathrm{d}p_j \mathrm{d}q_j \tag{6.27}$$

is the classical partition function per unit volume for a system in its initial state, and

$$E = H - p^2/2m \tag{6.28}$$

is the total energy in the center-of-mass coordinate system (p is the linear momentum of the system) [48].

Let us now assume that the reactants and products in our chemical reaction are separated by a barrier with energy E_0 (see Figure 6.1). If we take the reaction coordinate as the minimum energy path and introduce a trial dividing hypersurface located at the saddle point (the transition state) and orthogonal to the reaction coordinate, it can be shown that eq. (6.26) takes the familiar form associated with conventional transition state theory (see Keck [48] for details):

$$k(T) = \frac{k_{\mathrm{B}}T}{h} \frac{Q^{\dagger}(T)}{Q(T)} \exp(-E_0/k_{\mathrm{B}}T)\,, \tag{6.29}$$

Here, $Q^{\dagger}$ and Q are the partition functions of the transition state and reactants, respectively, and h is the Planck constant. It can be shown that the factors $Q^{\dagger}(T)/Q(T)$ and $\exp(-E_0/k_{\mathrm{B}}T)$ are associated with the entropic and enthalpic contributions to the reaction rate coefficient, respectively.

However, for reactions with a barrier the optimum dividing hypersurface (representing the dynamical bottleneck of the system) is not necessarily located at the saddle point of the electronic potential energy hypersurface. For reactions without a barrier, the location of the optimum dividing surface will vary with the energy and total angular momentum of the system. One can still

calculate the rate coefficient for the reaction by variational minimization the reactive flux for a set of trial dividing hypersurfaces.

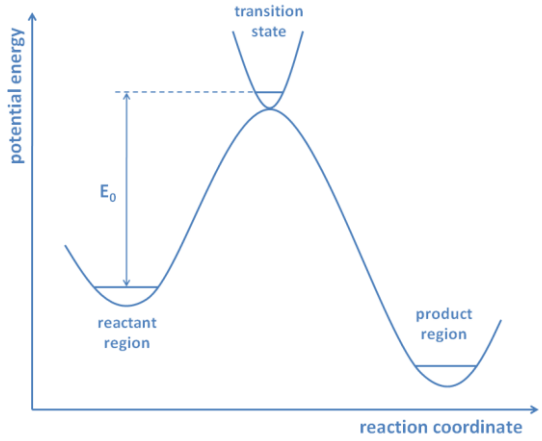

Figure 6.1 Schematic illustration of the minimum energy path of a chemical reaction with a barrier.

To illustrate the concept of variational minimization of the reactive flux, consider the potential energy surface depicted in Figure 6.2. The red solid line represents a reacting trajectory going from the reactants (R) to products (P), while the blue dotted line represents a nonreacting trajectory originating and ending in the reactants' region. If the dividing hypersurface is placed at the saddle point (illustrated by the black dashed line), the nonreacting trajectory is also included in the calculation of the reactive flux. Consequently, the reaction rate coefficient will be overestimated. If, on the other hand, the dividing surface is placed as illustrated by the black solid line in Figure 6.2, only reacting trajectories are counted, thus fulfilling the transition-state assumption. For a canonical ensemble[7], the minimization of the reactive flux can be written as [49]

$$k^{\mathrm{CVT}}(T) = \min_{\xi} k^{\mathrm{GT}}(T,\xi)\,, \tag{6.30}$$

where $k^{\mathrm{CVT}}(T)$ is the rate coefficient obtained from canonical variational transition-state theory (CVT) at temperature T, $k^{\mathrm{GT}}(T,\ \xi)$ is the generalized TST rate coefficient for a given reaction coordinate ξ, which is orthogonal to the dividing surface S:

$$k^{\mathrm{GT}}(T,\xi) = \frac{k_{\mathrm{B}}T}{h}\frac{Q^{\dagger}(T,\xi)}{Q(T)}\exp(-V_{\mathrm{MEP}}(\xi)/k_{\mathrm{B}}T)\,. \tag{6.31}$$

$V_{\mathrm{MEP}}(\xi)$ is the electronic potential energy at point ξ on the minimum energy path (MEP) relative to the overall zero of energy [49].

As presented, TST gives an exact upper bound to the classical reaction rate coefficient. Quantum effects can be included by replacing the classical partition functions with quantum partition func-

[7] For more details on a canonical ensemble see a textbook in thermodynamics.

tions, and by introducing ad hoc a transmission coefficient (κ) that corrects for quantum effects in the unbound degrees of freedom (usually tunneling along the reaction coordinate).

$$k(T) = \kappa(T) k^{\mathrm{TST}}(T) \tag{6.32}$$

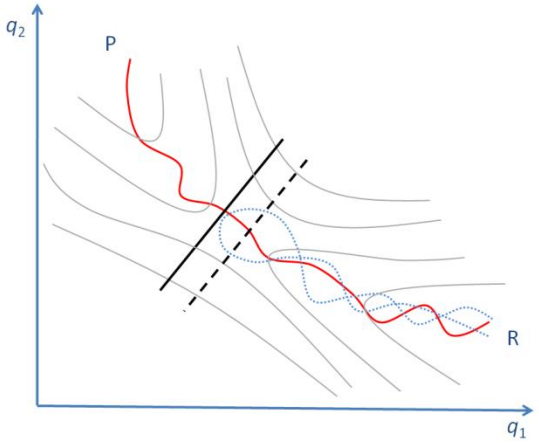

Figure 6.2 Schematic illustration of a reacting (red solid line) and a nonreacting (blue dotted line) trajectory, where (q_1, q_2) are coordinates and R and P denote reactants and products, respectively. The black dashed line represents a trial dividing hypersurface located at the saddle point and the black solid line represents the optimum dividing surface.

We have now developed the necessary machinery for discussing the application of transition-state theory for characterizing and predicting desorption rate coefficients. As for gas-phase reactions, one relies on the validity of ergodicity and the transition-state assumption when applying TST to gas-surface reactions. Grimmelmann et al. have shown that it is possible to correct for the errors induced by these assumptions by multiplying the TST desorption rate coefficient with the exact sticking coefficient to obtain the exact desorption rate coefficient *if the dividing surface is chosen at infinite adsorbent-adsorbate separation*:

$$k_{\mathrm{des}} = S_{\mathrm{c}} k_{\mathrm{des}}^{\mathrm{TST}} \tag{6.33}$$

Here, the factor S_{c} accounts for all trajectories neglected by the transition-state assumption, because the fraction of trajectories that recross the dividing surface at infinite adsorbent-adsorbate separation is precisely the sticking coefficient. If the dividing surface is chosen at infinite adsorbent-adsorbate separation, it can be shown that the sticking coefficient is precisely one [42]. However, eq. (6.33) does not imply that S_{c} must be one in all cases as will be demonstrated in the following.

6.3 Variational behavior of the sticking coefficient

Most often, eq. (6.33) is used to interpret experimental results. It would be desirable to be able to predict $S_{\mathrm{c}}(\theta_{\mathrm{ads}}, T)$ and $k_{\mathrm{des}}(\theta_{\mathrm{ads}}, T)$ independently using transition-state theory and in this way,

elucidate the physical factors contributing to the desorption rate coefficient. In the following we will present results from variational calculations of the sticking coefficient for a model surface.

Consider a clean (100) model surface taken as a square lattice of adsorption sites with surface area $A = M^2 = n_{ads}L^2$. The surface is assumed to lie in the (x, y) plane, and motion in (x, y) is assumed to be separable from motion in z. The potential function for motion in the (x, y) plane is given by

$$\begin{aligned} V(x) &= V_0 \qquad (n-1)L \le x \le nL \\ V(x) &= 0 \qquad nL \le x \le (n+1)L \\ V(y) &= V_0 \qquad (n-1)L \le y \le nL \\ V(y) &= 0 \qquad nL \le x \le (n+1)L \end{aligned} \tag{6.34}$$

where n is an odd positive integer, (x, y) is bounded by the area M^2, and V_0 is the barrier to migration on the surface modeled by

$$V_0(z) = V_0 \exp(-\alpha z^2). \tag{6.35}$$

That is, the barrier to migration decays with increasing separation of the adsorbate from the surface. The potential function $V(x, y)$ is illustrated in Figure 6.3. The potential function for the adsorption/desorption process is modeled by the following Morse potential

$$V(z) = \Delta_{des}H^\circ \, 1 - \exp(-\beta z)^{\,2}, \tag{6.36}$$

where $\Delta_{des}H^\circ$ is the enthalpy of desorption at standard conditions.

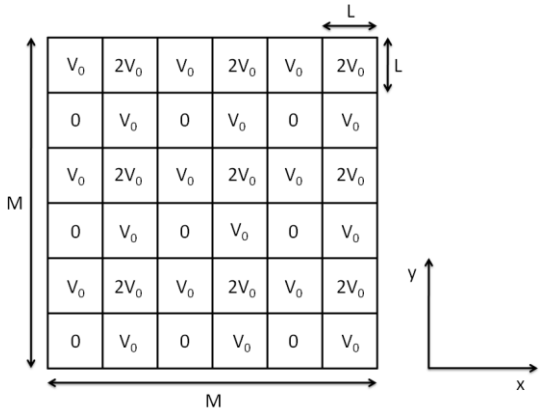

Figure 6.3 Simple potential function for a (100) model surface (after Pitt et al. [42]).

Pitt et al. [42] have shown that if $\Delta_{des}H^\circ \ge V(z) + 2V_0(z)$ for all z, then $S_c = 1$ is the variational minimum sticking coefficient. However, if $\Delta_{des}H^\circ < V(z) + 2V_0(z)$, it can be shown that the sticking coefficient for this model surface is given by

$$S_c = \frac{1}{4}\left\{ e^{(\Delta_{des}H^\circ - V(z) - 2V_0(z))/k_B T} + 2e^{(\Delta_{des}H^\circ - V(z) - V_0(z))/k_B T} + \frac{\Delta_{des}H^\circ - V(z)}{k_B T} + 1 \right\}. \tag{6.37}$$

Caveat: There is an error in the expression for S_c given by eq. 38 in the paper of Pitt et al. [42].

A plot of the variational behavior of S_c for different temperatures is shown in Figure 6.4a. We see that for small $z^\dagger$, $S_c(z^\dagger) \rightarrow \infty$, which is unphysical. This effect is due to overcounting of trajectories by transition-state theory. When $z^\dagger \rightarrow \infty$, $S_c = 1$ as is necessarily true for this dividing surface. Further, we see that the location of the dividing hypersurface ($z^\dagger$) is closer to the adsorbent surface as the temperature is increased, which is reasonable.

In Figure 6.4b the temperature dependence of the variational minimum $S_c(z^\dagger)$ is shown. We see that the value of $S_c(z^\dagger)$ goes through a minimum ($S_c \approx 1/4$) and increases towards unity as $T \rightarrow 0$. As discussed by Pitt et al. [42], the increase of $S_c(z^\dagger)$ with temperature above 0.1 K can be understood by considering the entropy change during adsorption. For the model surface under study, the motion of the adsorbed species was described by free translation in the (x, y) plane and as harmonic oscillation in the z direction. Thus, the entropy change to reach the transition state for adsorption is greatest at low temperatures and smallest at high temperatures. It is therefore a possibility that large entropy changes on reaching the transition state might outweigh the favorable adsorption enthalpy change as $T \rightarrow 0.1$ K. The appearance of $S_c(z^\dagger) < 1$ can therefore be ascribed to reduced sticking due to the entropic restrictions imposed on an adsorbed molecule [42]. Below 0.1 K the enthalpic contribution dominates and $S_c(z^\dagger)$ approaches unity.

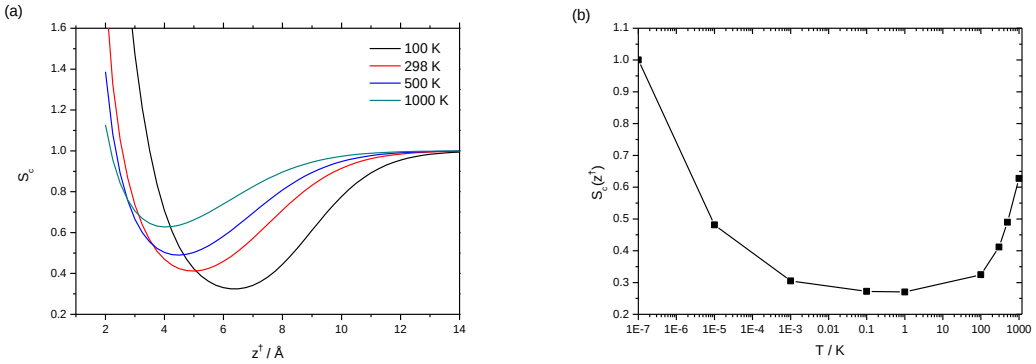

Figure 6.4 (a) Variational behavior of the sticking coefficient (S_c) and (b) temperature dependence of the variational minimum $S_c(z^\dagger)$ for barrierless adsorption onto a clean (100) model surface given by eq. (6.37), where $\Delta_{des}H^\circ = 41.84$ kJ mol^{-1}, $V_0 = 12.55$ kJ mol^{-1}, $\alpha = 0.04$ Å^{-2}, and $\beta = 1.0$ Å^{-1}.

Pitt and co-workers argues that the effects leading to $S_c < 1$, are probably of less importance for clean metal surfaces, but may be more important for partially covered surfaces and surfaces with many defects [42]. We will not present a TST description of such surfaces, but rather refer the interested reader to the later papers by Pitt and co-workers [24;50].

Finally, we mention that there are other entropic factors that could produce a variational minimum sticking coefficient of less than one. Polyatomic molecules may have low vibrational fre-

quencies that are strongly affected by adsorption, and therefore give an entropy change sufficiently large to yield $S_c < 1$ [42].

7 Experimental and computational methods

In the following a short description of some useful experimental and computational methods for surface science studies is given. The selected experimental techniques are temperature-programmed desorption (TPD), Fourier-transform infrared spectroscopy (FT-IR), Raman spectroscopy, electron microscopy, scanning electron microscopy (SEM), and nuclear magnetic resonance spectroscopy (NMR).

7.1 Temperature-programmed desorption

An experimental setup for temperature-programmed desorption (TPD) is illustrated in Figure 7.1. The sample is mounted in an ultra-high vacuum chamber and can be heated by means of heating wires. The concentration of desorbing species as a function of the temperature is usually measured with a quadrupole mass spectrometer. It is important that the pumping capacity is sufficiently high to prevent readsorption of the desorbed species. If the pumping speed is infinitely high, readsorption can be ignored and the relative rate of desorption is given by [51]

$$r_{des} = -\frac{\mathrm{d}\theta_{\mathrm{ads}}}{\mathrm{d}t} = k_{\mathrm{des}}\theta_{\mathrm{ads}}^{n} = A_{\mathrm{des}}(\theta_{\mathrm{ads}})\exp\left[-E_{\mathrm{des}}(\theta_{\mathrm{ads}})/k_{\mathrm{B}}T\right]\theta_{\mathrm{ads}}^{n}, \tag{7.1}$$

where

$$T = T_0 + \beta t, \tag{7.2}$$

and θ_{ads} is the coverage, n is the order of desorption, A_{des} is the pre-exponential factor of desorption, E_{des} is the activation energy of desorption, T_0 is the temperature at the start of the experiment, $\beta = \mathrm{d}T/\mathrm{d}t$ is the heating rate, and k_{B} is the Boltzmann constant.

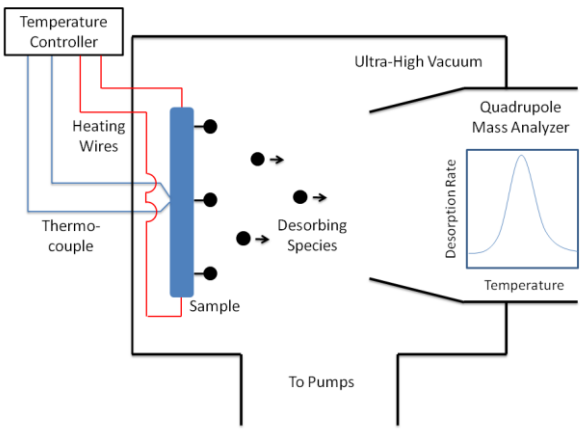

Figure 7.1 Illustration of an experimental setup for temperature-programmed desorption studies in ultra-high vacuum. Desorption of gases is followed using mass spectrometry (after Niemantsverdriet [51]).

TPD is a very useful technique in surface science, especially for single crystals and polycrystalline materials. The method can provide quantitative information about the coverage of adsorbates, the activation energy of desorption (usually equal to the activation energy of adsorption), lateral interactions between the adsorbates through the coverage-dependent adsorption energy, and the desorption mechanism through the pre-exponential factor of desorption (when interpreted by means of transition-state theory) [51].

Because the activation energy of desorption and the pre-exponential factor of desorption are coverage-dependent, the complete analysis of TPD spectra is complicated and time-consuming. Most surface scientists therefore rely on simplified methods which make use of easily accessible spectral features like the temperature of the peak maximum (T_{max}) and the full width at half-maximum intensity (W_{HM}) [51].

According to Niemantsverdriet [51], the semi-empirical Redhead formula is particularly popular where the activation energy of desorption is given by

$$E_{des} = k_B T_{max} \left[\ln\left(\frac{A_{des} T_{max}}{\beta} \right) - 3.46 \right], \tag{7.3}$$

where, again, β is the heating rate. The Redhead formula is approximately correct for first-order desorption (eq. 6.1) and for values of A_{des}/β in the order of 10^8–10^{13} K^{-1}. However, it is necessary to guess a value for A_{des}. A more interesting method is the Chan–Aris–Weinberg method where the activation energy of desorption and the pre-exponential factor of desorption are given by [51]

$$E_{des} = k_B T_{max} \left[\sqrt{\left(\frac{W_{HM}}{T_{max}} \right)^2 + 5.832 \frac{T_{max}}{W_{HM}}} - 1 \right] \tag{7.4}$$

$$A_{des} = \frac{E_{des} \beta}{k_B T_{max}^2} \exp(E_{des}/k_B T_{max}) \tag{7.5}$$

for first-order desorption. However, the Chan–Aris–Weinberg equations only predict correct values for E_{des} and A_{des} at zero coverage [51]. For porous materials the TPD analysis is much more complex because of intraparticle diffusion and intrinsic adsorption/desorption [52].

7.2 Microscopy

This section will give a short introduction to electron microscopy and some more details around scanning electron microscopy (SEM). The section is based on ref. [51].

7.2.1 Electron microscopy

Optical microscopy uses visible light. Since the wavelength of such light is rather long (~ 200 nm), no features below 1 μm can be detected. In order to obtain a better resolution an electron beam with much less wavelength (< 1 Å) can be used. Details with a resolution of about 0.1 nm

can then be detected. Electron microscopy is hence a common method used in catalyst and surface research. Figure 7.2 shows a sketch of an electron microscope. An electron beam is sent towards a surface and splits in different directions, as summarized in the list below:

- Transmitted electrons: electrons that go through the sample without energy loss.
- Diffracted electrons: electrons that are diffracted by particles which are favourably oriented towards the beam. These electrons make it possible to obtain dark-field images and crystallographic information.
- Backscattered electrons: electrons which have collided with atoms in the sample and are scattered back. The higher the mass/size of the atoms in the sample, the more is backscattered.
- Auger electrons and X-rays: electrons formed in the relaxation of core-ionized atoms.
- Secondary electrons: electrons that have lost some of their energy due to inelastic collisions, mostly in the surface region.

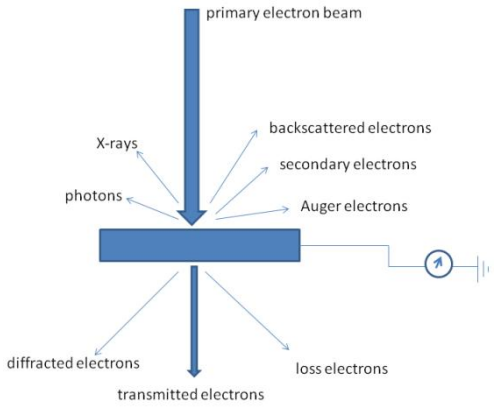

Figure 7.2 The interaction between the primary electron beam and the sample in an electron microscope leads to a number of detectable signal (reproduced after ref. [51]).

In addition the electrons cause characteristic vibrations in the sample. These vibrations can be investigated by studying the energy loss of the primary electrons.

7.2.1.1 Scanning electron microscopy

Scanning electron microscopy (SEM) can be used to study the topology and composition of a surface. SEM instruments have resolution of about 3–10 nm. A sketch of the set-up in SEM is shown in Figure 7.3. A narrow electron beam is sent over the surface. The yield of the either backscattered or secondary electrons are then detected as a function of the primary beam (see ref. [51] and references therein). This is used for bitmapping a picture of the sample. The different orientations at the surface cause contrast. The parts of the surface with surface normal pointing direct towards the detector will appear lighter than surface areas with normals pointing in other directions. The secondary electrons come from the surface region of the sample and inhabit mostly low energies (5–50 eV). Backscattered electrons originate from deeper in the sample and give

information about the chemical composition of the sample. Heavy elements will scatter more efficient and hence appear lighter.

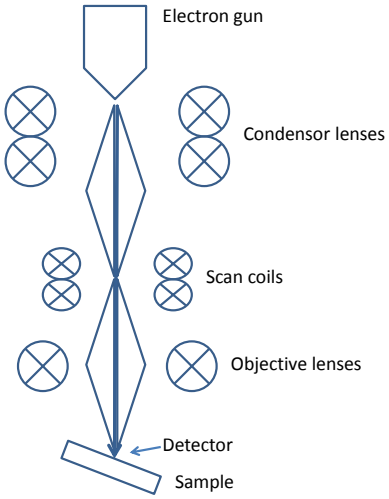

Figure 7.3 Schematic set-up of a scanning electron microscope (reproduced after ref. [51]).

7.3 Vibrational Spectroscopy

Fourier-transform infrared spectroscopy (FT-IR) and Raman spectroscopy are very useful non-destructive techniques for probing sorbate-sorbent interactions in situ with no or little sample preparation. Some of the most relevant FT-IR techniques for studying surfaces are illustrated in Figure 7.4.

Transmission infrared spectroscopy is the most common form of FT-IR spectroscopy. For surface science studies, however, it is only useful if the bulk of the material absorbs weakly. For the materials of interest in this work, this is seldom the case. Transmission FT-IR spectroscopy will therefore not be discussed further.

Diffuse reflectance infrared Fourier transform spectroscopy (DRIFTS) is a useful technique for studies of powders and rough surfaces. When an infrared beam is focused on the sample surface, the incident light is partly absorbed and partly scattered. For powders and rough surfaces there are three types of reflections: specular, diffuse, and so-called specular diffuse reflection. The two specular components are reflected from the surface without being absorbed by the sample, while the diffuse reflectance component has been absorbed by the sample before it is reflected from the surface at any angle. The diffusely scattered radiation is collected by an ellipsoidal mirror and focused on the detector. Different DRIFTS cells allow the sample to be investigated in situ in different atmospheres at different temperatures and pressures, which is of great interest in catalysis. Reproducible sample preparation for quantitative analysis is, however, difficult [53].

Reflection absorption infrared spectroscopy (RAIRS) measures the specular reflectance from a smooth surface. RAIRS is typically used for studies of adsorbed molecules on metal single crystals or polycrystalline foils. The infrared light enters the sample at the grazing angle. During reflection, the component of the light perpendicular to the surface excites those vibrations of the adsorbed molecule which give rise to an oscillating dipole moment perpendicular to the surface. The advantages of RAIRS are that there is no bulk signal and that the signal surface species is distinguishable from gas-phase species. However, it is difficult to observe low-frequency modes like the adsorbate-adsorbent bond.

Attenuated total reflectance (ATR) is a technique where the beam of infrared light traverses through an ATR crystal in intimate contact with the sample. The crystal is designed to enable internal reflection, thus creating an evanescent wave at the crystal surface which extends into the sample. In this way, absorption spectra can be recorded. The penetration depth of the evanescent wave is a function of the angle of incident of the infrared beam, the refractive index of the ATR crystal, and the wavelength of the light. Given the depth of penetration is typically a few micrometers, the adsorbent must be very thin so that the evanescent wave can probe the adsorbed species.

Raman spectroscopy and FT-IR spectroscopy are complementary techniques because different vibrational selection rules apply. Raman spectroscopy is highly suitable for in situ studies because the spectra of adsorbed species interfere weakly with signals from the gas-phase species [51]. Low-frequency vibrational modes that are difficult to investigate with FT-IR spectroscopy are often easy to study with Raman spectroscopy. Fluorescence from the sample can give rise to very large background signals, overshadowing the Raman signals. The problem with fluorescence can be reduced or eliminated by applying a different laser wavelength to excite the sample.

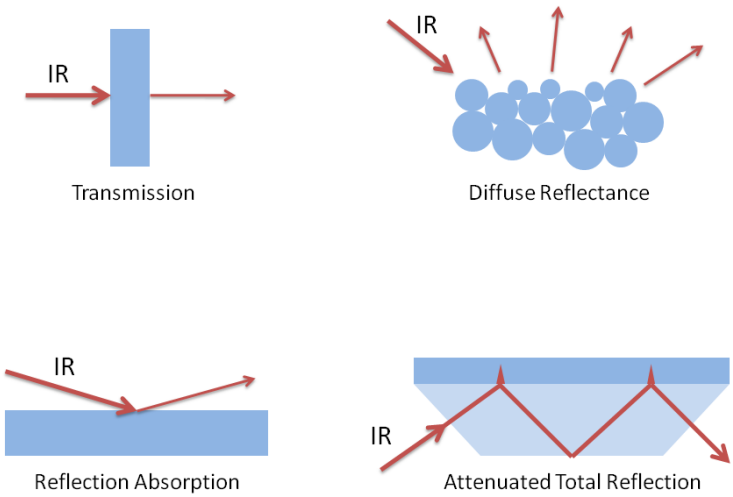

Figure 7.4 Some different techniques to perform Fourier-transform infrared spectroscopy.

7.4 Nuclear magnetic resonance spectroscopy

This section, which is based on refs. [54-57], provides a short introduction to the Nuclear Magnetic Resonance technique (NMR). A typical instrument setup is shown in Figure 7.5.

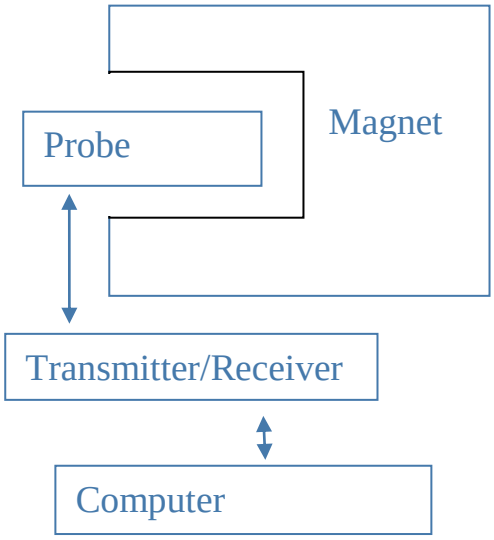

Figure 7.5 A simplified sketch of a nuclear magnetic resonance (NMR) system. The probe contains the sample for investigation [56].

NMR is a technique based on the quantum mechanical nuclear spin, I, of each atom. The nuclear spin has values $\pm n/2$, where n is a number between 0 and infinity. The nuclear magnetic moment, μ, is proportional to the spin, and is defined a

$$\mu = \gamma I\hbar \text{ or } \boldsymbol{\mu} = \gamma \mathbf{L} \tag{7.6}$$

where γ is the gyromagnetic ratio (the ratio between the magnetic moment of the nucleus and its angular momentum), which varies for each particular nucleus, $\hbar$ is the Planck constant h divided by 2π. In the vector definition $\mathbf{L}$ is the angular momentum. If the numbers of protons or neutrons are odd (or both of them), the net value of the nuclear spin is larger than zero and the nucleus has a magnetic moment (see e.g. ref. [58]).

To achieve an NMR signal the sample is first exposed to a static magnetic field B_0 to orient all spins in the same direction as illustrated in Figure 7.6. The system is after application of B_0 in the new ground state energy of the system

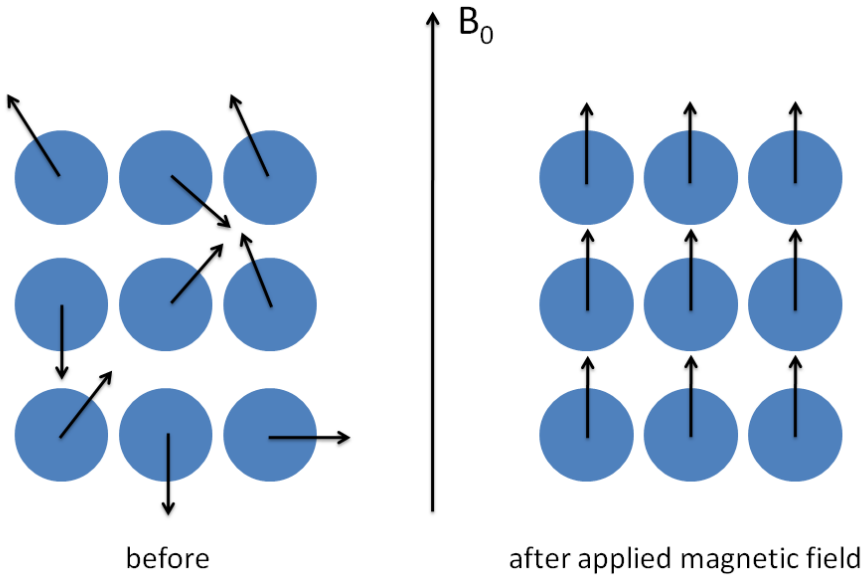

Figure 7.6 Nuclear spin orientations before and after an external magnetic field, B_0 is applied [57;59].

Due to the quantum mechanical Pauli principle only certain moments are allowed. For a single spin possible orientations are restricted to $-I$, $-I + 1$, $-I + 2$,…, $I - 2$, $I - 1$, I. This gives a total number of $(2I + 1)$ orientations, each denoted by the quantum number m_I. As an example consider a nucleus with spin 3/2, the possible values of m_I are then –3/2, –1/2, 1/2, 3/2.

The energy of the interaction is proportional to the nuclear moment and the applied field:

$$E = -\gamma \hbar m_I B_0 \tag{7.7}$$

The values of m_I can only be changed by one unit, i.e. $\Delta m_I = \pm 1$. The transition energy must hence be given as

$$\Delta E = \gamma \hbar B_0 = \hbar \omega \tag{7.8}$$

Thus, the resonance frequency is given by

$$\omega = \gamma B_0 \tag{7.9}$$

Since the nuclear momentum γ is specific for each type of nucleus, the resonance frequency must be specific for each type of nucleus also. This is the fundamental principle of NMR [54].

7.4.1.1 Sensivity of the NMR signal

For a nucleus with spin $I = 1/2$ there are two possible orientations, $m_I = \pm 1/2$, as shown in Figure 7.7.

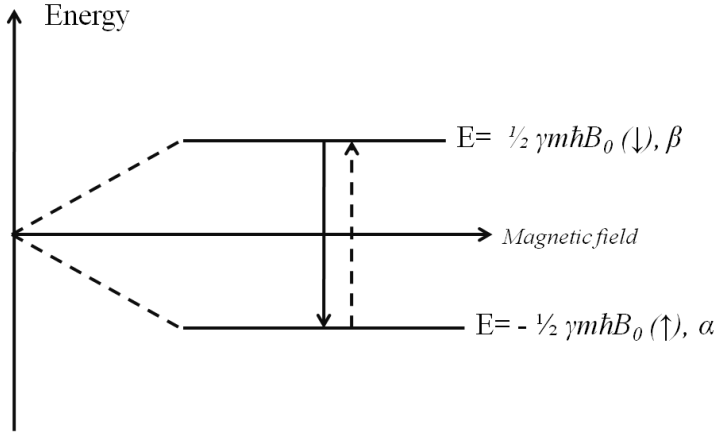

Figure 7.7 Energy levels and transitions for a nucleus (I =1/2) in a magnetic field B (reproduced after ref. [54]).

The parallel lower state (↑) $m_I = +1/2$ ($E = -\gamma m\hbar B_0$) is the lower in energy and hence the most stable, this state is called α. The antiparalell higher state (↓), $m_I = -1/2$ is called β. Two transitions equal in energy are allowed: $\alpha \rightarrow \beta$ and $\beta \rightarrow \alpha$, corresponding to absorption and emission of energy respectively. The number of spins in the two different states is different, giving a net absorption energy, and hence a NMR signal. The number of spins are N_α and N_β in the α and β state. The ratio between these is found from the Boltzmann distribution and can hence be written as

$$\frac{N_\beta}{N_\alpha} = e^{-\hbar\omega/k_B T} \tag{7.10}$$

as $\hbar\omega << k_B T$.

The frequencies of the NMR signal are in the order of 10^7 MeV, and the excess population in the lower state is hence ~ 10^5 .This gives a very low sensivity of the NMR signal, but a magnitude direct proportional to the number of nucleus producing it [54].

The sensivity also depends on the abundance of the nuclei that is being studied. The natural abundance of ^{1}H, ^{13}C, and ^{15}N is ~100%, 1%, and 0.4% respectively. The sensitivity of ^{13}C and ^{15}N are hence much lower than for ^{1}H [60;61].

7.4.1.2 Effective field

The effective field, $B_{0,}$ felt by the nucleus differs from the applied field because of the tiny local field, B_{loc}, from the circulating electron cloud around the nuclei. The effective field can hence be written as

$$B_0 = B_0 - B_{loc} \tag{7.11}$$

The form of the cloued and hence the shielding felt by the nuclei, is determined by the nature of the surrounding atoms. This gives different emitted energies for each unique nucleus [55].

7.4.1.3 Chemical shift

The resonance frequency of a nucleus is a consequence of its magnetic environment. The resonace is hence reported as a chemical shift, δ, defined as the percentual difference (in ppm), between the signal recorded for the sample, ω_{sample}, and a reference sample ω_{standard},

$$\delta = \frac{\omega_{\text{sample}} - \omega_{\text{standard}}}{\omega_{\text{spectrometer}}} \times 10^6 \tag{7.12}$$

where $\omega_{\text{spectrometer}}$ is the frequency of the instrument [10]. For ^{1}H and ^{13}C the reference is TMS, with $\delta = 0$ by definition.

7.4.1.4 Pulse sequences, dimensions, FID and Fourier transformation

To achieve energy resonances from nucleus moving to higher fields a pulsing external field *B* is applied. Different pulse sequences are chosen based on which nucleus to be studied and which information wished to obtain. It is for instance possible to study a sample by using 2D or multi-dimensional experiments. Such experiments are based on coupling through nuclear dipoles both scalar and through space and will give hence give information about geometrical structure. Figure 7.8 shows an example of a typical pulse sequence, RF, and the following Free Induction Decay, FID, signal. FID is the recorded signal after pulse application. This signal is time dependent. To get a frequency dependent signal, the FID is Fourier transformed as shown in Figure 7.9.

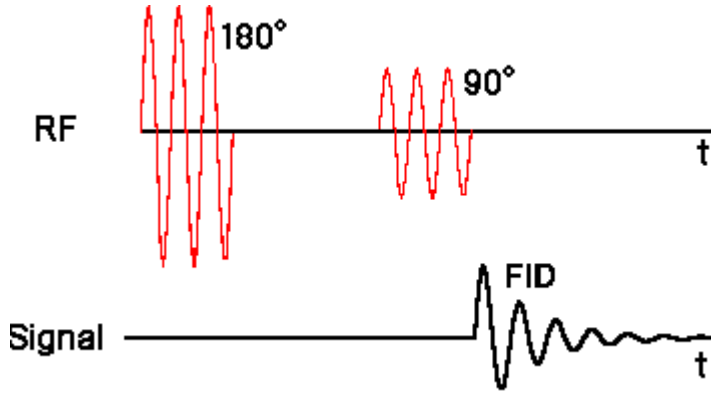

Figure 7.8 Pulse sequence applied on a sample. The FID is the corresponding out signal received by the computer [54;57].

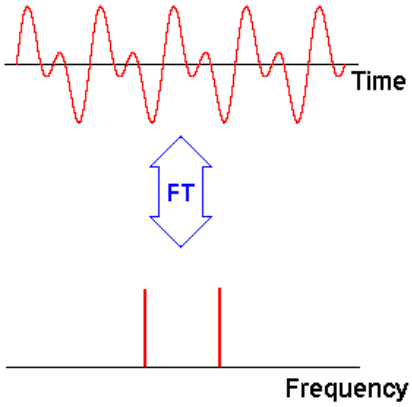

Figure 7.9 Fourier transformation from time domain to frequency domain [54;57].

7.4.2 MAS-NMR

This section will give a brief overview to the basic theory in solid state NMR. The section is written from details in [62]. In all materials various molecular orientations give rise to different fields. In liquid state these fields cancel out due to rapid molecular motion. In solid state the fields are fixed due to a rigid latter. Important interactions in a solid are dipolar coupling, magnetic shielding and quadrupolar coupling. Due to the strong interactions in a solid, the resonance spectrum signals from solids are much broader than those for solutions, see Figure 7.10.

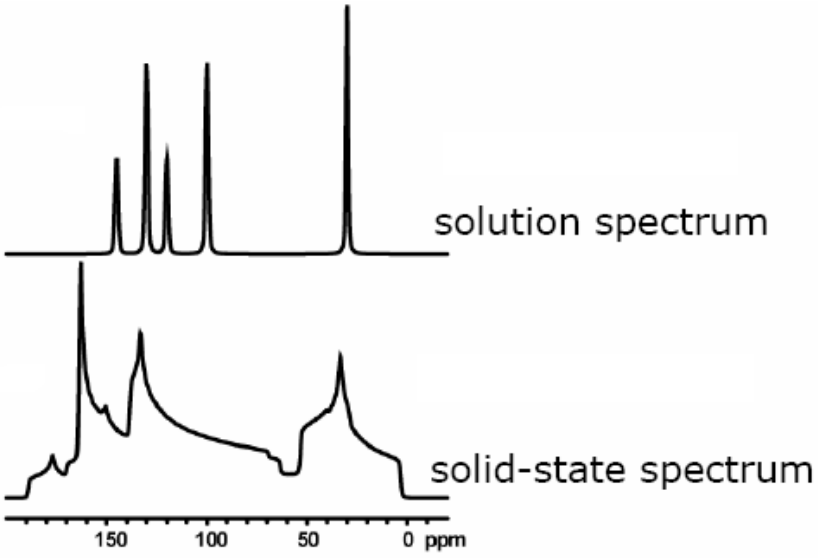

Figure 7.10 Simulated ^{13}C spectra for solution and solid-state [63].

The magnitude of a dipolar coupling and chemical shield interactions both depends on the term $3\cos^2\theta - 1$, where θ is the angle between two spins and the magnetic field B_0. When θ is 54.7°, the interactions disappears. This is the "magic angle". This means that if all molecules were oriented in this direction we could achieve a narrow spectrum to the fast tumbling limit. However it is not possible to orient all molecules in one direction, rather one tries to make the average orientation to 54.7°. To achieve this, the sample is placed inside a tube inside a rotor and oriented

at an angle 54.7° to the magnetic field B_0. The sample is then spun at an extremely high speed, 5-70 kHz. The setup is shown in Figure 7.11, hence the name "Magic Angle Spinning" (MAS).

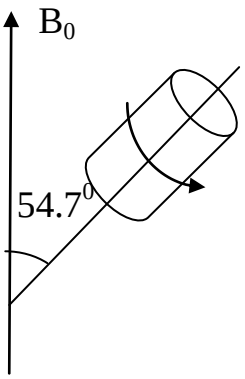

Figure 7.11 Solid sample inside rotor, oriented with an angle 54.7^0 to the external magnetic field B_0 [62].

In addition to spinning, the NMR signal can be increased by "transferring" magnetization from e.g. protons to carbon with the help of special pulse sequences. The NMR signal from the carbons theoretically then increases by a factor of four. This is Cross Polarization (CP) [62].

MAS-NMR can be used to study the sorption process on surfaces. By comparing experiments done at the same sample but performed at different times, splittings and new bonds can be seen. By measuring the time[8] it takes for a sample to return to its original state after application of a pulse, changes in bonds or surroundings can be studied. It is also possible to stepwise scan surfaces which are stepwise exposed to different chemicals or surroundings.

7.5 Quantum chemical calculations

The use of quantum chemical calculations in sorption studies is an important tool for predicting chemical and physical properties of an adsorbent/adsorbate system. In the following a brief description of the theory behind electronic structure calculations will be given. Further details can be found in textbooks on molecular electronic structure theory [64;65].

7.5.1 The Schrödinger equation

In order to describe the electronic structure of a molecular system, it is necessary to solve the time-independent Schrödinger equation (SE):

$$\hat{\mathcal{H}}\Psi = E\Psi \,, \tag{7.13}$$

where $\hat{\mathcal{H}}$ is the Hamiltonian – the energy operator of the system, Ψ is the wavefunction containing all information about the system, and E is the total energy of the system. Analytical solutions

[8] The times measured are called T_1 and T_2, for more details see e.g. [54].

of the SE exist, however, only for the simplest systems. For a general many-electron system it is therefore necessary to make use of approximations. Three important approximations are invoked: (i) neglect relativistic effects, (ii) limit the total wavefunction to one electronic potential energy surface – the *adiabatic* approximation, and (iii) separate the wavefunction into an electronic part and a nuclear part – the *Born–Oppenheimer* (BO) approximation. Within the BO approximation one assumes, since the mass of an electron is very much smaller than the mass of a nuclei, that the electrons are able to adjust instantaneously to any change in the positions of the nuclei. This allows for a decoupling of the electronic and nuclear motions, and the electronic wavefunction thereby depends parametrically on the positions of the nuclei. The many-body problem is then reduced to solving the electronic SE for a given set of nuclear coordinates. The BO and the adiabatic approximations are usually good for molecules in their electronic ground states, but both breaks down when two or more solutions to the electronic SE are close in energy, a classic example being lithium fluoride. It is reasonable to neglect relativistic effects for atoms with atomic number less than 36; however, spin is a relativistic effect and must be introduced ad hoc.

7.5.2 One-electron model

An electron i is characterized by the spatial coordinates $\mathbf{r}_i = (X_i, Y_i, Z_i)$ and the spin coordinate s_i expressed as $\mathbf{x}_i = (\mathbf{r}_i, s_i)$. A wavefunction of an electron is called a spin orbital and it is assumed that it can be written as a product of a spatial (molecular) orbital ϕ and a spin function θ:

$$\psi_i(\mathbf{x}_i) = \phi(\mathbf{r}_i)\theta(s_i)\,, \tag{7.14}$$

where the spin function is α_i ($m_s = +1/2$) or β_i ($m_s = -1/2$). Each molecular orbital (MO) is expanded in terms of M basis functions χ localized on the nuclei, conventionally called atomic orbitals (MO = LCAO; Linear Combination of Atomic Orbitals):

$$\phi_i = \sum_{\mu=1}^{M} c_{i\mu}\chi_\mu\,. \tag{7.15}$$

Within the one-electron model it is assumed that the electrons move independently of each other in molecular orbitals and that the total electronic wavefunction Φ for a N electron system (Φ denotes an approximate wavefunction, while Ψ denotes an exact wavefunction) can be written as an antisymmetric product of spin orbitals given as a Slater determinant (SD):

$$\Phi = \hat{\mathcal{A}}\ \psi_1(\mathbf{x}_1)\psi_2(\mathbf{x}_2)\cdots\psi_N(\mathbf{x}_N)\,, \quad \langle\psi_i|\psi_j\rangle = \delta_{ij}\,, \tag{7.16}$$

where $\hat{\mathcal{A}}$ is an antisymmetrizing operator.

7.5.3 The Hartree–Fock approximation

In the Hartree–Fock (HF) approximation the total electronic wavefunction is given as a single Slater determinant and the energy is found from the variational principle[9]. The effect of describing the wavefunction as one SD and only allowing single excitations from the SD is that all electrons are treated separately and they only interact with each other through a mean field. HF theory is therefore often called *mean field theory*. The HF wavefunction is found by solving the HF equation

$$\hat{\mathcal{F}}\phi_i = \varepsilon_i \phi_i \,, \tag{7.17}$$

where $\hat{\mathcal{F}}$ is the Fock operator and ε_i is the energy of the molecular orbital.

The Fock operator is an effective one-electron energy operator which describes the kinetic energy of an electron, the attraction to all nuclei, and the repulsion to all other electrons through the Coulomb and the Exchange operators. Note that the Fock operator is associated with the variation in the total energy, and not the energy itself. Since each orbital depends on all the other orbitals, the HF equations must be solved iteratively until the starting orbitals are the same as the eigenfunctions of the Fock operator; a *self-consistent field* (SCF).

7.5.4 Electron correlation methods

The HF method provides solutions to the Schödinger equation where the real electron–electron interaction is replaced by an average interaction – a mean field. For a sufficiently large basis set the HF wavefunction describes ~99% of the total energy, however, the remaining ~1% is often very important for describing chemical phenomena.

The electron correlation energy is defined as the difference between the exact nonrelativistic energy and the HF energy of the electronic system, both calculated in a complete one-electron basis [65]. Physically, this corresponds to the electrons being further apart than described by the HF wavefunction. Electron correlation can be divided into *dynamic* correlation and *static* or non-dynamic correlation. The dynamic correlation arises from the Coulomb repulsion between the electrons, while the static correlation is related to the degeneracy or near-degeneracy among configurations in which the single determinant method breaks down as the configurations interact strongly and cannot be treated isolate from each other. This typically happens in bond-breaking processes where bonding and antibonding configurations become degenerate.

Several methods have been designed for treating electron correlation. In the following a description of the most useful methods will be described briefly.

[9] The variational principle states that an approximate wavefunction has an energy which is above or equal to the exact energy [64]. The equality holds only if the wavefunction is exact.

7.5.4.1 Møller–Plesset perturbation theory

Since the correlation energy is small compared to the total energy of the system, being around 1%, it seems reasonable to correct the HF wavefunction by using perturbation theory. Perturbation methods which add a correction to the solutions from methods using the one-particle approximation are called many-body perturbation theory (MBPT). One of the most popular MBPT methods is Møller–Plesset perturbation theory (MPPT) [66]. In MPPT the unperturbed Hamiltonian is written as a sum of the Fock operators and the perturbation operator is a two-electron operator. Therefore, the perturbations are double-excitations from the HF determinant. Summing up the energy terms through a certain order *n* gives the Møller-Presset, MP*n* energy.

It can be shown that the sum of the zero-order and first-order energy terms is equal to the HF energy. Thus, the second-order correction to the energy is the first interesting property; this method is denoted as MP2. The MP2 method recovers 80–90% of the correlation energy and is the most economical ab initio method for including electron correlation.

However, a problem with the MP*n* wavefunction is that it is not variational. There is therefore no guarantee that MP*n* results converge as *n* is increased. A second problem with MPPT is that it only yields accurate results if the HF wavefunction (the zero-order/unperturbed wavefunction) is a valid approximation to the real wavefunction.

7.5.4.2 Coupled-cluster theory

Perturbation methods add all types of corrections to a given order. The idea behind Coupled-cluster (CC) methods is to include all corrections of a given type to infinite order, and thereby constitute a hierarchy of models that systematically recover more and more of the electron correlation. The CC wavefunction is given by

$$\Phi_{\mathrm{CC}} = e^{\hat{T}}\Phi_{\mathrm{HF}}; \quad e^{\hat{T}} = \sum_{k=1}^{\infty}\frac{1}{k!}\hat{T}^{k}, \tag{7.18}$$

where $\hat{T}$ is the Cluster operator defined by $\hat{T} = \hat{T}_1 + \hat{T}_2 + \ldots + \hat{T}_N$ and where N is the total number of electrons in the system. The $\hat{T}_l$ operator generates all configurations having l excitations from the reference determinant (the HF wavefunction). In the CCSD model [67-70] the Cluster operator is truncated to $\hat{T} = \hat{T}_1 + \hat{T}_2$, while in the CCSD(T) model [71] triplet excitations are included using perturbation theory.

Coupled-cluster theory is presently the most successful wavefunction theory. By its design, CC theory offers a hierarchical set of size extensive methods and the exact solution can be approached in a systematic manner. The CCSD(T) model gives very accurate results [65], but is computationally very expensive.

7.5.5 Density functional theory

The electronic structure methods presented so far are so-called ab initio methods. That is, they have been derived from first principles of quantum mechanics and the many-electron system is described by its wavefunction.

The basis for Density Functional Theory (DFT) is the proof by Hohenberg and Kohn [72] that a many-electron system can be described fully and exclusively in terms of its ground state electron density ρ, that is, the one-particle density. The significance of this is: (i) each observable quantity of a stationary quantum mechanical system can in principle be computed exact from ρ, i.e., each observable quantity can be written as a functional of ρ, and (ii) the ground state electron density can in principle be computed exact from a variational principle involving only the density. However, the mathematical form of the general exact energy functional is not known.

This issue is addressed in Kohn–Sham (KS) theory [73], where the energy functional is splitted into the following functionals: kinetic energy of a Slater determinant, attraction between nuclei and electrons, Coulomb interaction between the electrons, and a functional containing all the unknown terms – the *exchange-correlation functional*, $E_{\mathrm{xc}}[\rho(\boldsymbol{r})]$. In KS theory the electron density is written as a sum of KS orbitals which are eigenfunctions of the KS one-electron operator:

$$\rho(\mathbf{r}) = \sum_{i=1}^{N} \left|\phi_i(\mathbf{r})\right|^2 . \tag{7.19}$$

KS theory is the basis for the DFT methods used today. The difference between the methods is how the exchange-correlation functional is treated. In the local density approximation (LDA) it is assumed that the functional depends only on the value of the density at each point in space and that the local density can be described as a uniform electron gas. However, the density is not uniform. An improvement to LDA is to let the functional also depend on the gradient of the density; the generalized gradient approximation (GGA).

By writing $E_{\mathrm{xc}}[\rho(\boldsymbol{r})]$ as a sum of a exchange functional and a correlation function, a bewildering variety of methods has been designed. Hybrid DFT methods have also been designed which mix in HF exchange energy. One of the most successful methods is B3LYP, which is a combination of Becke's three-parameter hybrid exchange functional [74] and the correlation functional of Lee, Yang, and Parr [75]. The three parameters are fitted to experimental data, making B3LYP a semiempirical method rather than an ab initio method.

DFT methods are computationally quite cheap and give in many situations a very good description of the electronic structure. DFT may therefore be considered as the workhorse of computational chemistry. However, because of the nature of the exchange-correlation functional, it is not possible to design a hierarchy of methods that provide a systematically better description of the system. Further, DFT methods in general also have problems with describing dispersion forces and bond-breaking processes unless specially designed functionals are used.

7.5.6 Basis Sets

The most obvious choice of basis functions is Slater Type Orbitals (STO) which have the functional form:

$$\chi_\mu \propto \exp(-\zeta r)\,, \tag{7.20}$$

where ζ is the orbital exponent. As can be seen, STOs have the same exponential dependence on the distance between the nucleus and the electron, *r*, as the exact orbitals for the hydrogen atom. However, STOs are not very useful for electronic structure calculations on larger systems as it is very difficult to solve four-center integrals.

To circumvent these difficulties, Gaussian Type Orbitals (GTO) were introduced which have the functional form

$$\chi_\mu \propto \exp(-\zeta r^2)\,, \tag{7.21}$$

The advantage of GTOs is that a four-center integral is reduced to a two-center integral which makes the evaluation of the integral simpler. However, the r^2 dependency in the exponential of the GTO makes the GTO inferior to the STOs in two aspects. At the nucleus the GTO has zero slope while the STO has a cusp (discontinuous derivative). Secondly, the GTO falls off too rapidly far from the nucleus compared with an STO. The tail of the wavefunction is consequently represented poorly. It is therefore necessary to use more GTOs than STOs to achieve the same accuracy. Another problem with GTOs is that Cartesian GTOs do not give the same orbitals as spherical GTOs. A d-type spherical GTO has five components, while a Cartesian GTO has six components.

A minimal basis set would consist of only enough functions to describe all electrons in the neutral atoms. However, to achieve more accurate results, it is necessary to add flexibility to the basis set. A first improvement would therefore be to double all basis functions; this is called a *double zeta* (DZ) basis set. Realizing that the valence electrons are the ones that are chemically important, suggest that a DZ basis set can be simplified by only double the number of basis functions describing the valence orbitals; this is called a *split valence* double zeta (VDZ) basis set. The next improvement would be a *triple zeta* basis set and so on.

One has experienced that it is necessary to augment a given basis set with special functions to obtain higher accuracy. To describe the polarization of the atomic charge distribution in a molecular environment, e.g. a chemical bond, it is necessary to use basis functions having higher angular momentum than the occupied atomic orbitals. These basis functions are called *polarization* functions. In order to describe loosely bound electrons (anionic species, excited states, bond-breaking processes, etc.), it is necessary to use basis functions with small orbital exponents, so-called *diffuse* functions. Similarly, functions having large exponents – *tight* functions – are needed for describing the electron density close to the nuclei.

The fact that many basis functions are used to describe the energetically important, but chemically relatively unimportant, inner shell electrons, is the foundation for using contracted basis sets which is written as a linear combination of primitive GTOs. The two most widely used families of contracted Gaussian based basis sets are the Pople style basis sets ranging from the minimal STO-3G basis set [76] up to 6-311++G(3df,3pd) [77], and the correlation-consistent basis sets of Dunning. The Dunning basis sets, symbolized as cc-pV*X*Z where *X* = D, T, Q, 5, 6 [78;79], are constructed so that the error in the energy from the sp basis is approximately equal to the error in the correlation energy due to the incomplete polarization space. The sp basis is increased as the polarization space is increased. These basis sets therefore constitute a systematic hierarchy of basis sets that converge towards the basis set limit. They can also be augmented by diffuse functions; this is indicated by an "aug" prefix [80].

The basis sets described above are the basis sets of choice for describing molecular systems, but not for describing periodic systems like crystals. For this situation so-called plane wave basis sets are more appropriate. Plane waves are the exact eigenfunctions of the homogeneous electron gas and form an orthonormal basis set that does not depend on the position of the atoms.

8 Adsorption of chemical warfare agents on oxides

8.1 Introduction

Numerous studies of the interaction between oxides and nerve agents and simulants have been reported in the literature. The most commonly studied oxides are calsium oxide (CaO), aluminum oxide (Al_2O_3), iron(III) oxide (Fe_2O_3), titanium dioxide (TiO_2), silicon dioxide (SiO_2), and magnesium oxide (MgO). Many of the studies have been motivated by the fact that the oxides may adsorb and decompose chemical warfare agents (CWA). However, in these studies the oxides have often been nanosize materials since it is preferable with large surface areas for quicker decontamination. The chemical compounds are nevertheless the same, and it is natural to assume that bonding sites and mechanism also will be valid for regular oxides. In the following, the adsorption of chemical warfare agents and simulants on these oxides is reviewed. Nanoparticles are mentioned explicitly, otherwise the oxides are regular.

8.2 Adsorption and decomposition of sulfur mustard on oxides

This chapter will offer a review on different articles found on the sorption of sulfur mustard (HD) on different metal oxides. A short comparison of results found from degradation over regular CaO and nanosize CaO will first be given; this to justify the assumption that the many bonding properties being valid for the nanosize materials are also valid for the regular, commercial material. Thereafter a study of the effect from different acid and base site on a metal will follow. An overview over the different reaction products from the degradation is also given. The last sections will then give more details on the bonding mechanisms between the surface and HD or the degradation products.

8.2.1 Calcium oxide: Nano oxides versus regular oxides

Wagner et al. studied in 2000, using ^{31}P and ^{13}C MAS-NMR, the degradation of 2-CEES on nanosize CaO (aerogel prepared, AP-CaO) and regular CaO [81]. The results from their study are shown in Table 8.1. The main difference between the two oxides is the reaction time. As can be expected AP-CaO with its large surface area, highly reactive edges and corner "defect" sites [82], breaks HD down much faster than commercial CaO. However, the fraction between elimination products and hydrolysis product is similar for nanosize and regular CaO.

Table 8.1 Decomposition of HD and 2-CEES on AP-CaO and regular CaO (see text for details) [81].

compound/material/ hydration	NMR method	induction period / h	initial half life / h	steady-state half life / h	elimination/ hydrolysis / %
HD/AP-CaO/"as received"	^{13}C	5	8.7	8.7	80/20
HD/AP-CaO/"aged "as received"	^{13}C	1	3.5	3.5	80/20
HD/AP-CaO/"wet"	^{13}C	none	3.1	> 46	80/20
HD/AP-CaO/"dried"	^{1}H	none	4.0	> 264	5/95
HD/CaO/"as received"	^{1}H	0.67	31	> 1176	80/20
HD/CaO/"wet"	^{13}C	none	9.1	> 1176	60/40
2-CEES/AP-CaO/aged " as received	^{1}H	none	<0.2	>135	5/95
2-CEES/AP-CaO/"dried"	^{1}H	none	1.7	> 156	30/70

8.2.2 Effect of acid and base sites on degradation

Tang et al. [83] studied the degradation at 298K of HD over different metal oxides, CaO (amorphous reagent), MgO (amorphous reagent and nanosize), SiO_2 (amorphous reagent), Al_2O_3 (nanosize and support), the zeolite HZSM-5[10], and A-Clays[11]. This work was done to figure out the effect of different acid and base sites on different oxides used for degradation of HD. Methods used for identification were gas chromatography–flame photometric detection (GC-FPD), gas chromatrography–mass spectrometry (GC-MS), NMR, and ultraviolet-visible spectroscopy (UV-VIS) To characterize the strength of the base and acid sites at the surface, temperature-programmed desorption with CO_2 and NH_3, respectively, were used. CaO and MgO had strong base sites, but no acid sites. The SiO_2 and the Al_2O_3 surfaces possessed both acid and base sites. HZSM-5 and A-clays were mainly acid with some contribution of base sites. The oxide surfaces were partly contaminated with CO_2 and H_2O from air and the free acid and base sites were assumed to be the reaction centre for reactions with HD molecules. All the oxides adsorbed both HD vapour and droplets and followed an adsorption isotherm of type II (see section 5.2.4.1). The activity of the surface was in addition to the base-acid properties found to be dependent on the

[10] The chemical formula for ZSM-5 is $Na_nAl_nSi_{96-n}O_{192}\cdot 16H_2O$ [84]. The ratio between Si and Al in ref. [83] is 50.

[11] The formula of A-Clay in ref. [83] is $Si_8Al_4O_{20}(OH)_4\cdot nH_2O$.

temperature and the adsorbed H_2O. Both increasing the humidity and exposing the oxides directly with H_2O increased the degradation rate.

Hydrolysis products were detected all over the surfaces independent of their acid-base properties. The nano materials gave the fastest reaction rate. However, an augmentation of surface acidity or basicity or more humidity accelerated the degradation of HD over the oxides. Nanosize Al_2O_3 gave the highest degradation rate with an activation energy of 34.2 kJ/mol. The difference between wet and dry surface was found to be most evident for the basic oxides. More than 10 different products from degradation of HD were investigated with FC-FPD, GC-MS, NMR and UV-VIS approaches. The main products are TG, CH and HEVS. The chemical formulas of the different reaction products are given in Figure 8.1.

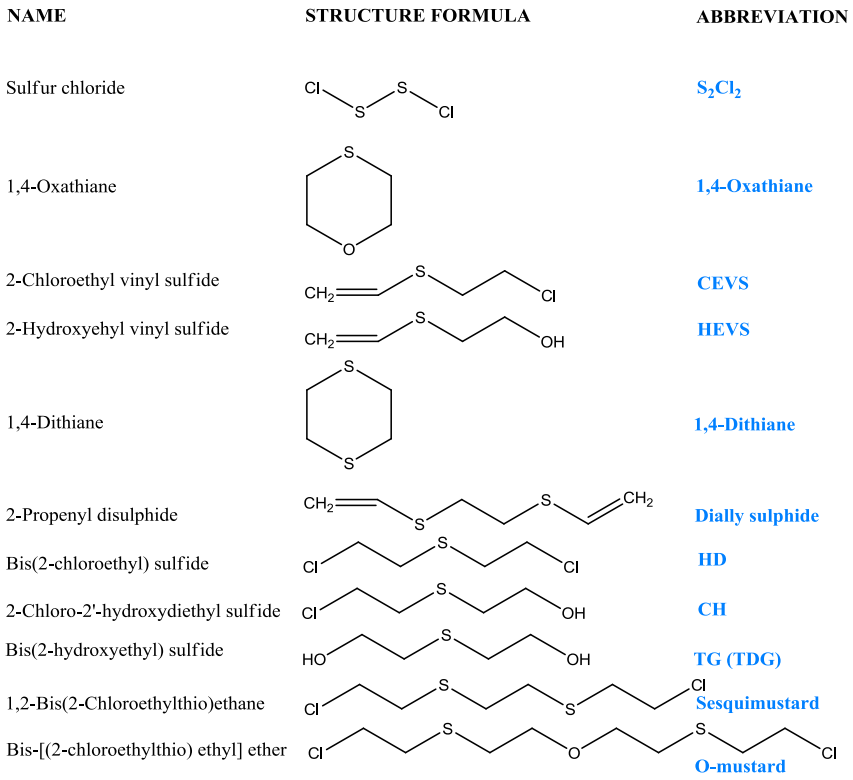

Figure 8.1 Identities of the compounds detected for HD reaction with oxides (after ref. [83]).

The suggested reaction mechanism is two-parted. The elimination of HCl from HD proceeds at the basic sites of the oxides and possibly also at the Lewis acid site of the oxides. The intermolecular addition-elimination for HD over the oxides happens through cleavage of C-S and C-Cl bonds, most likely activated by an H^+ proton from the hydrolysis or a surface acidic site. A schematic review of the reaction procedure is given in Figure 8.2. The different products from HD over the oxides might have been achieved from different reaction pathways. Elimination of HCl is a major pathway at the basic sites, whereas the intermolecular addition-elimination proceeds at

the acidic sites. Products from HD with –OH and C=C groups most likely were formed from hydrolysis of C-Cl and elimination of HCl (C_α–H, C_β–Cl)[12] respectively.

If the hydrolysis is followed by intramolecular elimination of HCl, 1,4-oxathiane will be produced. Hydrolysis to CH followed by an intermolecular elimination of H_2O (from the OH groups) will form O-mustard. Cleavage of both C-S and C-Cl bonds in two HD molecules will form 1,4-dithiane and sesquimustard. Dially sulphide can again be formed from sesquimustard through intramolecular elimination of HCl. The kind of detected degradated HD product can vary due to ongoing transformation of products into more stable compounds. However, as long as H_2O is present the hydrolysis of HD can continue [83].

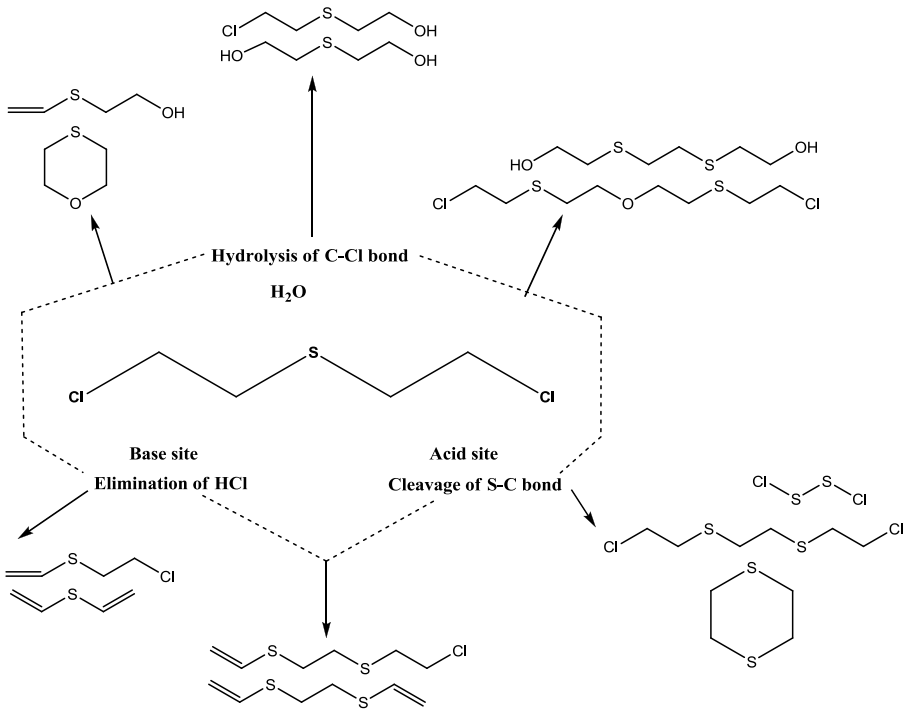

Figure 8.2 The role of acid-base sites on the degradation pathways of HD over different oxides (after ref. [83]).

8.2.3 Metal oxides in wet area

Wagner et al. made in 1998 a ^{13}C MAS NMR study of HD in soil [86]. HD will in reaction with water, quickly be hydrolyzed into CH and TG. On AP-CaO [81] Wagner et al. detected the sulfonium ion CH-TG which is a result from the reaction of CH and TG hydrolysis product. These ions tends to form when HD is in contact with water [86] and the formation of CH-TG is a reversible reaction. However, if the CaO surface is heavily hydrated the formation of sulfonium ions will be stopped. The same formation will also be hindered in environments of dilute homogenous solutions and at surfaces where destructive adsorption occurs. This can be seen in Figure 8.3 where the different hydrolysis product are immediately bond and hence hindered to react with

[12] The alpha carbon in organic chemistry refers to the first carbon that attaches to a functional group (the carbon is attached at the first, or alpha, position). By extension, the second carbon is the beta carbon [2] and so on [85].

neighbouring hydrolysis products. On surfaces and in solutions HD droplet formation hinders the overall hydrolysis rate since only molecules at the droplet surface react [86].

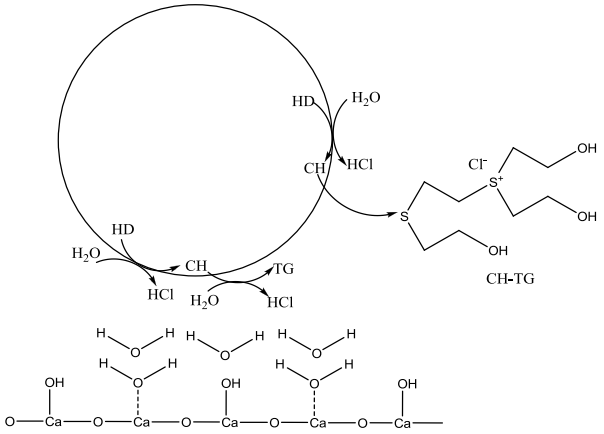

Figure 8.3 Hydralizing environment hinder sulfonium ion formation [81].

8.2.4 Alumunium oxide (Al_2O_3)

FT-IR-spectroscopy was used by Mawhinney et al. to study the details of the interaction between nanosize-Al_2O_3 and 2-CEES [87]. Their observations are summarized in Figure 8.4.

Part I shows the reactions for a hydrolyzed surface at temperatures between 303 and 473 K. Two reactive sites were present at Al_2O_3, isolated hydroxyl sites and Lewis acid-base sites. At 303 K 2-CEES is bonded to the surface. The sulphur atom in 2-CEES acts as a Lewis base and donates electrons to the Al^{3+} Lewis acid site, forming a donor bond. Once adsorbed onto the surface of alumina, the chlorine atom with rich electron density, interact with the isolated hydroxyl group, forming hydrogen bondings[13] (characterized by a C-O stretching mode near 1100 cm^{-1}). At 473K the hydrogen bond is splitted by hydrolysis reaction to produce HCl gas.
Part II illustrates the reactions on an ”ideal” surface, i. e. a surface without OH bondings. (The surface has been idealized by thermally treating with T>1073 K under vacuum). It is suggested the O^{2-} Lewis base donates electrons to the carbon atom closest to the chlorine atom. The electron-rich chlorine atom couples to the electron-deficient Al^{3+} Lewis acidic site (streching mode of 1100 cm^{-1}). The reaction hence continues with splitting of the C-Cl bond. 2-CEES is hence adsorbed as two dissociated species, resisting as an Al^{3+}-Cl -bond and an $O^{-}C_2H_4SC_2H_5$ bond [87].

[13] It is known that halogenated organic compounds undergo hydrolysis reactions at the halogen-carbon bonds in solutions. In an organic molecule with a sulphur atom in the α or β position to the chlorine atom, the chlorine-carbon bond will be activated. Simplified this can be thought of as sulphur donating electron density to chlorine allowing the chlorine to dissociate (see ref. [87] and references therein).

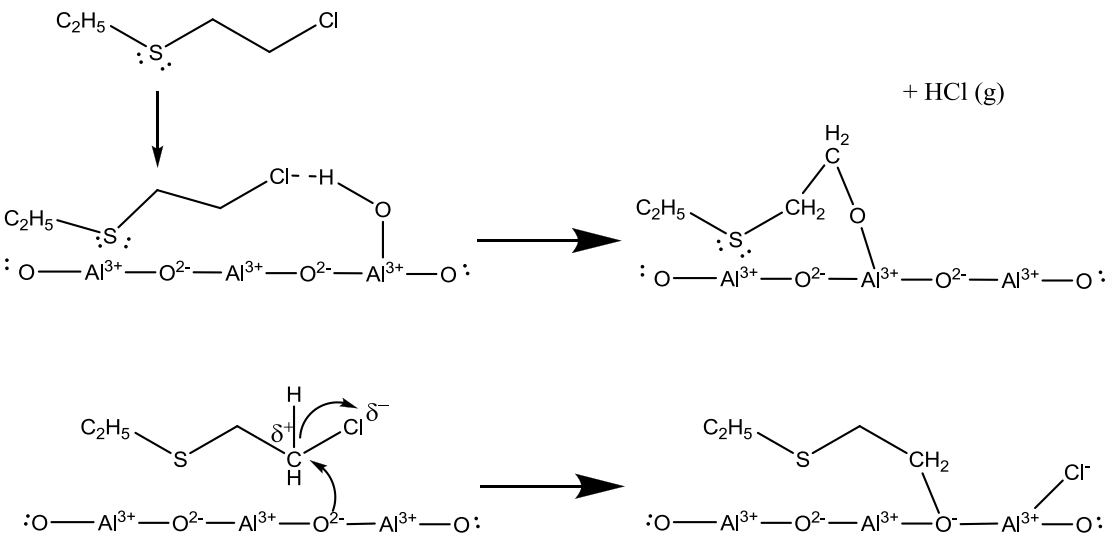

Figure 8.4 Representation of the two reaction pathways of 2-CEES with the active sites created on the Al_2O_3 surface. Reaction I is dominant in the presence of isolated Al-OH groups. Reaction II is dominant for highly dehydroxyled, "ideal", Al_2O_3 (after ref. [87]).

As the reaction of 2-CEES adsorbing on Al_2O_3 proceeds, the $ClC–H_2$ scissor vibrational mode increases in intensity the first few minutes and thereafter decreases. After five minutes a new mode emerges, interpreted as the $Al–O–CH_2$ streching mode. This indicates a bond between the hydrolysis product and the surface $–AlO-C_2H_4SC_2H_5$ (see ref. [87] for details).

In 2000 Mawhinney et al. [88] made an extensive study of the interaction between the various hydroxyl groups on the γ-Al_2O_3 surface (powder) and 2-CEES at different low temperatures. Al_2O_3 has due to its surface structure, five different OH groups [89]. The OH groups differ by their coordination to the surface (giving different stretching mode in the IR spectrum). They concluded that the diffusion and reaction on partially dehydroxylated Al_2O_3 can be divided into four different thermal stages. At temperatures between 140-153 K, 2-CEES is frozen on the outer surface of the Al_2O_3 powder. 2-CEES is hence mainly interacting with itself. For temperatures between 153-273 K, 2-CEES gain enough energy to overcome the diffusion barrier and diffuses into the porous Al_2O_3 and interacts with both the basic and acidic Al-OH groups. As the temperatures rise above 273 K, 2-CEES gets sufficient energy to break the bondings with the acidic Al-OH groups. When the temperature has exceeded 298 K 2-CEES is bound to the Al^{3+} sites. When the system has high enough energy, hydrolysis reaction with the neighbouring isolated Al-OH groups will occur. The different stages are shown in Figure 8.5. In addition to the strong interaction between C and Al-OH groups, a fraction of the interaction with the Al-OH groups most likely occurs through the sulphur atom in 2-CEES (see ref. [88] and references therein). Mawhinney et al. showed the hydrolysis product of 2-CEES, 2-hydroxyethyl ethyl sulphide was bond to the alumina on the surface. This also suggests that the hydrolysed product from HD, TG, also bonds to aluminum.

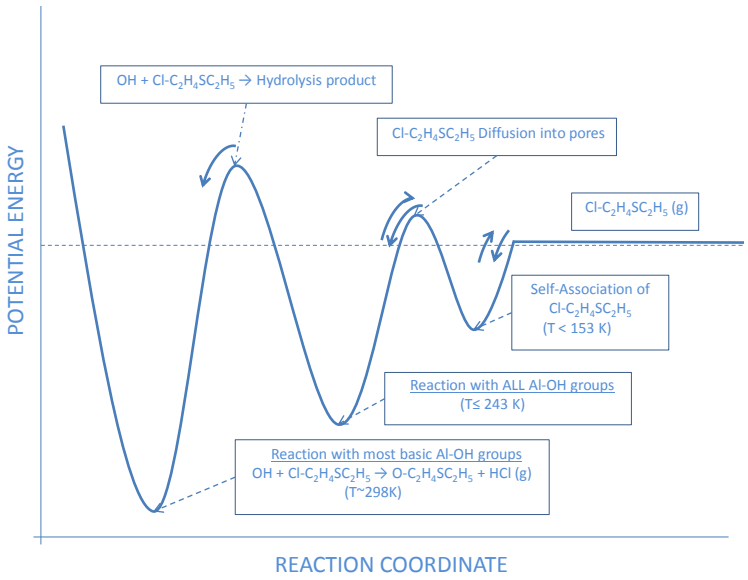

Figure 8.5 Schematic representation of the diffusion and reaction events for 2-CEES adsorbing on Al_2O_3 shown in a potential energy diagram (reproduced after [88]).

Wagner et al. investigated in 2001 with MAS-NMR reaction rates and products for nerve agents and sulphur mustard reaction on the surface of nanosize Al_2O_3 at room temperature [90]. Later Wagner also studied the reactions of VX, GD, and HD with conventional Al_2O_3 [91]. It was found that all VX, GD and HD hydrolyzed on both nanosize and conventional Al_2O_3. shows the reaction half-life times for the different adsorbates and surfaces of Al_2O_3. The half-life time of the adsorbates can be ranked as follows: GD < HD << VX. The ranking is the same as for the vapour pressure of the chemical warfare agents. The less vapour pressure, the less of the CWA can diffuse into the pores of the nanosize material, the slower the reaction rate [90]. The reaction capasity for nerve agents on metal oxides is high; this can be explained from the surface-bound acid hydrolysis product which causes quick erosion of the alumina surface to form bulk alumina phosphate complexes [90]. HD is less reactive. However, the droplet size of both HD and VX had a significant effect on the reaction kinetics.

shows that 13 µL and 3.5 µL HD on γ- Al_2O_3 have half-life times of 70.9 and 0.7 h respectively. At high loadings the reaction capacity of Al_2O_3 is overwhelmed and no reaction products can be observed. The effect was less on GD, since GD has large water solubility and hence spread more rapidly on the hydrated alumina surface.

Table 8.2 Reaction half-life times for the degradation of HD, GD, and VX on γ-Al_2O_3 and AP-Al_2O_3 [91].

chemical warfare agent	amount / µL	oxide	half-life time ($t_{1/2}$) / h
HD	13	γ-Al_2O_3	70.9
HD	3.5	γ-Al_2O_3	0.7
GD	16	γ-Al_2O_3	1.8
VX	15	γ-Al_2O_3	220.8
VX	3.5	γ-Al_2O_3	163.2
HD	3.5	AP-Al_2O_3	6.3
GD	3	AP-Al_2O_3	1.8
VX	3.5	AP-Al_2O_3	153.6

The more HD present on the surface of Al_2O_3, the more water is needed for hydrolysis. For low loadings of HD, the main product is thiodiglyocyl (TG, 71%). In addition, CH-TG sulfonium ion (12%) and elimination of HCl (17%) are observed. At high loadings and wet conditions mainly H2-TG and CH-TG are produced, analogues to hydrolysis of bulk HD droplets in water. The degradation rate for HD on γ- Al_2O_3 being higher than on AP-Al_2O_3 can be caused by different surface hydration state, since these states were not controlled [91].

New MAS-NMR experiments from 2009 [92], showed that for HD adsorbed on neutral dry alumina no degradation products could be detected. However, the signal broadening in the NMR spectrum indicated physisorption of HD onto the surface. When the alumina was wetted (5 wt-%), CH-TG and H-2TG was produced. This shows again that the destruction rate for HD depends on the amount of water present.

8.2.5 Titanium oxide (TiO_2)

Titanium oxide (TiO_2) is an interesting photooxidation catalyst since at sunny weather a surface of TiO_2 can be self-cleaning [93]. Thompson et al. [94] studied the adsorption of 2-CEES on reduced TiO_2(110) and on partially dehydroxylated high area anatase and rutile powered samples of high-area TiO_2. To study the surface chemistry of TiO_2(110) temperature-programmed desorption mass spectrometry, TPD-MS, and Auger spectrometry were combined. The desorption rate parameters were found by thermal desorption measuresments. On the powdered samples FT-IR was used. On TiO_2(110) the 2-CEES is strongly chemisorbed and oxidized by lattice oxygens. At reduced TiO_2(110) the monolayer was completely saturated at pressure of 7×10^4 molecules/cm^2. The activation energy was 105 kJ/mol and the desorption of the monolayer starts at ~270 K. At higher pressure multilayers may adsorb on top of the monolayer, but these layers will desorb at lower temperature. Weak interactions are measured in the monolayer. At 400 K all the 2-CEES parent molecules are desorbed, but decomposed species are still present. In the anatase and rutile TiO_2 the 2-CEES molecules are primarily oxidized by Ti-OH groups, and at 550 K lattice oxygen from TiO_2 also participate. The C–S bond is broken to produce chloroethoxy ($ClCH_2CH_2$–O–Ti) and ethoxy groups (CH_3CH_2-O-Ti), respectively. At the high area surfaces, Ti–OH groups are

still present and hydrogen bonds connect 2-CEES to Ti–OH groups via both chorine and sulphur [95]. At temperatures above 550 K these species react further to COO and CO_3. At 900 K the surface is clean [94].

Martynov et al. [93] made an experiment of photocatalytic destruction of 2-CEES at pure TiO_2. Gass chromatographic mass spectrometry GC-MS, was used for the qualitative and quantitative studies. In addition IR was used to sustain the results. From experiments performed at 25 °C and 80 °C they detected with in-situ IR analysis a wide array of intermediates with different toxicity (eight primary intermediates). The final products were H_2O, CO_2, SO_2, SO_4^{2-}, and HCl. The temperature increase seemed to change the production rates.

Panayotov et al. present in their article from 2004 [96] results from destruction of 2-CEES over the mixed photocatalyst TiO_2–SiO_2 at temperature 200 K. The instrument used was a dual beam IR–UV reactor. From their study they concluded that photooxidation of 2-CEES at this surface results in the formation of physiadsorbed CO_2 product, and other partially oxidized carbonyl containing products. These oxidized products block readsorption of 2-CEES by Si–OH groups on the used catalyst. The carbonyl products are in the opposite to CO_2, adsorbed via hydrogen bonding to the Si–OH groups. By heating under vacuum to about 300 K CO_2 will desorb. By further heating to 400 K the carbonyl-containing products may desorb. At 400 K the surface is reactivated and the ability of TiO_2–SiO_2 photocatalyst to fully adsorb 2-CEES is partly restored (one-fifth of the degradation rate of a fresh photocatalyst).

8.2.6 Magnesium oxide (MgO)

Wagner et al. [82] have with MAS-NMR studied the room-temperature degradation of sulfur mustard on nanosize MgO. MgO offers only basic sites. The degradation process is shown in Figure 8.2. Elimination of HCl at the base site leaves CEVS at the surface. In the hydrolysis part of the reaction H_2O reacts with HD or degradatation products to form CH and TG. TG bonds to the surface via the oxygen from TG and Mg from MgO ($\cdots H_2CO$–Mg). Broad 13C lines for TG in the NMR spectrum arise from either hydrogen-bonding with the surface or revealed reactive magnesium alkoxide; see Figure 8.7 for an illustration of the mechanism.

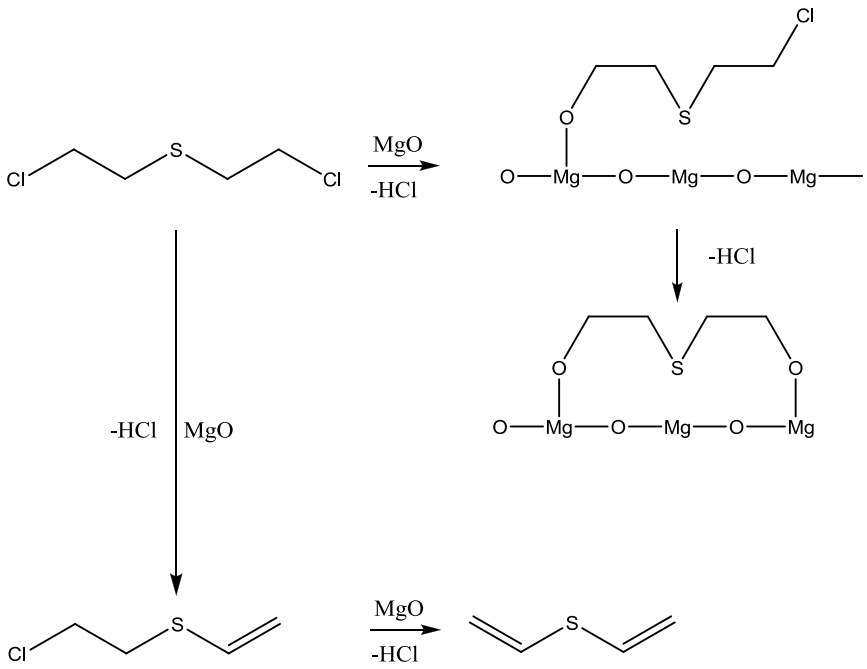

Figure 8.6 Reaction pathway for sulfur mustard (HD) on MgO [90].

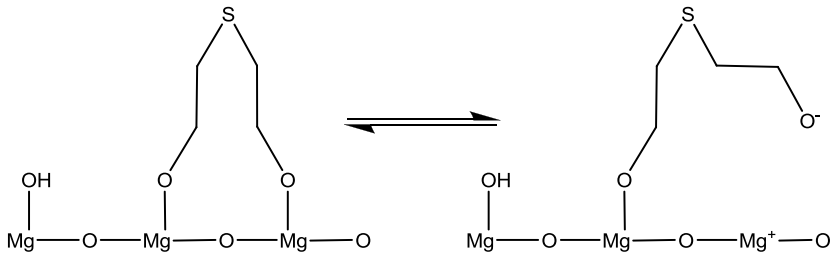

Figure 8.7 Bonding TG bond to the surface of nanosize MgO [82].

8.3 Adsorption and decomposition of nerve agents on oxides

8.3.1 Aluminum oxide (Al_2O_3)

The adsorption of dimethyl methylphosphonate [$(CH_3O)_2(CH_3)P(O)$, DMMP], a simulant for sarin (GB), on aluminum oxide was first studied by Templeton and Weinberg in 1985 [97;98]. Templeton and Weinberg used inelastic electron tunneling spectroscopy under ultra-high vacuum conditions to investigate the adsorption process over a temperature range from 200 to 673 K. The Al_2O_3 surface contained little, if any, physisorbed molecular water (H_2O), but some chemisorbed water (OH groups).

At 200 K, Templeton and Weinberg [97] found that DMMP adsorbs molecularly to the aluminum oxide surface. Two different adsorption sites on Al_2O_3 are available for DMMP: One where the phosphoryl group of DMMP is hydrogen-bonded to surface hydroxyls (Al–OH···O=P) as illustrated in Figure 8.8a, and a second site where DMMP is chemisorbed to coordinatively unsatu-

rated aluminum atoms via Al···O=P dative bonding[14]; see Figure 8.8b. Because of the character of the bond formed, the heat of adsorption should be considerably lower for the surface hydroxyl site than for the other site [97]. It was not possible to distinguish between the two structures (Figure 8.8a-b) on the basis of the phosphoryl stretching frequency since it is nearly the same for the two situations. To distinguish between the two structures, Templeton and Weinberg [97] carried out an experiment where deuterated DMMP [$(CD_3O)_2(CH_3)P(O)$, DDMMP] was first adsorbed to the aluminum oxide surface at 200 K, and then annealed the system to 295 K and back to 200 K to allow any weakly adsorbed molecules to desorb. DDMMP was used to avoid the occlusion of the phosphoryl spectral region by other strong vibrational modes. The inelastic electron tunneling spectra (Figure 2 in ref. [97]) showed that much of the DDMMP had desorbed after annealing, thus suggesting that virtually all the DDMMP is adsorbed to surface hydroxyls on the aluminum oxide surface at 200 K (Figure 8.8a).

As mentioned, there was a small but significant amount of DDMMP still adsorbed to the Al_2O_3 surface after warming to 295 K. This could be due either to the existence of strongly chemisorbed DDMMP as illustrated in Figure 8.8b, or the existence of dissociatively chemisorbed DDMMP. Templeton and Weinberg [97] investigated this situation further by exposing DDMMP to the aluminum oxide surface at 295 K and 473 K. The experiment suggested that DMMP adsorbs dissociatively to form methyl methylphosphonate [$(CH_3O)(CH_3)P(O)OH$, MMP] adspecies via cleavage of a H_3CO-P bond as illustrated in Figure 8.9. Above 573 K, the MMP adspecies decompose to yield tridentate methyl phosphonate adspecies.

Templeton and Weinberg [98] expanded their study of the adsorption of phosphonate esters on aluminum oxide to also include diisopropyl methylphosphonate [$((CH_3)_2CHO)_2(CH_3)P(O)$, DIMP] and diphenyl methylphosphonate [$(C_6H_5O)_2(CH_3)P(O)$, DPMP]. DIMP adsorbs molecularly to Al_2O_3 at 295 K and dissociatively at temperatures above 373 K, whereas DPMP adsorbs dissociatively already at 295 K. The findings of Templeton and Weinberg [97;98] was supported by Aurian-Blajeni and Boucher [99] who used FT-IR spectroscopy to investigate the interaction of DMMP with aluminum oxide.

[14] A dative bond is a coordination bond formed upon interaction between molecular species where one serves as a donor and the other as an acceptor of the electron pair to be shared in the complex formed. As such, dative bonds are analogous to covalent bonds, but the former are distinguished by their significant polarity, lesser strength, and greater length (ref. IUPAC Gold Book [10]).

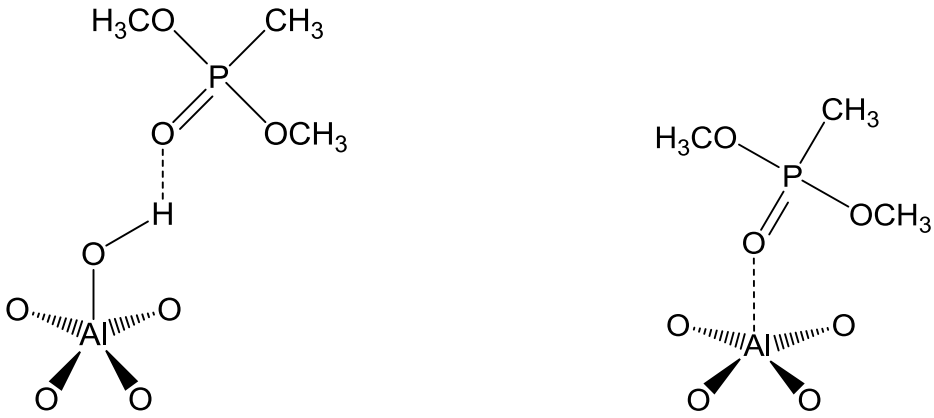

Figure 8.8 Adsorption of dimethyl methylphosphonate to (a) surface hydroxyls or (b) coordinatively unsaturated aluminum atoms on Al_2O_3 (after Templeton and Weinberg [97]). The models are not to scale.

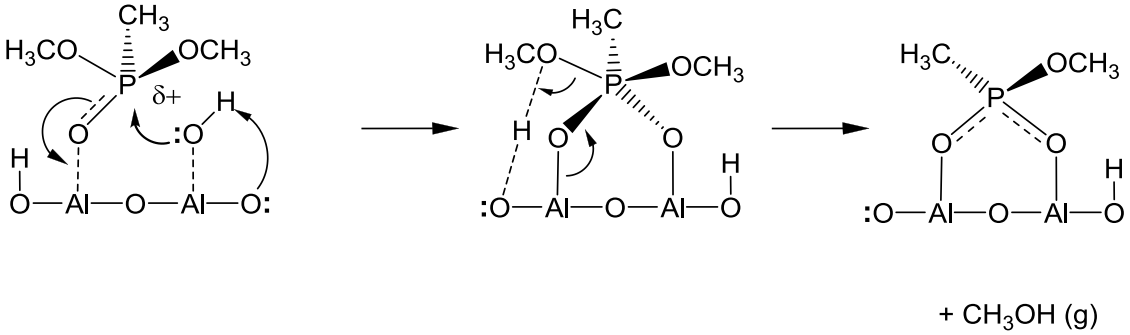

Figure 8.9 Dissociative adsorption of dimethyl methylphosphonate on Al_2O_3 (after Templeton and Weinberg [97]). The models are not to scale.

Further insight into the adsorption of nerve agents on aluminum oxide was gained by Bermudez [89;100] by means of quantum chemical calculations using density functional theory. The most interesting study is the one published in 2009, where Bermudez investigated the effects of photolysis and surface hydroxylation in the adsorption of DMMP, sarin, and VX on γ-Al_2O_3 [89]. The computational levels of theory used by Bermudez were the Perdew–Burke–Ernzerhoff (PBE) exchange functional and the Vosko–Wilk–Nusair (VWN) correlation functional together with the so-called TZP basis set, which is of triple-zeta[15] quality with a single polarization shell added (a p shell for hydrogens and a d shell for all other atoms).

The bulk and surface structures of the γ-phase of aluminum oxide are not well established. Bermudez [89] represented the bulk structure of γ-Al_2O_3 by a defective-spinel model, which is in line with the traditional view. The most stable surface in this model is the (111) surface plane formed by "cleaving" on the layer of vacancies. Further, Bermudez used two different cluster models to

[15] A triple zeta basis set contains three times as many basis functions as the minimum basis, which only contains enough functions to describe all the electrons of the neutral atom.

represent the (111)a surface: Al_8O_{12} and $Al_{32}O_{48}$ (see Figure 3 in ref. [89]). Ching and co-workers [101], on the other hand, found that γ-Al_2O_3 is better described as an amorphous network-like structure of Al-O bonds. The model for the bulk structure is important because it determines the structure and stability of the different surface planes. This, in turn, influences the identity and the distribution of both OH-free and hydroxylated reactive surface sites [89]. However, it is difficult to represent the surface structure with small cluster models if the surface has a large degree of disorder. In this respect the choice by Bermudez can be justified, but it should be kept in mind when interpreting the results.

The structure of the hydroxylated γ-Al_2O_3 surface is untrivial and not fully understood. The general consensus is that the O–H vibrational stretching mode falls in approximately the 3760–3800 cm^{-1} range for sites where OH is bonded to a single surface aluminum atom (type I sites), 3700–3750 cm^{-1} for sites where OH is bridged to two Al atoms (type II sites), and 3635–3700 cm^{-1} for sites where OH is bonded to three Al atoms (type III sites) [89]. However, to complicate the picture, for each type of site various combinations of octahedrally (O_h) and tetrahedrally (T_d) coordinated aluminum are possible. As a consequence, a type II site bridging two Al(O_h) sites, for example, will be chemically distinct from one bridging an Al(O_h) and an Al(T_d). For the (111)a surface studied by Bermudez [89], the types of sites formed are a type I Al(T_d)–OH site and two type III sites. For the first type III site, OH is coordinated to two Al(O_h) and one Al(T_d). For the second type III site, OH is coordinated to three Al(O_h) atoms (see Figure 3 of ref. [89] for details). Henceforth, the two type III sites will be referred to as type IIIa and type IIIb, respectively.

The Brønsted acidity[16] of the different types of OH sites is important when discussing the reactivity of the sites. Bermudez [89] have estimated the Brønsted acidity by calculating the deprotonation energy (ΔE_{dp}) for the different sites. For deprotonation of a species XOH, ΔE_{dp} is given as

$$\Delta E_{dp} = E(XO^-) + E(H^+) - E(XOH)\,, \tag{8.1}$$

where the energy of the species includes the electronic energy and the zero-point vibrational energy, and XO^- and H^+ are at infinite separation. ΔE_{dp} is positive and decreases with increasing acidity. For aluminum oxide, the deprotonation energy decreases in the order type I > type II > type III. That is, type III sites are most acidic. The type IIIa site is slightly more acidic than the type IIIb site [89].

We now turn to the adsorption of nerve agents on the aluminum oxide surface. In the study of Bermudez [89], the adsorption energy (ΔE_{ads}) is defined as

$$\Delta E_{ads} = E(\text{cluster} + \text{mol}) - E(\text{cluster}) - E(\text{mol}) + \Delta E(\text{BSSE})\,, \tag{8.2}$$

where the energies (E) are the relaxed total energies of the cluster with the adsorbed molecule, of the bare cluster, and of the free molecule, respectively. The last term, ΔE(BSSE), is a correction

[16] A Brønsted acid is a molecular entity capable of donating a proton to a base or the corresponding chemical species (ref. IUPAC Gold Book [10]).

for the basis-set superposition error (BSSE). BSSE is an artifact of the calculation owing to the use of incomplete basis sets. The quality of an incomplete basis set is not the same at all geometries because the electron density around one nucleus may be described by basis functions centered at other nuclei [64]. Consequently the cluster with the adsorbed molecule will be artificially lowered in energy, thereof the plus sign before the BSSE term. In the limit of a complete basis set the BSSE will be zero.

Table 8.3 summarizes the energetic of the adsorption of DMMP, sarin, and VX on OH-free γ-Al_2O_3 clusters. For all adsorbates the energetically most favorable configuration is dative bonding of the P=O group to the Lewis-acidic[17] Al(T_d) site. This is also the case for VX where one might expect the Al(T_d)···N interaction to be strong. The results of Bermudez [89] show, however, that the Al(T_d)···S interaction is stronger than the Al(T_d)···N interaction for VX, but both are significantly less than the interaction between the P=O group and the Al(T_d) site. However, care should be exercised in the interpretation of these results because a triple zeta basis set or larger augmented with diffuse functions is generally needed to obtain a good description of the sulfur chemistry [102].

If we turn to the adsorption of nerve agents on hydroxylated aluminum oxide surfaces, hydrogen bonds with surface OH groups might be of importance in addition to Al···O=P dative bonding. Bermudez [89] investigated the effect for different OH sites on the Al_8O_{12} cluster and the results are summarized in Table 8.4. For all adsorbates, P=O···OH(type IIIb) is the energetically most favorable hydrogen bond and the strength of the bond decreases in the order DMMP > sarin > VX. This is consistent with the higher Brønsted acidity of the type III OH sites compared to the type I sites. The interaction between surface OH groups and P–O–R, P–F, P–S, or P–N groups is significantly weaker than that of the P=O group. However, even the strongest OH···O=P bond is much weaker than an Al(T_d)···O=P dative bond on an OH-free surface. Thus, the latter bonding mode will occur whenever vacant Al(T_d) sites are available. However, the picture might have been modified if the TZP basis set had been augmented with so-called diffuse basis functions. Such functions are generally needed for a proper description of loosely bound complexes. Adding diffuse functions to the basis set will, however, significantly increase the computational cost. Finally, an interesting point is that the amine group of VX is able to extract a proton from a type III OH site to form the corresponding ammonium ion. The computed proton affinities show that the VX amine group is a stronger base than either pyridine or 2,6-dimethyl pyridine, and is comparable in alkalinity to triethyl- and tripropylamine [89].

[17] A Lewis acid is a molecular entity that is an electron-pair acceptor and therefore able to react with a Lewis base to form a Lewis adduct by sharing the electron pair donated by the Lewis base (ref. IUPAC Gold Book [10]).

Table 8.3 Energetics of the nondissociative adsorption of DMMP, sarin, and VX on OH-free γ-Al_2O_3 clusters for different bonding modes [89].[a]

cluster	adsorbate	ΔE_{ads} / kJ mol^{-1}				
		Al(T_d)···O=P	Al(T_d)···O–C	Al(T_d)···F	Al(T_d)···N	Al(T_d)···S
Al_8O_{12}	DMMP	−221.8				
	Sarin	−215.5	−129.7[b]	−109.6[b]		
	VX	−215.9			−127.2[b]	−145.6[b]
$Al_{32}O_{48}$	DMMP	−173.2				
	Sarin	−166.5				
	VX	−164.4				

[a] The adsorption energy (ΔE_{ads}) is defined in eq. (8.2).
[b] Not corrected for basis set superposition error.

Table 8.4 Adsorption energies (ΔE_{ads} / kJ mol^{-1}) for H-bonding to the Al_8O_{12} cluster [89].[a]

OH type	DMMP		sarin		VX[b]				
	P=***O***	P–***O***–Me	P=***O***	P–***O***–Me	P–***F***	P=***O***	P–***O***–Et	P–***S***–R	R′–***N***–(R″)$_2$
type I	−18.8	−20.9			−16.7	−10.0		+1.4	−15.9
type IIIa	−57.3	−41.2							
type IIIb	−97.1	−58.2	−91.6	−43.5	−36.8	−79.5	−33.5	−42.3	c

[a] All energies have been corrected for basis set superposition error. The bold, italicized atom is the one to which the H-bond is formed.
[b] R″ is a –CH(CH$_3$)$_2$ group; R′ is a –CH$_2$CH$_2$– group; R is the –R′N(R″)$_2$ group.
[c] Geometry optimization led to proton transfer from the surface OH group to the N atom.

8.3.2 Titanium dioxide (TiO_2)

Studies of the interaction of chemical warfare agents with titanium dioxide (TiO_2), have mainly focused on the adsorption and decomposition of simulants on TiO_2. Rusu and Yates [103] have investigated the uptake of DMMP on TiO_2 powder over a large temperature range by means of FT-IR spectroscopy.

At temperatures lower than ~160 K, DMMP condenses as a layer of ice on the outer surface of the titanium dioxide. No changes in the vibrational intensity of isolated Ti–OH surfaces species were observed, because condensed DMMP molecules cannot diffuse into the pores where the majority of the surface hydroxyl groups are situated.

As the temperature increases above 166 K, the DMMP molecules diffuse into the porous TiO_2 powder and interact with the hydroxyl groups found on the interior surface of the powder. This is observed as a shift of the P=O stretching mode to a lower vibrational frequency (from 1242 cm^{-1} for the condensed phase to 1210 cm^{-1} for the adsorbed phase), and the development of the 1210 cm^{-1} band is accompanied by a decrease in the intensity of the vibrational band assigned to isolated surface hydroxyl groups. The FT-IR spectra showed no perturbation of the C–O stretching mode, suggesting that the adsorption does not involve the CH$_3$–O– moiety of DMMP. Thus, the structure of the hydrogen-bonded complex is likely of the form illustrated by structure **I** in Figure

8.10 and not of the form illustrated by structure **II**. If Lewis acid (Ti^{4+}, Ti^{3+}) sites are available, DMMP may be chemisorbed to TiO_2 as illustrated by structure **III** in Figure 8.10 [103].

Above 214 K, the DMMP starts to decompose on the TiO_2 surface. The reaction is thought to occur as illustrated in Figure 8.11 where the DMMP is hydrolyzed to yield surface-bound methyl methylphosphonate and methoxy (CH_3O) species [103]. According to Kim et al. [104], the methoxy groups desorb from the surface at temperatures above 473 K, probably as gaseous methanol (CH_3OH). Above 573 K, a stable phosphate surface complex is formed [103;104]. Kim and coworker speculated that this complex, most likely methylphosphonate, may be responsible for poisoning effects observed during DMMP gas exposure of chemiresistive sensors operating in this temperature range.

These findings were supported by Panayotov and Morris [105;106] who also used FT-IR spectroscopy to investigate the adsorption of DMMP on TiO_2 nanoparticles. For the reaction illustrated in Figure 8.11, an Arrhenius activation energy of ~48 kJ mol^{-1} was observed over the temperature range 300–400 K, which is the same order of magnitude as observed for neutral and alkaline hydrolysis of phosphonate esters [106]. Panayotov and Morris also found that lattice oxygen plays a role in the degradation of adsorbates on the TiO_2 surface in the absence of gaseous oxygen. The quick poisoning effect of reactive sites by a strongly bound phosphorus compound was also observed by Panayotov and Morris. Thermal reactivation of the titanium dioxide particles in the presence of oxygen restores the physisorption capacity of the particles. However, the reactive adsorption pathway is almost completely eliminated [105].

The photodegradation of DMMP vapor on TiO_2 surfaces has been investigated by several research groups [107-109]. Irradiation of titanium oxide with ultraviolet (UV) light excites a valence band electron to the conduction band. The conduction band electron (e_c^-) and the valence band hole (h_v^+) may respectively reduce or oxidize species adsorbed to the surface. The reduction/oxidation process is thought to involve the production of superoxide anions (O_2^-) and hydroxyl radicals ($\dot{O}H$) as shown by eqs. (8.3)–(8.5) [108].

$$TiO_2 + h\nu \rightarrow e_c^- + h_v^+ \tag{8.3}$$

$$e_c^- + O_2 \rightarrow O_2^- \tag{8.4}$$

$$h_v^+ + H_2O \rightarrow H^+ + \dot{O}H \tag{8.5}$$

Obee and Satyapal [108] proposed that the photodegradation of DMMP may occur either by a hydrogen abstraction mechanism or by an addition-elimination mechanism involving the OH radical as illustrated in Figure 8.12. The formation of the methyl phosphonic acid ($CH_3P(O)(OH)_2$) and PO_4^{3+} products blocked further adsorption of DMMP vapor because these species are strongly bound to the adsorption sites. Interestingly, Obee and Satyapal found that washing the TiO_2 surface with water completely restored the catalytic activity of the adsorbent. The surface was also partially restored upon UV irradiation. Rusu and Yates [109] found that

heavy loading of DMMP on the titanium dioxide surface inhibited the photooxidation of DMMP due to site blockage for O_2 adsorption on the surface. This was not observed by Moss et al. [107] and the difference was attributed to the different reaction conditions in the two studies.

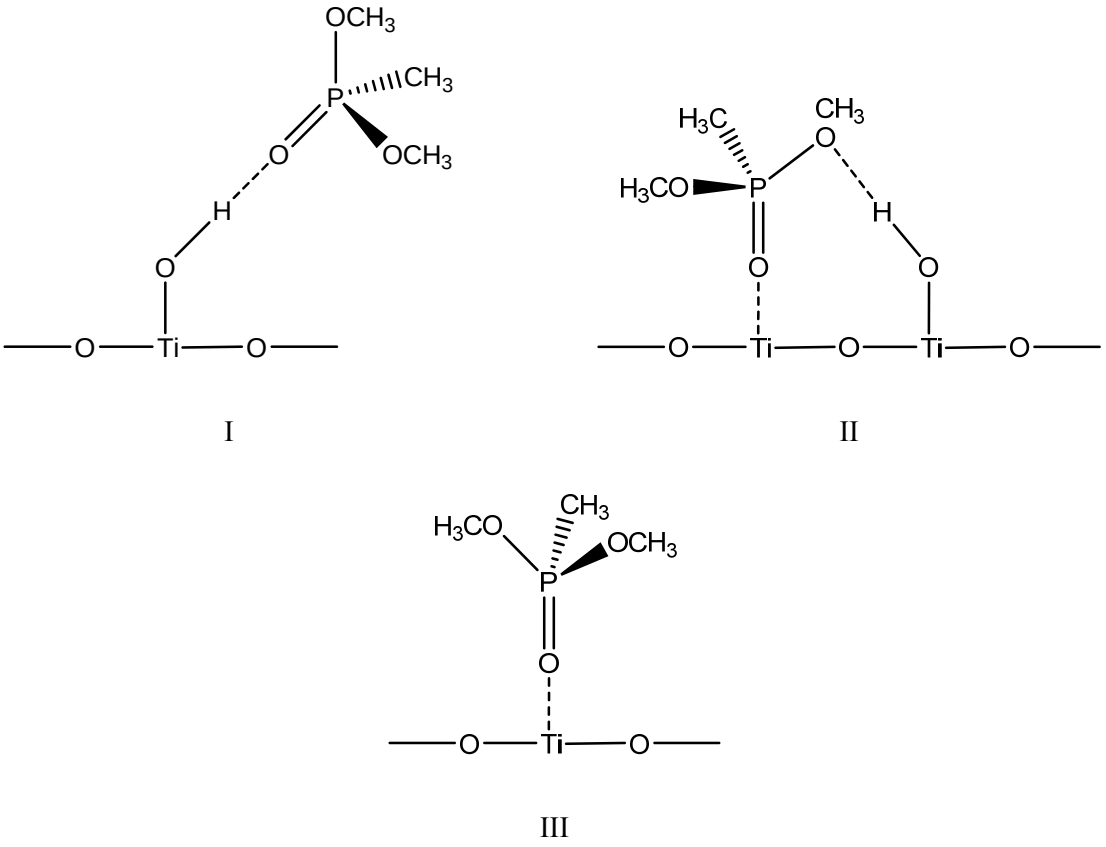

Figure 8.10 Structures of possible adorption complexes of dimethyl methylphosphonate (DMMP) on solid titanium dioxide (TiO_2) [103].

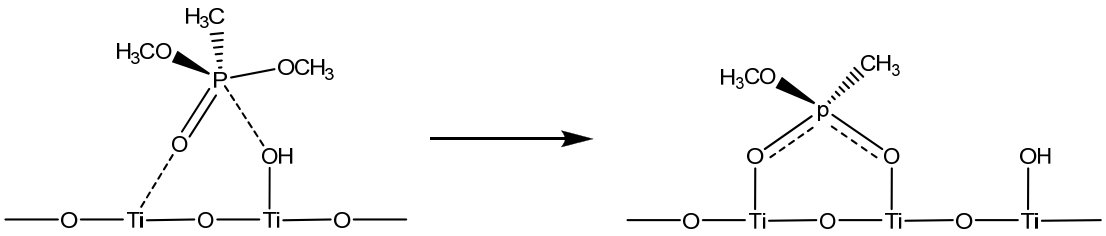

Figure 8.11 Decomposition of dimethyl methylphosphonate (DMMP) on solid titanium dioxide (TiO_2) [103].

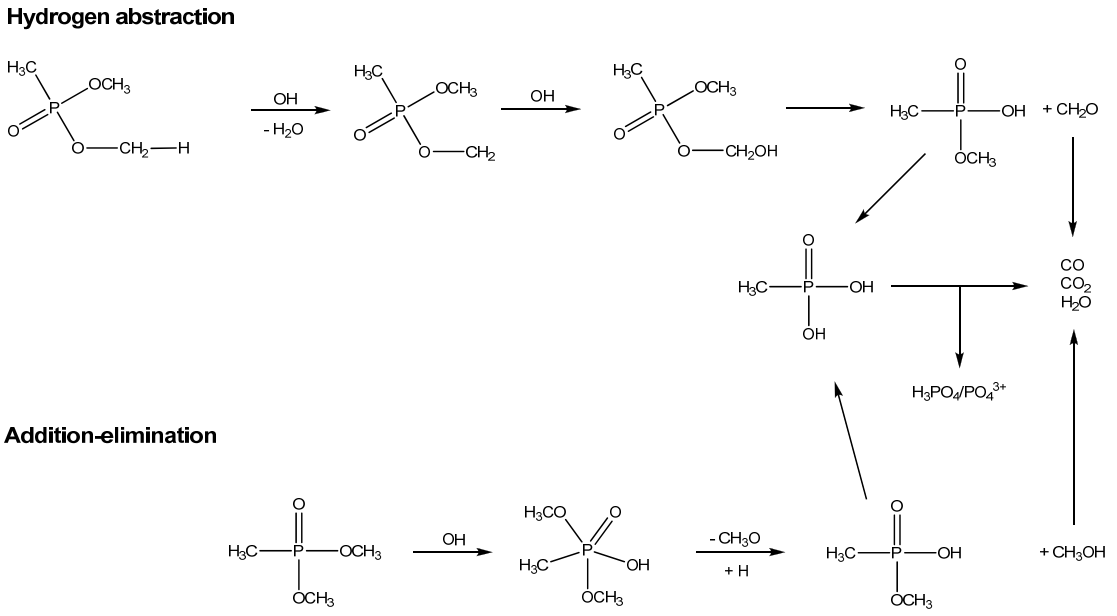

Figure 8.12 Proposed mechanism for the photodegradation of dimethyl methylphosphonate on a titanium dioxide surface (after ref. [108]).

8.3.3 Ferric oxide (Fe_2O_3)

The interaction of dimethyl methylphosphonate with α-Fe_2O_3 was studied by Henderson et al. [110] using temperature-programmed desorption and Auger electron spectroscopy. On the clean α-Fe_2O_3 surface multilayer adsorption of DMMP was observed at temperatures around 170 K. As the temperature approached 250 K, the DMMP started to decompose through oxidation of the P–CH_3 bond by lattice oxygens. Around 600 K further decomposition and desorption of all carbon-containing species in the form of CH_3OH, CO_2, CO, and HCOOH took place. Above 650 K phosphorus migrated into the bulk of the oxide, allowing for a partially regeneration of the iron oxide surface sites.

This behavior is different from what has been observed for other oxides. For e.g. aluminum oxide the P–CH_3 bond remained intact even at temperatures above 573 K [97;98]. Mitchell and co-workers observed the same mechanism for the decomposition of DMMP on alumina-supported iron oxide [111;112]. They postulated that the mechanism for the cleavage of the P–CH_3 bond is through the Mars and van Krevelen mechanism involving the Fe(II)/Fe(III) redox couple:

$$Fe_2O_3 + 2e^- \rightarrow 2FeO + O^{2-} \tag{8.6}$$

$$(H_3CO)_2P(O) - CH_3 + O^{2-} \rightarrow (H_3CO)_2P(O)^-_{ads} + H_3CO^-_{ads} \tag{8.7}$$

$$2FeO + \tfrac{1}{2}O_2(g) \rightarrow Fe_2O_3 \tag{8.8}$$

Multiple oxidation states are not available for the other oxides, which might explain why cleavage of the P–CH_3 bond was not observed for other oxides than Fe_2O_3.

The passivating layer formed in the bluing of steel, a technique commonly used by gun manufactures, consists of Fe_3O_4 (magnetite) [113]. Magnetite can be considered as $FeO \cdot Fe_2O_3$ [114]. It is therefore reasonable to assume that the decomposition of organophosphate esters on Fe_3O_4 follows a similar mechanism as that occurring on Fe_2O_3.

8.3.4 Silicon dioxide (SiO_2)

Henderson et al. [110] also investigated the adsorption of dimethyl methylphosphonate on silicon dioxide (SiO_2). At 200–205 K on dehydrated SiO_2, a multilayer of DMMP was observed. By annealing to 275 K, DMMP desorbed to form a monolayer on the surface. The monolayer molecularly desorbed according to first-order kinetics with an activation energy for desorption of about 71 kJ mol^{-1} (assuming a pre-exponential factor of 10^{-13} s^{-1}). No decomposition products were observed. On hydrated SiO_2 some decomposition of DMMP was observed, but no more than 10% of the monolayer. The only detectable decomposition products were methylphosphonate and methanol.

Kanan and Tripp [115] investigated the gas-phase adsorption of DMMP, trimethyl phosphate (TMP), methyl dichlorophosphate (MDCP), and trichlorophosphate (TCP) on silica using FT-IR spectroscopy. At room temperature, Kanan and Tripp observed that DMMP adsorbs through formation of hydrogen bonds with surface hydroxyl groups. This was evident from the redshift of the silanol (SiO–H) stretching mode from 3747 cm^{-1} to 3223 cm^{-1} accompanied with a blueshift of the SiO–H bending modes. The shift of 524 cm^{-1} for the silanol stretching mode tells us that the hydrogen bonds formed are quite strong. For comparison, adsorption of methoxysilanes shift the silanol stretching mode to 3350 cm^{-1}, whereas adsorption of triethylamine gives rise to a shift of the SiO–H stretching mode to 2677 cm^{-1} [115]. Amines are known to be very sticky to surfaces. Kanan and Tripp further observed that the adsorption of DMMP on silicon dioxide only involves formation of hydrogen bonds with surface silanol groups. In a separate experiment, a thin film of silica was first reacted with bis(trimethylsilyl)amine [$((CH_3)_3Si)_2NH$; also called hexamethyldisilazane] to convert all isolated silanol groups to $SiOSi(CH_3)_3$ species. After exposure of excess DMMP vapor at room temperature to the bis(trimethylsilyl)amine treated silica, no evidence of adsorbed DMMP could not be observed in the infrared spectra [115].

The desorption of DMMP, TMP, MDCP, and TCP at elevated temperatures was also investigated by Kanan and Tripp [115]. DMMP had desorbed completely at 573 K and no decomposition products could be detected. TMP, MDCP, and TCP also desorbed molecularly. The ease of desorption followed the order TCP (297 K) > MDCP (423 K) > DMMP (573 K) > TMP (673 K). The shift in the vibrational frequency of the silanol stretching mode (3747 cm^{-1}) followed the order TCP (3488 cm^{-1}) < MDCP (3425 cm^{-1}) < TMP (3262 cm^{-1}) < DMMP (3223 cm^{-1}). All four compounds showed a shift in the P=O vibrational stretching mode [115]. Thus, the trend in desorption as a function of temperature must be caused by differences in the type and number of hydrogen bonds formed between the different species and the surface silanols.

The observed behavior for the adsorption and desorption of TCP on silica can be explained by the formation of a single and relatively weak $SiO–H\cdots O=P(Cl)_3$ hydrogen bond (Figure 8.13a).

MDCP may adsorb to silica through the formation of two hydrogen bonds as illustrated by the structure given in Figure 8.13b, while three hydrogen bonds may be formed in the adsorption of TMP to silica (Kanan and Tripp [115] argues that the P=O moiety of TMP is not involved in hydrogen bonds with silanols because of steric hindrance). Thus, the observed trend for TCP, MDCP, and TMP may be explained by the structures given in Figure 8.13.

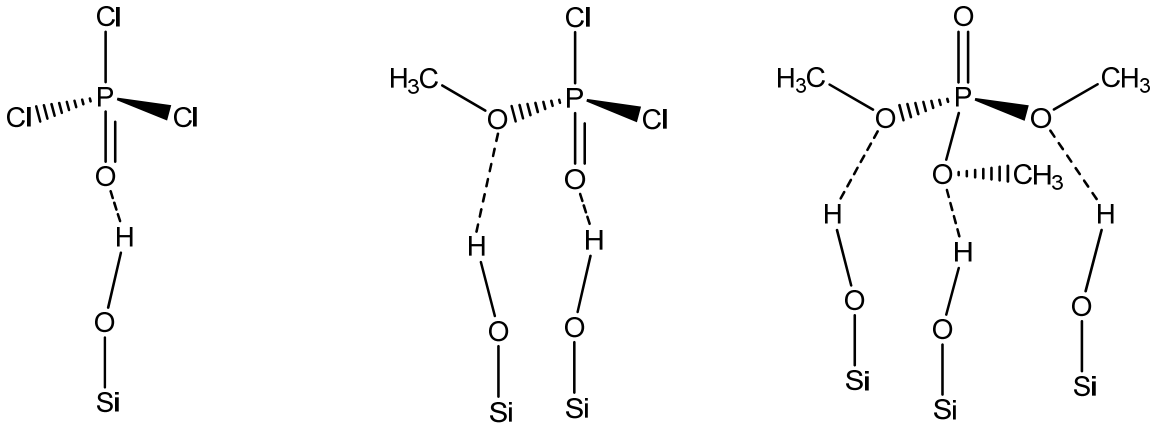

(a) (b) (c)

Figure 8.13 Structures of possible adorption complexes of (a) trichlorophosphate (TCP), (b) methyl dichlorophosphate (MDCP), and (c) trimethyl phosphate (TMP) on solid silicon dioxide (SiO_2) [115].

The question that arises then is why DMMP desorbs at lower temperatures than TMP even though the shift in the silanol stretching frequency is largest for DMMP. A priori, three different moieties of DMMP may interact with surface silanol groups, namely the P–CH_3, P=O, and P–O–CH_3 groups. The P–CH_3 group, however, cannot form hydrogen bonds with the silanol groups because the van der Waals interaction is too weak to cause the large shift in the silanol vibrational stretching frequency [115]. Instead, Kanan and Tripp observed a redshift in the P=O stretching mode from 1275 cm^{-1} for gaseous DMMP to 1256 cm^{-1} for adsorbed DMMP together with a disappearance of the O–CH_3 stretching modes at 1075 and 1049 cm^{-1}. The disappearance of the O–CH_3 stretching modes was not accompanied by any change in the C–H stretching mode of the methyl groups, implying that the absence of the O–CH_3 stretching modes is not due to elimination of the methoxy groups [115]. The interaction between DMMP and silica must therefore be through the P=O and P–O–CH_3 moieties.

Kanan and Tripp postulated two different structures for the hydrogen bonded complex of DMMP with surface silanols involving the P=O and P–O–CH_3 groups. These structures are depicted in Figure 8.14. If DMMP adsorbs to silica through formation of three hydrogen bonds as illustrated in Figure 8.14b, one would expect to observe two shifted silanol bands: one at 3223 cm^{-1} for the two hydrogen-bonded methoxy groups and a band at higher wavenumbers for the hydrogen-bonded P=O group as observed for adsorbed TCP and MDCP. However, because only a single broad band at 3223 cm^{-1} is observed, Kanan and Tripp [115] concluded that DMMP is adsorbed

through hydrogen bonding of the two methoxy groups as illustrated in Figure 8.14b. This is consistent with the observed small shift in the P=O stretching mode.

Although it is suggested that the P=O group of TMP and DMMP is not hydrogen-bonded to surface silanols, a small redshift in the P=O stretching frequency is observed for both compounds. One possible explanation is that the formation of hydrogen bonds involving the methoxy groups may reduce the electron-donating strength from the methoxy groups to the phosphorus atom, thus decreasing the strength of the P=O bond [115].

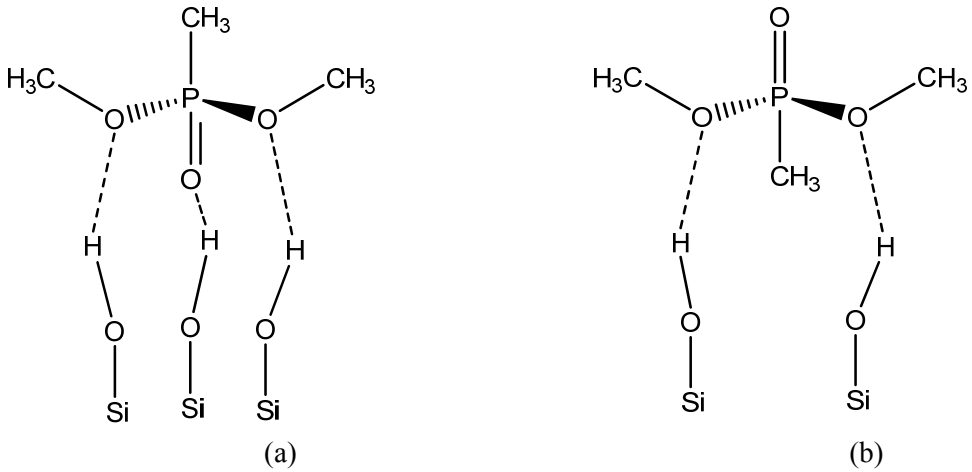

Figure 8.14 Structures of possible adorption complexes of dimethyl methylphosphonate (DMMP) on solid silicon dioxide (SiO_2) [115].

Hussain [116] tested quartz glass and borosilicate glass containers for collection of environmental samples with respect to recovery of chemical warfare agents from the containers (unfortunately the glass compositions are not known in detail). Soil and snow were tested as sample matrices. One of the compounds Hussain tested was trideuterated diisopropyl methylphosphonate (DIMP-d_3). DIMP is a commonly used G-agent simulant. Generally, low recoveries of DIMP-d_3 from the glass containers were observed at room temperature with the quartz glass container being the worst.

DIMP is structurally similar to DMMP. Thus, it is very likely that DIMP will adsorb to silica in the same way as DMMP through formation of two hydrogen bonds involving the $(CH_3)_2CH–O–P$ moieties. It is therefore expected that elevated temperatures are needed for full recovery of DIMP and other organophosphates from glass containers.

9 Summary and conclusions

This report has given a two fold introduction to adsorption phenomena. First focus has been set on theory and different experimental methods. The purpose of the first part has been to give readers new to the field a theoretical background to adsorption and an overview of possible experimental techniques. The techniques mentioned are complimentary and will all give different in-

formation. Combining different methods can hence give a broad picture of chemistry and physics when something adsorps on a surface.

The second part of the report summarizes different studies performed on the degradation of CWA on metal oxides. There is a significant amount of knowledge on the interaction between sulfur mustard and different oxides. As discussed, the reaction rate and the fraction of final products from sulfur mustard (HD) decomposing on metal oxides depend on the acid-base properties of the surface, and also the amount of water adsorbed. The hydrolysis rate will increase remarkably when water is absorbed on the surface, this is particularly clear for the basic oxides. However, formation of sulfonium ions is hindered on too heavily hydrated surfaces and at surfaces where destructive adsorption occurs. Elimination of HCl from HD is situated at the basic sites of the oxides. This is also possible at the Lewis acidic sites. Splitting of the sulfur mustard molecule through cleavage of the C–Cl and C–S bonds probably proceeds at the acid sites of the oxides and during reaction with H^+ from the hydrolysis. The main degradation products are 2-chloro-2′-hydroxydiethyl sulfide (CH), bis(2-hydroxyethyl)sulfide (TG), and 2-chloroethyl vinyl sulfide (CEVS). The degradation rate decreases with too big HD droplets; the reaction capacity of the oxide may then be overwhelmed. A commonly used simulant for sulfur mustard is 2-chloroethyl methyl sulfide (2-CEES). The products from the degradation of 2-CEES on oxides are consistent with the products from the decomposition of HD. To conclude, the interactions between sulfur mustard and oxides are well understood. However, less information is available on the other vesicants like nitrogen mustards and lewisite, or the mustard-lewisite mixture HL.

When it comes to the adsorption and degradation of nerve agents on oxides, the knowledge originate mainly from studies of simulants. On Al_2O_3, TiO_2, and Fe_2O_3 the nerve agent simulant dimethyl methylphosphonate (DMMP) adsorbs molecularly through bonding between the P=O group and surface acid sites. This will most likely also be the case for the nerve agents. As has been discussed, the mechanism for the degradation of the adsorbed species is generally the same for the different oxides with Fe_2O_3 and SiO_2 as exceptions. On dry SiO_2 no degradation will occur, while on a hydrated surface only a small fraction of the organophosphorous will decompose. There is a need for more information on which products that are formed in the degradation of G and V-type nerve agents on oxides. This information must come from experiments. However, quantum chemical calculations are very useful for elucidating the degradation mechanisms and for interpreting the experimental results.

References

Bibliography

[1] "Convention on the Prohibition of the Development, Production, Stockpiling and Use of Chemical Weapons and on their Destruction (Chemical Weapons Convention)," The Organisation for the Prohibition of Chemical Weapons (OPCW): The Hague, Netherlands, 2010.

[2] "Potential military chemical/biological agents and compounds," US Army Chemical School, Fort Leonard Wood, MO,FM 3-11.9, MCRP 3-37.1B, NTRP 3-11.32, AFTTP(I) 3-2.55, 2005.

[3] L. Szinicz, "History of chemical and biological warfare agents," *Toxicology*, vol. 214, no. 3, pp. 167-181, Oct.2005.

[4] "Status of participation in the Chemical Weapons Convention as at 21 May 2009," The Organisation for the Prohibition of Chemical Weapons (OPCW), The Hague, Netherlands,Note by the Technical Secretariat S/768/2009, May2009.

[5] "North Korea's Weapons Programmes - A Net Assessment," The International Institute for Strategic Studies, 2004.

[6] M. Z. Diab, "Syria's chemical and biological weapons: Assessing capabilities and motivations," *The Nonproliferation Review*, vol. 5, pp. 104-111, 1997.

[7] D. Shoham, "Chemical and biological weapons in Egypt," *The Nonproliferation Review*, vol. 5, pp. 48-58, 1998.

[8] B. Lia, T. Hegghammer, R. I. Vogt Andersen, Å. Kjøk, and L. Bokhari, "Atommateriale, gass og mikrober som terrorvåpen? En undersøkelse av terrorgruppers interesse for og bruk av ikke-konvensjonelle våpen," Forsvarets forskningsinstitutt, Kjeller, Norway,FFI-rapport 2001/02930, Mar.2002.

[9] S. S. Talmage, A. P. Watson, V. Hauschild, N. B. Munro, and J. King, "Chemical warfare agent degradation and decontamination," *Curr. Org. Chem.*, vol. 11, pp. 285-298, 2007.

[10] M. Nic, J. Jirat, and B. Kosata, "IUPAC Compendium of Chemical Terminology (Gold Book)," 2009.

[11] I. H. Svenum, "Adsorption at solid surfaces," 2009.

[12] L. K. Engman, A. Lindblad, A.-K. Tunemalm, O. Claesson, and B. Lilliehöök, "Kemiska vapen - hot, verknad och skydd," Sverige: Totalförsvarets Forskningsinstitutt (FOI), 2002.

[13] S. L. Bartelt-Hunt, D. R. U. Knappe, and M. A. Barlaz, "A review of chemical warfare agent simulants for the study of environmental behavior," *Crit. Rev. Env. Sci. Tec.*, vol. 38, no. 2, pp. 112-136, 2008.

[14] "SciFinder Scolar, web version," 2010.

[15] V. S. Mirzayanov, "Dismantling the Soviet/Russian Chemical Weapons Complex: An Insider's View," in *Chemical Weapons Disarmament in Russia: Problems and Prospects*.

A. E. Smithson, V. S. Mirzayanov, R. Lajoie, and M. Krepon, Eds. Washington DC: The Henry L. Stimson Center, 1995, pp. 21-33.

[16] P. C. Hemmer, *Faste stoffers fysikk*. Trondheim: Tapir forlag, 1987.

[17] S. Zumdahl, *Chemical principles*. U.S.A: Houghtun Mifflin company, 1998.

[18] Ibach and Luth, *Festkörperphysik*. Heidelberg: Springer Verlag, 2002.

[19] M. T. Dove, *Structure and dynamics*. New York: Oxford university press, 2009.

[20] "Miller index," Wikipedia, The Free Encyclopedia, 2010.

[21] H. Ibach, *Physics of Surfaces and Interfaces*. Berlin Heidelberg: Springer, 2006.

[22] D. P. Woodruff, *The Solid-Liquid Interface*. London: Cambridge University Press, 1973.

[23] S. H. Payne, H. J. Kreuzer, K. A. Peterlinz, T. J. Curtiss, C. Uebing, and S. J. Sibener, "Coverage dependent desorption kinetics of CO from Rh(111): a theoretical analysis," *Surf. Sci.*, vol. 272, pp. 102-110, 1992.

[24] I. G. Pitt, R. G. Gilbert, and K. R. Ryan, "The application of transition state theory to gas-surface reactions. III. Lattice gas systems with adsorbate interactions," *Surf. Sci.*, vol. 326, pp. 361-369, 1995.

[25] A. Nilson, L. G. M. Pettersen, and J. K. Nørskov, *Chemical bonding at surfaces and interfaces*. Amsterdam: Elsevier, 2008.

[26] S. Holloway and J. Nørkov, *Bonding at surfaces*. Liverpool: Liverpool University Press, 1991.

[27] A. Gross, *Theoretical Surface Science. A Microscopic Perspective*. Berlin, Heidelberg: Springer Verlag, 2003.

[28] J. Fraissard, "Physical Adsorption: Experiment, Theory and Applications," Dordrecht: Kluwer Academic Publishers, 1996, p. 114.

[29] J. E. Lennard-Jones, "Processes of adsorption and diffusion on solid surfaces," *Trans. Faraday Soc.*, vol. 28, pp. 333-359, 1932.

[30] A. Zangwill, *Physics at surfaces* Cambridge university press, 1988.

[31] A. Dabrowski, "Adsorption - from theory to practice," *Adv. Colloid Interface Sci.*, vol. 93, pp. 135-224, Oct.2001.

[32] J. Tóth, *Adsorption, theory, modeling and analysis*. New York: Marcel Dekker, 2002.

[33] A. Mannarswamy, S. H. Munson-McGee, R. Steiner, and P. K. Andersen, "D-optimal experimental designs for Freundlich and Langmuir adsorption isotherms," *Chemometrics and Intelligent Laboratory Systems*, vol. 97, pp. 146-151, 2009.

[34] "Henry's law," Wikipedia, The Free Encyclopedia, 2010.

[35] D. M. Young and A. D. Crowell, *Physical adsorption of gases*. London: Butterworth & Co, 1962.

[36] I. Langmuir, "The constitution and fundamental properties of solids and liquids," *J. Am. Chem. Soc.*, vol. 38, pp. 2221-2295, 1916.

[37] C. L. Mantell, *Chemical engineering science* McGraw-Hill, 1945.

[38] S. Brunauer, E. Emmett, and T. Teller, "Adsorption og gases in multimonomolecular layers," *J. Am. Chem. Soc.*, vol. 60, p. 309, 1938.

[39] K. S. W. Sing, D. H. Everett, R. A. W. Haul, L. Moscou, R. A. Pierotti, J. Rouquérol, and T. Siemieniewska, "Reporting physisorption data for gas/solid system, with special reference to the determination of surface area and porosity," *Pure & Appl. Chem.*, vol. 57, no. 4, pp. 603-619, 1985.

[40] R. I. Masel, *Adsorption and reactions on solid surfaces*. New York: John Wiley and Sons, 1996.

[41] S. Brunauer, L. S. Deming, W. E. Deming, and E. Teller, "On a theory of van der Waals adsorption of gases," *J. Am. Chem. Soc.*, vol. 62, p. 1723, 1940.

[42] I. G. Pitt, R. G. Gilbert, and K. R. Ryan, "Application of transition-state theory to gas-surface reactions: Barrierless adsorption on clean surfaces," *J. Phys. Chem.*, vol. 98, pp. 13001-13010, 1994.

[43] H. Ibach, W. Erley, and H. Wagner, "The preexponential factor in desorption - CO on Ni(111)," *Surf. Sci.*, vol. 92, pp. 29-42, 1980.

[44] M. G. Evans and M. Polanyi, "Application of the transition-state method to the calculation of reaction velocities, especially in solution," *Trans. Faraday Soc.*, vol. 31, pp. 875-894, 1935.

[45] H. Eyring, "Activated complex in chemical reactions," *J. Chem. Phys.*, vol. 3, pp. 107-115, 1935.

[46] E. Wigner, "The transition-state method," *Trans. Faraday Soc.*, vol. 34, pp. 29-41, 1938.

[47] M. Hazewinkel, "Encyclopaedia of Mathematics," Berlin, Heidelberg, New York: Springer-Verlag, 2002.

[48] J. C. Keck, "Variational theory of reaction rates," *Adv. Chem. Phys.*, vol. 13, pp. 85-121, 1967.

[49] D. G. Truhlar, A. D. Isaacson, and B. C. Garrett, "Generalized Transition State Theory," in *Theory of Chemical Reaction Dynamics*. M. Baer, Ed. Boca Raton, FL: CRC Press, 1985, pp. 65-137.

[50] I. G. Pitt, R. G. Gilbert, and K. R. Ryan, "The application of transition state theory to gas-surface reactions in Langmuir systems," *J. Chem. Phys.*, vol. 102, pp. 3461-3473, 1995.

[51] J. W. Niemantsverdriet, *Spectroscopy in Catalysis. An Introduction*, 3rd. ed. Weinheim: Wiley-VCH Verlag GmbH & Co KGaA, 2007.

[52] J. M. Kanervo, T. J. Keskitalo, R. I. Slioor, and A. O. I. Krause, "Temperature-programmed desorption as a tool to extract quantitative kinetic or energetic information for porous catalysts," *J. Catal.*, vol. 238, pp. 382-393, 2006.

[53] I. Gausemel, "Infrared study of CO and CO_2 adsorption on copper-containing samples." Ph.D. University of Oslo, 2001.

[54] R. J. Abraham, J. Fisher, and P. L. Loftus, *Introduction to NMR spectroscopy* John Wiley and sons, 1988.

[55] M. A. Fox and J. K. Whitesell, *Core Organic Chemistry*. London: Jones and Barlett Publishers International, 1997.

[56] E. W. Hansen and B. Pedersen, "FYS-KJM4740 MR spectroscopy and Tomography - part I," Department of Chemistry, University of Oslo,2009.

[57] J. P. Hornak, "Basics of NMR," 1999.

[58] P. C. Hemmer, *Kvantemekanikk*. Trondheim: Tapir forlag, 1999.

[59] B. Arstad, "NMR-presentasjon (SINTEF)," 2009.

[60] G. Aylward and T. Findlay, *SI chemical data*, 4 ed. Milton: John Wiley and Sons, 1998.

[61] K. S. Krane, *Introductory to nuclear physics*. New York: John Wiley and Sons, 1988.

[62] M. J. Duer, *Introduction to Solid-State NMR spectroscopy*. Oxford: Blackwell publishing, 2004.

[63] "Bruker Bio Spin," 2009.

[64] F. Jensen, *Introduction to Computational Chemistry*. Chichester: John Wiley & Sons, 1999.

[65] T. Helgaker, P. Jørgensen, and J. Olsen, *Molecular Electronic-Structure Theory*. Chichester: John Wiley & Sons, 2000.

[66] C. Møller and M. S. Plesset, "Note on a approximation treatment for many-electron systems," *Phys. Rev.*, vol. 46, pp. 618-622, 1934.

[67] J. Cizek, "Use of the cluster expansion and the technique of diagrams in calculations of correlation effects in atoms and molecules," *Adv. Chem. Phys.*, vol. 14, pp. 35-89, 1969.

[68] G. D. Purvis III and R. J. Bartlett, "A full coupled-cluster singles and doubles model: the inclusion of disconnected triples," *J. Chem. Phys.*, vol. 76, pp. 1910-1918, 1982.

[69] G. E. Scuseria, C. L. Janssen, and H. F. Schaefer III, "An efficient reformulation of the closed-shell coupled cluster single and double excitation (CCSD) equations," *J. Chem. Phys.*, vol. 89, pp. 7382-7387, 1988.

[70] G. E. Scuseria and H. F. Schaefer III, "Is coupled cluster singles and doubles (CCSD) more computationally intensive than quadratic configuration interaction (QCISD)?," *J. Chem. Phys.*, vol. 90, pp. 3700-3703, 1989.

[71] K. Raghavachari, G. W. Trucks, J. A. Pople, and M. Head-Gordon, "A fifth-order perturbation comparison of electron correlation theories," *Chem. Phys. Lett.*, vol. 157, pp. 479-483, 1989.

[72] P. Hohenberg and W. Kohn, "Inhomogeneous electron gas," *Phys. Rev.*, vol. 136, p. B864-B871, 1964.

[73] W. Kohn and L. J. Sham, "Self-consistent equations including exchange and correlation effects," *Phys. Rev.*, vol. 140, p. A1133-A1138, 1965.

[74] A. D. Becke, "Density-functional thermochemistry. III. The role of exact exchange," *J. Chem. Phys.*, vol. 98, pp. 5648-5652, 1993.

[75] C. Lee, W. Yang, and R. G. Parr, "Development of the Colle-Salvetti correlation-energy formula into a functional of the electron density," *Phys. Rev. B*, vol. 37, pp. 785-789, 1988.

[76] W. J. Hehre, R. F. Stewart, and J. A. Pople, "Self-consistent molecular-orbital methods. I. Use of Gaussian expansions of Slater-type atomic orbitals," *J. Chem. Phys.*, vol. 51, pp. 2657-2664, 1969.

[77] M. J. Frisch, J. A. Pople, and J. S. Binkley, "Self-consistent molecular orbital methods. 25. Supplementary functions for Gaussian basis sets," *J. Chem. Phys.*, vol. 80, pp. 3265-3269, 1984.

[78] T. H. Dunning, Jr., "Gaussian basis sets for use in correlated molecular calculations. I. The atoms boron through neon and hydrogen," *J. Chem. Phys.*, vol. 90, pp. 1007-1023, 1989.

[79] A. K. Wilson, T. van Mourik, and T. H. Dunning, Jr., "Gaussian basis sets for use in correlated molecular calculations. VI. Sextuple zeta correlation consistent basis sets for boron through neon," *J. Mol. Struct. (Theochem)*, vol. 388, pp. 339-349, 1996.

[80] R. A. Kendall, T. H. Dunning, Jr., and R. J. Harrison, "Electron affinities of the first-row atoms revisited. Systematic basis sets and wave functions," *J. Chem. Phys.*, vol. 96, pp. 6796-6806, 1992.

[81] G. W. Wagner, O. B. Koper, E. Lucas, S. Decker, and K. J. Klabunde, "Reactions of VX, GD, and HD Nanosize CaO: Autocatalytic Dehydrohalogentaion of HD," *J. Phys. Chem.*, vol. 104, pp. 5118-5123, 2000.

[82] G. W. Wagner, P. W. Bartram, O. B. Koper, and K. J. Klabunde, "Reactions of VX, GD and HD with nanosize MgO," *J. Phys. Chem.*, vol. 103, pp. 3225-3228, 1999.

[83] H. Tang, Z. Cheng, H. Zhu, G. Zuo, and M. Zhang, "Effect of acid and base sites on the degradation of sulfur mustard over several typical oxides.," *Appl. Catal. B*, vol. 79, pp. 323-333, 2008.

[84] "ZSM-5," Wikipedia, The Free Encyclopedia, 2010.

[85] "Alpha and beta carbon," Wikipedia, The Free Encyclopedia, 2010.

[86] G. W. Wagner and B. K. MacIver, "Degradiation of fate of mustard in soil as determined by ^{13}C MAS NMR," *Langmuir*, vol. 14, pp. 6930-6934, 1998.

[87] D. B. Mawhinney, Rossin J.A., K. Gerhart, and Yates J.T., "Adsorption an Reaction of 2-Chloroethylethyl sulfide with Al_2O_3 surfaces," *Langmuir*, vol. 15, pp. 4789-4795, 1999.

[88] D. B. Mawhinney, Rossin J.A., K. Gerhart, and Yates J.T., "Infrared Spectroscopic Study of the Surface Diffusion to Surface Hydroxyl Groups on Al_2O_3: 2-Chloroethyl Sulfide Adsorption Site Selection," *Langmuir*, vol. 16, pp. 2237-2241, 2000.

[89] V. M. Bermudez, "Computational study of environmental ffects in the adsorption of DMMP, sarin, and VX on γ-Al_2O_3: Photolysis and surface hydroxylation," *J. Phys. Chem. C*, vol. 113, no. 5, pp. 1917-1930, 2009.

[90] G. W. Wagner, L. R. Procell, R. J. O'Connor, S. Munavalli, C. L. Carnes, P. N. Kapoor, and K. J. Klabunde, "Reactions of VX, GB, GD, and HD with nanosize Al_2O_3. Formation of aluminophosphonates," *J. Am. Chem. Soc.*, vol. 123, no. 8, pp. 1636-1644, 2001.

[91] G. W. Wagner, L. R. Procell, and S. Munavalli, "^{27}Al, $^{47-49}$Ti, ^{31}P and ^{13}C MAS NMR study of VX, GD and HD reactions with nanosize Al_2O_3, Conventional Al_2O_3 and TiO_2 and Aluminium and Titanium Metal," *J. Phys. Chem.*, vol. 111, pp. 17564-17569, 2007.

[92] Y. Zafrani, M. Goldvaser, S. Dagan, L. Feldberg, D. Mizrahi, D. Waysbort, E. Gershonov, and I. Columbus, "Degradation of Sulfur Mustard on KF/Al_2O_3. Supports: Insights into the Products and the Reactions Mechanisms," *J. Org. Chem.*, vol. 74, no. 21, pp. 8464-8467, 2009.

[93] I. N. Martyanov and K. J. Klabunde, "Photocatalytic Oxidation of Gaseous 2-Chloroethyl ethyl sulfide over TiO_2," *Env. Sci. Technol.*, vol. 37, pp. 3448-3453, 2003.

[94] T. L. Thompson, D. A. Panayotov, and J. T. Yates, Jr., "Adsorption and Thermal Decompostion of 2-Chloroethyl Ethyl Sulfide on TiO_2 Surfaces," *J. Phys. Chem. B*, vol. 108, pp. 16825-16833, 2004.

[95] D. A. Panayotov and J. T. Yates, Jr., "Bifunctional Hydrogen Bonding of 2-Chloroethyl ethyl sulfide on TiO2-SiO2 Powders," *J. Phys. Chem. B*, vol. 107, pp. 10560-10564, 2003.

[96] D. A. Panayotov, P. Kondrayuk, and Yates J.T., "Photooxidation of a Mustard Gas Simulant over TiO_2-SiO_2 Mixed-Oxide Photocatalyst: Site poisoning by Oxidation Products and Reactivation," *Langmuir*, vol. 20, pp. 3674-3678, 2004.

[97] M. K. Templeton and W. H. Weinberg, "Adsorption and decomposition of dimethyl methylphosphonate on an aluminum oxide surface," *J. Am. Chem. Soc.*, vol. 107, pp. 97-108, 1985.

[98] M. K. Templeton and W. H. Weinberg, "Decomposition of phosphonate esters adsorbed on aluminum oxide," *J. Am. Chem. Soc.*, vol. 107, pp. 774-779, 1985.

[99] B. Aurian-Blajeni and M. M. Boucher, "Interaction of dimethyl methylphosphonate with metal oxides," *Langmuir*, vol. 5, pp. 170-174, 1989.

[100] V. M. Bermudez, "Quantum-chemical study of the adsorption of DMMP and sarin on γ-Al_2O_3," *J. Phys. Chem. C*, vol. 111, no. 9, pp. 3719-3728, 2007.

[101] W. Y. Ching, L. Ouyang, P. Rulis, and H. Yao, "Ab initio study of the physical properties of γ-Al_2O_3: Lattice dynamics, bulk properties, electronic structure, bonding, optical properties, and ELNES/XANES spectra," *Phys. Rev. B*, vol. 78, no. 1, p. 014106, July2008.

[102] M. Rosenberg, A. Loewenschuss, and C. J. Nielsen, "Spectral shifts of matrix isolated species as criteria for acid-base interactions with solid Xe," *Phys. Chem. Chem. Phys.*, p. submitted, 2009.

[103] C. N. Rusu and J. T. Yates, "Adsorption and decomposition of dimethyl methylphosphonate on TiO_2," *J. Phys. Chem. B*, vol. 104, no. 51, pp. 12292-12298, 2000.

[104] C. S. Kim, R. J. Lad, and C. P. Tripp, "Interaction of organophosphorous compounds with TiO_2 and WO_3 surfaces probed by vibrational spectroscopy," *Sens. Actuators, B*, vol. 76, pp. 442-448, 2001.

[105] D. A. Panayotov and J. R. Morris, "Uptake of a chemical warfare agent simulant (DMMP) on TiO_2: Reactive adsorption and active site poisoning," *Langmuir*, vol. 25, no. 6, pp. 3652-3658, 2009.

[106] D. A. Panayotov and J. R. Morris, "Thermal decomposition of a chemical warfare agent simulant (DMMP) on TiO_2: Adsorbate reactions with lattice oxygen as studied by infrared spectroscopy," *J. Phys. Chem. C*, vol. 113, pp. 15684-15691, 2009.

[107] J. A. Moss, S. H. Szczepankiewicz, E. Park, and M. R. Hoffmann, "Adsorption and photodegradation of dimethyl methylphosphonate vapor at TiO_2 surfaces," *J. Phys. Chem. B*, vol. 109, pp. 19779-19785, 2005.

[108] T. N. Obee and S. Satyapal, "Photocatalytic decomposition of DMMP on titania," *J. Photochem. Photobiol. , A*, vol. 118, pp. 45-51, 1998.

[109] C. N. Rusu and J. T. Yates, "Photooxidation of dimethyl methylphosphonate on TiO_2 powder," *J. Phys. Chem. B*, vol. 104, pp. 12299-12305, 2000.

[110] M. A. Henderson, T. Jin, and J. M. White, "A TPD/AES study of the interaction of dimethyl methylphosphonate with α-Fe_2O_3 and SiO_2," *J. Phys. Chem.*, vol. 90, pp. 4607-4611, 1986.

[111] M. B. Mitchell, V. N. Sheinker, A. B. Tesfamichael, E. N. Gatimu, and M. Nunley, "Decomposition of dimethyl methylphosphonate (DMMP) on supported cerium and iron co-impregnated oxides at room temperature," *J. Phys. Chem. B*, vol. 107, pp. 580-586, 2003.

[112] T. M. Tesfai, V. N. Sheinker, and M. B. Mitchell, "Decomposition of dimethyl methylphosphonate (DMMP) on alumina-supported iron oxide," *J. Phys. Chem. B*, vol. 102, pp. 7299-7302, 1998.

[113] "Bluing (steel)," Wikipedia, The Free Encyclopedia, 2010.

[114] P. Kofstad, *Uorganisk kjemi. En innføring i grunnstoffenes kjemi*, 3rd ed. Oslo: TANO, 1992.

[115] S. M. Kanan and C. P. Tripp, "An infrared study of adsorbed organophosphonates on silica: A prefiltering strategy for the detection of nerve agents on metal oxide sensors," *Langmuir*, vol. 17, pp. 2213-2218, 2001.

[116] F. Hussain, "Test av beholdere for innsamling av miljøprøver i forbindelse med verifikasjon av kjemiske stridsmidler," Forsvarets forskningsinstitutt, Kjeller, Norway,FFI-rapport 2000/03807, July2000.

Abbreviations

Abbreviation	Explanation
2-CEES	2-chloroethyl methyl sulfide
Al_2O_3	Aluminum oxide
AP	Aerogel-prepared
ATR	Attenuated total reflectance
BO	Born-oppenheimer
BSSE	Basis-set superposition error
CaO	Calcium oxide
CBRN	Chemical, biological, radiological, nuclear
CC	Coupled cluster
ccp	Cubic closes packed
CEVS	2-Chloroethyl vinyl sulfide
CH	2-Chloro-2-hydroxyethyl sulfide / Hemimustard
CH_3CH_2	Ethoxy
Cl_2	Chlorine
CP	Cross-polarization
CVR	Chinese VX
CWA	Chemical warfare agent
CWC	Chemical weapons convention
DDMMP	Deuterated DMMP
DEPPT	O,S-diethyl phenylphosphonothioate
DFT	Density functional theory
Dially Sulfide	2-Propenyl disulphide
DIMP (DIPMP)	Diisopropyl methylphosphonate
DMMP	Dimethyl methylphonate
DRIFTS	Diffuse reflectance infrared Fourier transform spectroscopy
DZ	Double zeta
eV	Electron volt
$E_{xc}[\rho(\mathbf{r})]$	Exchange-correlation functional
Fe_2O_3	Iron(III) oxide
FFI	Norwegian defence research establishment
FID	Free induction decay
FT-IR	Fourier-transform infrared spectroscopy
GA	Tabun
GB	Sarin
GC-FPD	Gas chromatography-flame photometric detection
GC-MS	Gas chromatography-mass spectroscopy
GD	Soman
GF	Cyclosarin
GTO	Gaussian type orbitals
HD	Sulfur mustard
HEVS	2-Hydroxyethyl vinyl sulfide
HF	Hartree-fock
HN-1, HN-2, HN-3	Nitrogen mustard

HOMO	Highest occupied molecule orbital
IUPAC	The International Union of Pure and Applied Chemistry
KS	Kohn-sham
L	Lewisite
LCAO	Linear combination of atomic orbitals
LDA	Local denity approximation
LUMO	Lowest unoccupied molecule orbital
MAS	Magic angle spinning
MBPT	Many-body perturbation theory
MDCP	Methyl dichlorophosphate
MgO	Magnesium dioxide
MMP (MMPA)	Methyl methylphosphonate
MO	Molecular orbital
MPPT	Møller-Plesset perturbation theory
MS	Methyl salicylate
NMR	Nuclear magnetic resonance spectroscopy
O-mustard	Bis-[(2-chloroethylthio) ethyl] ether
OPCW	Prohibition of Chemical Weapons
PBE	Perdew-burke-ernzerhoff
PES	Potential energy hypersurface
RAIRS	Reflection absorption infrared spectroscopy
S_2Cl_2	Sulfur chloride
SCF	Self-consistent field
SD	Slater determinant
SE	Schrödinger equation
SEM	Scanning electron microscopy
Sequimustard	1,2-Bis(2-Chloroethylthio)ethane
SiO_2	Silicon dioxide
STO	Slater type orbitals
TCP	Trichlorphosphate
TG (TDG)	Bis(2-hydroxyethyl) sulfide
TiO_2	Titanium dioxide
TMP	Trimethyl phosphate
TPD	Temperature programmed desorption
TPD	Temperature programmed desorption-mass spectroscopy
TST	Transition state theory
UV-VIS	Ultraviolet-visible spectroscopy
VDZ	Valenze double zeta
VR	Russian VX
VWN	Vasko-wilk-nusair
WMD	Weapons of mass destruction